ANALYSIS OF MULTI-COMPONENT SEISMIC DATA IN THE SHALLOW WATER ENVIRONMENT OF THE ARABIAN GULF

A Dissertation

by

ZHAO ZHANG

Submitted to the Office of Graduate and Professional Studies of
Texas A&M University
in partial fulfillment of the requirements for the degree of

DOCTOR OF PHILOSOPHY

Chair of Committee,	Yuefeng Sun
Committee Members,	Benchun Duan
	Yalchin Efendiev
	Mark Everett
	Zoya Heidari
Head of Department,	John R. Giardino

May 2015

Major Subject: Geophysics

ABSTRACT

The quality of the seismic data is essential to quantitative reservoir characterization of rock properties and geological structure interpretation. Although marine multi-component seismic data hold a wealth of information about both compressional and shear velocities, the acquisition suffers from high levels of noise, which make the processing a challenging task and drastically decreases optimal value extraction. This dissertation employs a four component (4C) processing workflow via advanced time-frequency-wavenumber filtering and polarization methods to improve data quality for further interpretation and reservoir characterization.

The proposed workflow is used to enhance seismic reflected energy and explore the shear wave information in the horizontal components. This study makes use of one 2D seismic line and well log dataset from one offshore in the southern Arabian Gulf (Abu Dhabi, United Arab Emirates). A combination of strong lateral seafloor heterogeneities, shallow water depths (~10m), and hard sea bottom results in highly interfering and complex wave-fields and seemingly noisy seismic data acquired in this shallow water environment. Meanwhile, we expect converted wave modes (PS-S waves) due to the strong reflector at hard sea bottom. In this work, we first propose sophisticated filtering algorithms to attenuate surface waves, and then designed advanced processing sequence combined with existing techniques for converted waves detection.

Compared to body waves, surface waves are characterized by low velocity, low frequency and high polarization. First, we utilize the variable factor S transform to

transform the seismic data from time domain to time-frequency-wavenumber(TFK) domain. This designed transform provides better resolution control on both time and frequency by adjusting the shape of Gaussian window function through additional parameters. Second, we estimate the impacts of residual surface waves on rotation and suppress those waves using TFK dependent polarization analysis. Polarization attributes, ellipticity and rise angle, are calculated through a developed 3D covariance matrix analysis that exploits the joint relationship of wavenumber, time, frequency and polarization. Those computed attributes are used for attenuating the surface waves and determining radial and transverse components. Third, we introduce the new 4C ocean bottom cable (OBC) processing strategy using both compressional and shear waves to recover the image of the subsurface from noisy seismic data.

Comparing the time slices and gathers before and after using the strategy, it is observed that the method, described here, attenuates surface waves and remnant surface waves effectively and improves the signal to noise ratio without weakening the desired reflected signals. The results from this dissertation will find application in reservoir characterization from shear wave and converted wave analysis.

DEDICATION

To my wonderful parents, who were not lucky enough to have much education when they were growing up, but value education most highly.

ACKNOWLEDGEMENTS

The completion of a PhD is an endeavor that requires much outside help, especially for a person like me who transferred from computer science to geophysics. I would like to first thank Dr. Sun, the chairman of my advisory committee, for his constant helpful advice, comments and financial support throughout my PhD program at Texas A&M University, particularly during the most difficult times. I always get inspired by the insightful ideas he gives me, not only for the research problems but also life attitude. His sincerity toward science and teaching will always set an example for many to follow.

I also would like to thank my dissertation committee members, Dr. Duan, Dr. Everett, Dr. Efendiev and Dr. Heidair, for giving valuable suggestions to improve my understanding of the problems and the clarification for the conclusions.

I am grateful to the R&D Oil-Subcommittee of the Abu Dhabi National Oil Company (ADNOC) and its operating companies (OpCos) for sponsoring this project and permission for publication. My thanks also go to TAMU Berg-Hughes center, Aramco, BP, ConocoPhillips and ExxonMobil for providing fellowship support; as well as Chevron for internship opportunities.

I am indebted to every member of the Reservoir Geophysics Program (RGP): Hamid Adesokan, Qifeng Dou, Liqin Sang, and Tingting Zhang. They have all provided assistance to me in many aspects of my studies and in my life. Finally, I want to thank my parents for their love, engagement and support over the years.

NOMENCLATURE

4C	Four Components
OBC	Ocean Bottom Cable
V_P	Velocity of Compressional waves
V_S	Velocity of Shear waves
FFT	Fast Fourier Transform
CWT	Continuous Wavelet Transform
STFT	Short Time Fourier Transform

TABLE OF CONTENTS

Page

LIST OF FIGURES

Page

LIST OF TABLES

Page

CHAPTER I

INTRODUCTION

Multi-component seismic data(3C on land; 2C/4C on seabed) aim to record the full elastic wave-field, including shear(S) wave information that complements the compressional(P) wave information; also contain valuable additional information about subsurface. Compared to traditional single component seismic data, the poor data quality is a serious problem in the 3C/4C acquisition, especially in the shallow water environment, with issues such as ground coupling, surface heterogeneity and geophone orientation being the most serious. Therefore, up to now, 3C/4C seismic data have been used in field application only as better P-wave data, whereas the value of the data recorded by the two horizontal components has not been demonstrated. Additionally, traditional processing technology on 1C data cannot be simply extended to 3C/4C data, which requires dedicated algorithms and procedures. To obtain the full benefit of the multicomponent measurement, advanced surface waves attenuation algorithm and 4C processing workflow are proposed and implemented on real field data in this study.

1.1. Statement and Significance of the Problem

Accurate estimation and imaging of the subsurface geological structure from the seismic reflection data have been a challenging problem in the hydrocarbon exploration. Subsurface imaging is related to velocity, and a high-resolution subsurface image necessitates an accurate velocity profile obtained from a high quality seismic dataset. In

addition, the elastic wave propagation in the Earth's interior involves complex interaction between incident waves and subsurface, including reflection, refraction, diffraction, polarization, and absorption. Accordingly, the image quality depends on the combination of proper acquisition and optimized processing technologies, which requires fully considering wave propagation properties.

Recording horizontal vibrations, as well as vertical motion and pressures, four-component (4C) ocean bottom cable (OBC) seismic data contains the full seismic wave-field that can provide greater comprehension of subsurface structure and fluid properties. P-wave velocity is a function of the medium's density, shear modulus and bulk modulus, whereas S-wave velocity is a function of the density and the shear modulus only. Therefore, P-wave is highly sensitive to pore's fluid content and its velocity decreases with reducing fluid saturation. The propagation of S-wave is not influenced by the fluid type, saturation and pressure, which means that S-wave velocity and reflectivity is relatively unaffected by the pore fluid and primarily depend on rock matrix (Waggoner and Kristiansen, 2003). With P-wave alone, it is not sufficient to produce subsurface image or describe its properties, especially when gas, even in small amounts, exists in the reservoir (Nahm and Duhon, 2003). Additionally, P wave only may fail to determine important reservoir properties, such as lithology or formation stress, from changes in fluid composition or pressure, as well as the presence, density and orientation of fractures in the overburden. With the additional help of S-wave, 4C OBC seismic data brings the opportunity to obtain more accurate estimation of key reservoir fluid/rock

properties and provide a valuable tool for structural interpretation and lithology changes prediction.

In 4C OBC acquisition, each receiver consists of one hydrophone and three tri-axis orthogonal geophones. Geophones are effective at separating components so that reflection signals can be acquired and split even when there are mixed wave fields. Theoretically, vertical components record the P-wave motion and two horizontal components record the S-wave motion. The pressure component, hydrophone, provides additional measurement of the P-wave motion through the fluid pressure changes. Three geophone components need to be aligned in the direction of wave propagation to measure the ground motion. Correct orientation in all three orthogonal vector directions is obtained through careful deployment, which is critical to obtain high quality dataset but difficult to achieve in the marine environment. Besides the geophone ground coupling issue, the data quality in offshore acquisition is also influenced by other factors including subsurface condition, deep currents, and weather. Moreover, it is more challenging to collect data in a shallow water environment.

Shallow marine acquisition is the only water-based seismic acquisition in which the land recording equipment is implemented in a marine environment. It often presents low signal-to-noise ratio (S/N) issues associated with strong lateral seafloor heterogeneities, shallow water depths, and hard sea bottom. Typically this acquisition has been done with the two- component recording (hydrophone P component and vertical geophone Z component) to obtain P-wave information (Berteussen and Sun, 2010). In the shallow water Arabian Gulf, 4C OBC acquisition has been implemented

for collecting extra shear information. However, the collected data suffers even more serious noise issues in this area. It contains refracted horizontally polarized head waves, Scholte waves, P-related surface waves, and body waves. The conventional processing algorithm and procedure are not effective when attenuating surfaces waves and when recovering both P waves and S waves. It is also difficult to simply extend existing methodologies to OBC seismic data processing.

Two major theoretical approaches are widely used in seismic processing to attenuate surface waves and enhance the reflection signal quality from knowledge of elastic wave properties: (1) spectral analysis, such as short time Fourier transform (Nawab and Quatieri, 1998) and wavelet transform (Deighan and Watts, 1997), use different frequency properties of wave fields to recognize and separate surface waves; (2) polarization analysis in the time or frequency domain measures the degree of linearization and ellipticity to distinguish body waves and surface waves (Montalbetti and Kanasewich, 1970; Samson and Olson, 1980, 1981; Christoffersson et al., 1985; Esmersoy, 1984; Vidale, 1986; Magotra et al., 1987; Jackson et al., 1991; Diallo et al., 2006; and Gaiser, 2007). Both two approaches take into account either velocity, frequency or polarization only. However, because surface waves are characterized by all three attributes (low velocity, low frequency and high polarization), these approaches do not produce high-quality processed seismic dataset.

Conventional processing sequences (Yilmaz, 1987) are designed primarily for single component seismic data to obtain P waves or PS waves. In the shallow water environments, the collected seismic data suffers the low S/N issues. Because of this,

these conventional processing sequences result in an unreliable subsurface image. Accordingly, few successful applications have extracted the useful data from the two horizontal components in the Arabian Gulf region. And this environment also causes obstacles to obtain the exact velocity of P waves from the hydrophone and geophone components. In order to obtain shear wave information, multicomponent seismic data requires well-developed processing workflow.

1.2. Dissertation Research Objective

The objective of the present work is to improve the multicomponent OBC data quality though advanced processing algorithm and procedures for the shallow marine environment. With the knowledge of wave propagation characteristics, two surface wave separation approaches were employed in my analysis by extending theoretical approaches. New 4C OBC seismic processing procedure is proposed to obtain high resolution and high S/N dataset, which is essential for shear wave information extraction from horizontal components. The research outcome will represent a valuable tool in both attenuating the surface waves and enhancing reflection signals, which will result in better data for subsurface imaging and structure interpretation in the shallow marine exploration in the Arabian Gulf.

Despite a large number of studies, in addition to those cited here, none of them indicate a reasonably systematic method to investigate propagation properties of surface waves, which are mostly Scholte waves, and suppress those effects from the OBC data in the shallow marine acquisition. Exploiting the joint relationship of wavenumber, time,

frequency and polarization will contribute to the correct evaluation and attenuation of surface waves. In Part I, surface waves' propagation characteristics in the shallow water environments are investigated via one typical shot gather from one offshore in the Arabian Gulf. The purpose of this study is to design advanced filtering approach to separate surface waves from body waves on both hydrophone and geophones. In Part II, we further analyze how wavenumber, time and frequency effect polarization attributes and we invent a polarization filtering to attenuate residual surface waves and preliminarily identify shear waves. In Part III, we extend previous conventional approaches onto a 2D seismic line to procure P wave sections via designed processing sequence. In the shallow water environment, we expect to find strong PS-S waves in horizontal components due to the shallow water depth and strong reflectors near the seabed. In this work, the other major objective is to extract converted waves (PS-S) through advanced processing techniques. In this part, we utilize velocity models based on nearby log data and the knowledge established from modeling results to obtain a preliminary PS-S waves section.

1.3. Dataset and Geological Background

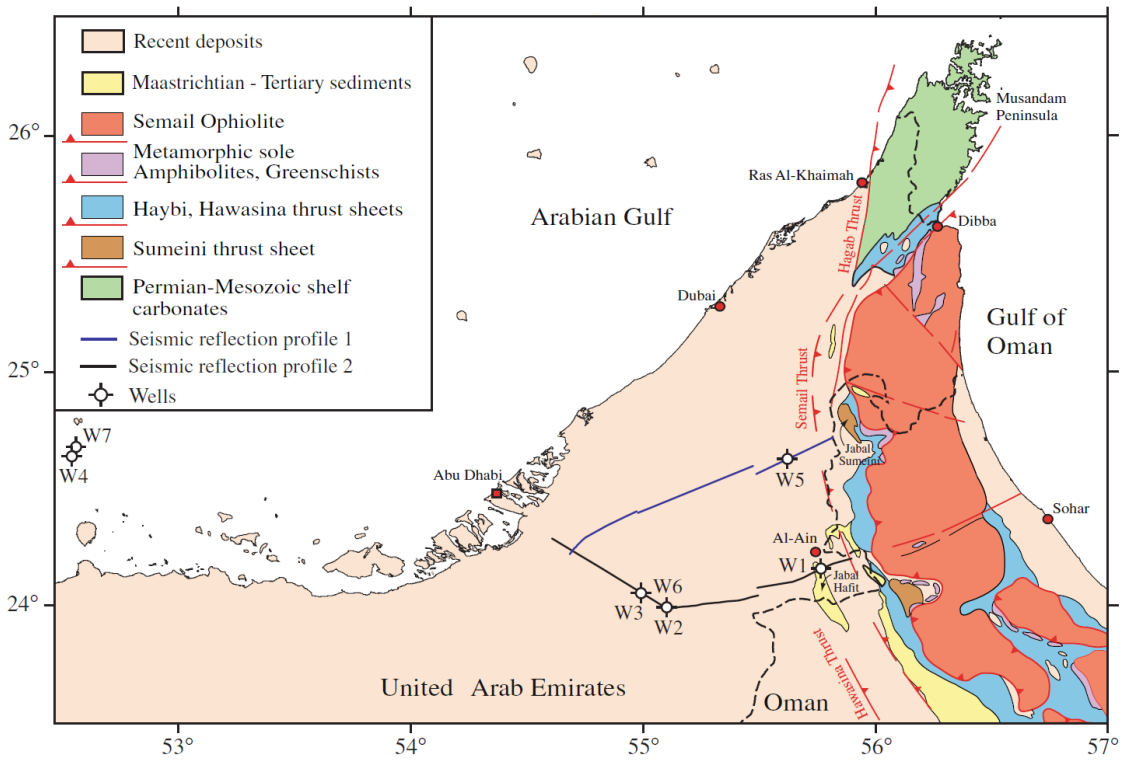

Figure I-1: Geological map of the Arabian Gulf Basin (Modified after Ali et al. 2013).

The Arabian Gulf Basin (**Error! Not a valid bookmark self-reference.**) is located in the Arabian Peninsula, which was a result of the Arabian plate subducting under Eurasian lithospheric plate (El-Awawdeh et al., 2008). In term of hydrocarbon resources, the Arabian Gulf Basin is the richest region of the World. This basin holds 55-68% of the recoverable oil and over 40% of gas reserves (Konyuhov and Maleki, 2006), according to different estimates. Structures of the gulf belong to the asymmetric foreland basin related to anticlines and synclines of the Zagros Orogen, which is a part of the

central Tethyan deformation belt. Sediments are predominantly dolomites, limestone, anhydrites or shales that were folded during the Neogene tectonic phase, indicating general low relief of the area during deposition. Over 70% of Gulf oil was generated from Jurassic-Cretaceous sediments, while others are from the Phanerozoic eon. The enormous thickness of carbonate rocks with excellent porosity and permeability are widespread, which provide the potential excellent storage for the huge volume of generated/migrated hydrocarbon. Moreover, the Zagros deformation has created fracture networks enhancing permeability. The ductile evaporate and shale beds play the role of regional fluid seals. With thermally matured organic-rich source rocks, porous and permeable reservoir rocks, and impermeable overlying seal rocks, the Arabian Gulf Basin is the world's largest source of crude oil.

The United Arab Emirates (U.A.E.) is a part of Arabian Peninsula and lies at its northeastern corner. In U.A.E., the existing oil and gas reservoirs are developed mainly in carbonates rock with high heterogeneous quality from the late Permian to middle Miocene in depth from 1000 to 5500 m. The sedimentary layers have wide and open folds in the shallow part and sub-seismic fault and fracture systems at greater depth (Sirat and Sun, 2006). A detailed structural determination with the exact location of faults from seismic is beneficial on reservoir production. However, major existing exploration issues in this area are that the water is overall very shallow, with a maximum depth of 20 meters and an average depth of 10 meters. Additionally, the area contains a hard bottom with P-wave velocity varying from 3 to 4.8 km/s. Both of these factors lead to highly dispersive surface waves. Surface waves in the dataset include the trapped

waves generated in the water column and the interface waves due to the hard sea-bottom, all of which influence the data quality and interpretation of the 4C data. Noise attenuation and signal enhancement are the most demanding job in processing the seismic data from the UAE offshore fields.

The 4C OBC survey used for this study was acquired over one giant offshore oilfield, located about 80km southwest of Abu Dhabi Island. The 3D survey surface areas was approximately 207 km^2, with water depth ranges from 6 to 20m and with average only 10 m. The source is a 2000 cu-in air gun fired at 5-meter depth with interval 25 meters. The receivers are 4-component sea-bottom cable with instrument spacing 25 meters. The time sampling interval is 2ms and the total recording time is 6000ms. The Arab formation (Upper Jurassic) and Khuff formation (Late Permian-Early Triassic) are two target oil and gas-bearing formations. The regional real is the anhydrite and dolomitic rock in the Hith formation. The 4C OBC data collected here is used to image the major structure, identify the target reflectors, study the reservoir heterogeneity, and better estimate shear wave.

1.4. Summary of the Dissertation

Multi-component seismic technology has been developed in the last several decades, with the aim to deliver better property estimation of reservoir rocks and pore fluid from shear waves. 4C seismic data, however, have been so far used in field applications only as better P-wave data, although in principle they could provide us with unprecedented information about the shear wave (S-wave) propagation in the earth.

There are several reasons that 4C seismic data have not been used to their full potential in the shallow water environment. The intrinsic complexity of seismic wave propagation in real earth materials recorded fully by 4C seismic data demands far more sophisticated analysis and interpretation than conventional one-component data such as pressure data offshore and vertical displacement data onshore. In addition, in the shallow-water environment of the offshore U.A.E in the Arabian Gulf, the characteristics of seismic wave propagation are dramatically different from other deep-water environments in most of the world where the 4C technology was originally developed. Inadequate knowledge on the shallow-water characteristics of seismic wave propagation could thus result in less optimal 4C acquisition design and processing in this environment.

This research is to gain a fundamental understanding of the characteristics of elastic wave propagation in shallow water environment of the offshore U.A.E. in order to improve the 4C technology for a better reservoir description and a better hydrocarbon recovery. Chapter II begins by focusing on the dispersion properties of surface waves on both hydrophone and geophones. Time-frequency analysis is used for revealing how spectral content changes with time. To extend analysis onto 3D, we introduce the time-frequency-wavenumber (TFK) transform using variable factor S transform to convert the seismic data from time domain to TFK domain. I investigated the distribution and characteristic of different wave-fields in TFK domain and designed a non-stationary filtering to separate the surface waves, based on their low frequency and low velocity properties.

In Chapter III, the impacts of residual Scholte waves is estimated on rotation. We extend existing covariance analysis onto TFK domain by designing a new filtering algorithm to separate body waves from surface waves. Three polarization attributes, ellipticity, linearity and rise angle, are calculated and used to suppress residual surface waves in the TFK domain. Surface waves are characterized by elliptical polarization of particle motion, while body waves are liner polarization. Combing with time, frequency and wavenumber, polarization attributes act as an effective tool for wave field identification and separation.

In Chapter IV, I integrated the filtering algorithm with regular processing procedure, such as velocity modeling, NMO and stacking, to get the high-quality processed seismic data for interpretation. The goal of this section is to image earth structure correctly using both P waves and S waves extracted from the pressure component. Furthermore, we investigated the existence of shear wave in horizontal components and image structure using processed S wave from the horizontal components. This is critical for optimal estimation of rock properties for reservoir characteristic.

Finally, the structural sections using both P and S waves from all four components are obtained through above filtering algorithms and the processing sequence. Combined with the log data, they can image earth structure correctly; the section using the S-wave matches approximately the result using P-wave from the pressure components. This direct S wave information from the seismic will benefit further interpretation and AVO analyses.

CHAPTER II

IMPROVING OBC DATA QUALITY IN SHALLOW-WATER ARABIAN GULF THROUGH ADVANCED TIME-FREQUENCY ANALYSIS

2.1. Summary

Features of subsurface structure of interest in the exploration geophysics field are three dimensional in nature (Ylmaz, 2001). Four-component (4C) Ocean-bottom cable (OBC) records the full three-dimensional ground motion via 3C geophone as well as the water pressure via hydrophone. It is the preferred method of overcoming subsurface complexity and leads to avenues in elastic wave imaging in marine environments. Therefore, in both exploration and production, there is an increasing demand for extracting additional and more precise wave field information from multi-component seismic data.

In order to obtain elastic information of the sub-sea-bottom, both P- and S- wave velocity fields should be precisely estimated. In the deeper water environment, P/S wave decomposition has led to a number of successful applications in direct hydrocarbon detection, structural imaging, and lithology discrimination (Tatham and McCormack, 1991). However, some of the world's important oil and gas fields are in the Arabian

---

∗Part of the data reported in this chapter is reprinted with permission from "Analysis of Surface waves in shallow water environment of the Persian Gulf using S and t-f-k transform." by Zhang, Z., Sun, Y.F., and Berteussen, K., 2010. *Proc.*, 80th SEG Annual International Meeting, Denver, Colorado, 17-22 October, 3723-3728. Copyright 2010 by SEG.

Gulf, where the average water depth could be as shallow as 10-15m (Sun and Berteussen, 2009a, 2009b). Due to this unusually shallow water depth and the hard sea bottom, 4C OBC seismic data recorded in those areas are severely degraded by highly dispersed and scattered surface waves. They produce severe data-quality issues which result in inaccuracies in the wave-field decomposition and further influence the interpretation of seismic attributes. On the other hand, when the surface waves are measured with sufficient amplitude resolution, its dispersive characteristics can be used to infer the shear-wave properties of the seabed. They could be useful to probe sediment property of the sea bottom where log data are usually not available. Therefore, a good separation between reflection signals and surface waves is an essential prerequisite for the success of multi-component exploration in these shallow water environments.

2.2. Literature Review

Studies on the surface wave attenuation have been taken over many decades. Numerous approaches have been proposed and implemented for surface wave extraction or elimination include windowed frequency filtering, phase shift analysis (Sato, 1955), FK filtering (Yilmaz, 2001), short-time Fourier transform (STFT) filtering (Nawab and Quatieri, 1998) and wavelet transform (WT) filtering (Deighan and Watts, 1997). Frequency filtering, phase shift analysis and FK filtering are theoretically designed in the frequency domain, based on Fourier Transform, and have the same effect on the whole time series. Those characteristics are more suitable to suppress the linear noise. However, the non-stationary seismic signals have varying frequency content in time,

which bring difficulties of defining a single, appropriate rejection zone in the Fourier domain. To overcome this problem, filtering can be designed using the STFT or WT. Nawab and Quatieri (1998) firstly used time windowing and introduced STFT. However, there exists a compromise between window sizes and frequency precision, then the performance of the STFT based filter is frequency dependent (Cohen, 1995). Alternatively, WT can decompose the trace into time-scale wavelet coefficients which allow defining specific filtering zones affected by noise (Sinha et al., 2005, 2009). In most of the applications, the wavelet family implements octave scaling of frequencies and there is no shape change over entire time; both of these two reasons result in an under-sampled representation of high frequencies and an oversampled representation of low frequencies (Stockwell, 2007). Most of above methods only consider on one aspect of surface waves, which may either fail to effectively eliminate surface waves or lead to unwanted artificial waves to body waves.

Combing the advantages of STFT and WT, the S transform (Stockwell et al., 1996) can be considered as a frequency-depend STFT or a phase-corrected WT (Dash et al., 2003). S transform has been widely used as a valuable tool for the time-varying signal analysis. Successful applications demonstrated its advantages in seismic data processing, such as spectral decomposition (Deng et al., 2007), magnetic resonance data (Zhu, et al., 2003; Goodyear et al., 2004), and estimation on the first arrivals of the P waves (Parolai, 2009). S transform is also implemented in filtering design (e.g., Pinnegar and Eaton, 2003; Zhu et al., 2003; Goodyear et al., 2004; Schimmel and Gallart, 2005,

2007; Askari and Siahkoohi, 2008). This research also extends S transform advantage on noise separation.

2.3. Theory

2.3.1. Standard S Transform

The S transform can conceptually be viewed as a hybrid of STFT and WT. Instead of a pre-selecting window length, it adopts the Gaussian window, whose width scales inversely and height scales linearly, with the frequency, to decompose the signal into time-frequency independently (Askari and Siahkoohi, 2008).

The S transform of a time series $u(t)$ is defined as (Stockwell et. al., 1996):

$$S_x(t, f) = \int_{-\infty}^{+\infty} u(\tau) w(t-\tau, \sigma(f)) \exp(-j2\pi f\tau) d\tau$$

with a constraint

$$\int_{-\infty}^{+\infty} w(t-\tau, \sigma(f)) d\tau = 1$$

where the $w(\tau, f)$ is the Gaussian window

$$w(t, \sigma(f)) = \frac{1}{\sigma(f)\sqrt{2\pi}} \exp\left(-\frac{t^2}{2\sigma^2(f)}\right)$$

where τ is the time and f is the frequency, and t is the parameter that controls the position of the Gaussian window in the time domain.

The S spectrum is invertible; and the inverse transform algorithm is (Stockwell et al., 1996):

$$u(t) = \int_{-\infty}^{+\infty} \left[\int_{-\infty}^{+\infty} S(\tau, f) d\tau \right] \exp(j2\pi ft) df .$$

Compare to wavelet analysis, S transform identifies the real and the imaginary parts of the spectrum separately and preserves both phase and amplitude spectrum, while wavelet transform could not provide absolute phase of the signal (Sahu, et. al., 2009). The similarity between S transform and the STFT is that they are both derived from the Fourier transform, which is the time series multiplied by a time-shift window (Stockwell, 2007). However, unlike STFT, the standard deviation in S transform is actually a function of frequency, f , defined as

$$\sigma(f) = \frac{1}{|f|} .$$

Consequently, both time and frequency adjust the shape of the window function. Therefore, the advantage of S transform is the ability to provide multi-resolution analysis of non-stationary signals and keep the absolute phase feature of each frequency, which could not be achieved either by STFT or WT.

Even though the potential of S transform has been recognized as a valuable tool in seismic signal analysis in the oil/gas industry for years, it is burdened with poor time-frequency concentration due to the nature of the Gaussian window. There is no parameter in Gaussian function to adjust the window width in time or frequency, which is defined as a reciprocal of the frequency (Sejdic, et. al., 2007). To overcome these issues, Sejdic et. al. (2007) and later Sahu et. al. (2009) introduced the optimized S transform, which provide a better resolution control via the modified Gaussian window function.

2.3.2. The Variable-Factor S Transform

The common idea of the improved S transform is to introduce a set of additional parameters into the Gaussian window, which permits the use of windows with frequency dependence in their shape as well their width and height (Pinnegar and Mansinha, 2003a, 2003b; Sejdic, et. al., 2007; Sahu et. al., 2009; Todorov and Margrave, 2010). Hence the generalized S transform is defined as:

$$S(t, f, \beta) = \int_{-\infty}^{\infty} x(t)\omega(t-\tau, f, \beta)\exp(-2\pi i f\tau)d\tau$$

In practice, ω is replaced with a specific window, and β is replaced with a set of parameters (Pinnegar and Mansinha, 2003a).

Window function is the key to the resolution in the special analysis. A wider time window results in better frequency concentration in the time-frequency plane, at the cost of poorer time resolutions. A narrower time window provides better time resolution, but leads to worse frequency resolution. Figure II-1 shows Gaussian window at different frequencies. Low frequency results in a wider time window, while high frequency leads to a narrower time window. Different values of parameter τ lead the horizontal shift along t axis.

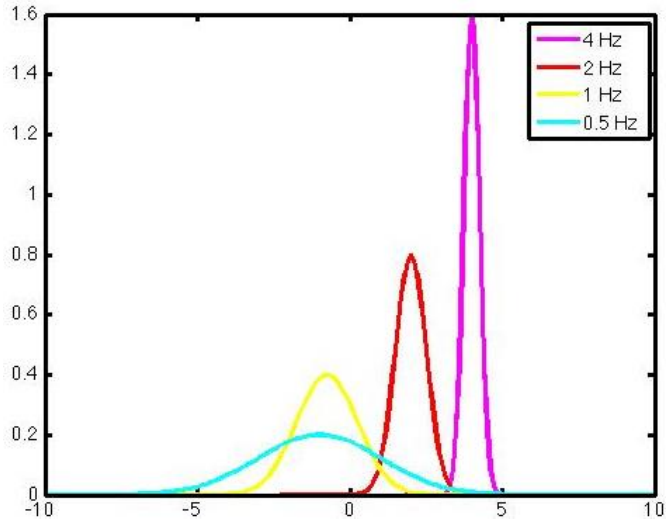

Figure II-1: Gaussian window at different frequencies (f1 = 4 Hz, f2 = 2Hz, f2 = 1Hz and f4 =0.5Hz). With frequency decreasing, the width of the window increases.

The advantage of the improved S transform is the use of windows where the width, height and shape are frequency dependent. In this paper, we implement Todorov's variable-factor S transform (2010), in which the standard derivation of the window is:

$$\sigma(f) = \frac{k(f)}{|f|}.$$

Based this equation, the proposed variable-factor S transform can be represented as:

$$S_x(t,f) = \int_{-\infty}^{+\infty} u(\tau) \frac{|f|}{\sqrt{2\pi}k(f)} \exp\left(-\frac{(\tau-t)^2 f^2}{2k^2(f)}\right) \exp(-j2\pi f\tau) d\tau$$

where $k(f)$ is defined as:

$$k(f) = \alpha f + \beta$$

in this paper. The value of $k(f)$ indicates the number of the period of a Fourier sinusoid within one standard derivation of the Gaussian window (George et al., 2009). By

increasing this value, the transform will increase the frequency resolution with a corresponding loss of the time resolution.

Figure II-2 shows how the shape of the Gaussian window changes with parameters α and β. Comparing with regular Gaussian window, modified Gaussian window has relative narrow window width at specific frequency with positive value of α and β. The regular Gaussian window can be considered as the modified window function with α=0 and β = 1. Parameter α dominates the shape changes; with increasing value of α, the width narrows down. Parameter β provides the fine-tuning after α set.

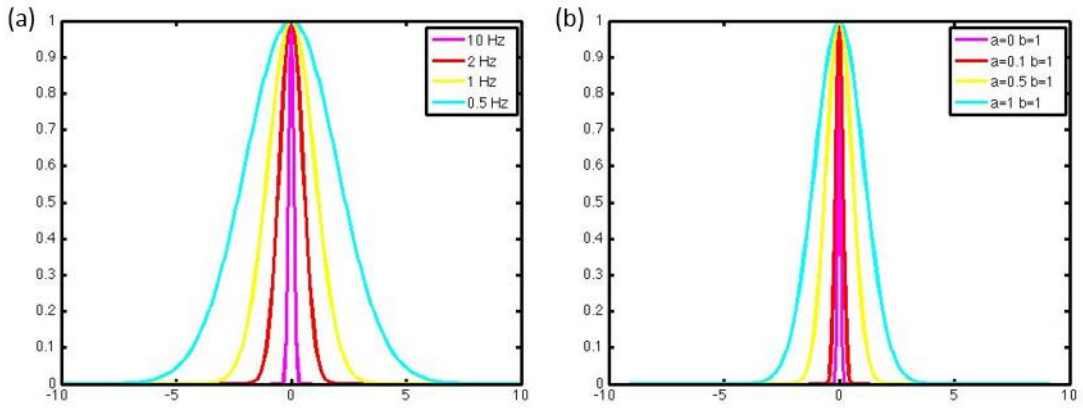

Figure II-2: (a) Gaussian window at different frequencies. (b) Modified Gaussian window with parameter α and β. (f1 = 10 Hz, f2 = 2 Hz, f3 = 1 Hz and f4 = 0.5 Hz)

Consequently, we can control the time and frequency resolution through parameters α and β. As the width of the window is dictated by the frequency, it is apparent that the window is wider in the time domain at lower frequencies, which means the window provides good localization in the frequency domain for low frequencies

(Stockwell, 2007). Due to the low frequency spectrum of surface waves, this property makes the variable-factor S transform more appropriate for our analysis.

2.3.3. The TFK Transform

In the FK domain, the various types of seismic events are partitioned from one to another, compared with the time-space domain representation. This property makes the FK domain a suitable option for surface wave elimination and extraction due to the distinctive dip information of surface waves and reflections. On the other hand, the nonstationary filters based on nonstationary transforms, such as the CWT, STFT or S transform, could provide more accurate phase picking estimates than approaches based on standard filtering procedures, especially for the data obtained from shallow water environments. Based on these two concerns, we can make a joint representation of the signal in a TFK domain, rather than analyzing signals in only the time-space or frequency-wavenumber domain. For a given input signal, the signal in TFK domain can be calculated through:

$$TFK(\tau, f, k) = \int_{-\infty}^{+\infty}\int_{-\infty}^{+\infty} u(t,x)\exp(-j2\pi kx)w(t-\tau,\sigma(f))\exp(-j2\pi f\tau)dxd\tau,$$

where $w(t,\sigma(\alpha,\beta,f))$ is defined as:

$$w(t, f, \alpha, \beta) = \frac{|f|}{(\alpha f+\beta)\sqrt{2\pi}}\exp(-\frac{f^2t^2}{2(\alpha f+\beta)^2})$$

The data is first transformed from the time-space domain to the time-wavenumber domain through 1D Fourier transform over the spatial variable, then the variable-factor S transform over time (Zhang, et. al., 2010, 2015). The integration of

TFK results over time can be regarded as the FK transform of $u(t,x)$. The TFK transform appears to have advantages over the normal FK transform when the FK panel of seismic data varies over time, especially for the data obtained from the shallow water environment.

2.4. Method

The FK filter transform separates the original overlapping dipping events in the FK domain on the basis of their dips (Ikelle, 2005). Following the same idea, we propose a nonstationary FK filtering that combines the de-noising in the FK domain with the filtering of the coefficients in the variable-factor S transform time-frequency plane.

Filtering in time-frequency representation, such as the TFK domain, multiplies the spectrum TFK(t,f,k) with a weighting function F(t,f,k), and this assigns high values to useful signals and low ones to unwanted signals. Consequently, the filtered output time series is

$$u_{filter}(t,x) = \int_{-\infty}^{+\infty}\int_{-\infty}^{+\infty}\int_{-\infty}^{+\infty} TFK(\tau, f, k)F(\tau, f, k)d\tau \exp(j2\pi ft)df \exp(j2\pi kx)dk$$

We perform our method in the following steps:

(1) Apply the TFK transform on the original data and get the 3D result TFK(t,f,k) in TFK domain.

(2) Identify the time-frequency relationship f(t) of surface waves based on specific wavenumber k and the frequency-wavenumber relationship f(k) of surface waves based on specific time t.

(3) Design a suitable filter F(t,f,k) in the TFK domain on the basis of TF(k) and FK(t) to separate surface waves.

(4) The filtering is imposed on the resulting spectrum within which the undesired energy is zeroed out.

(5) Invert the filtered record through an inverse ST and an inverse FT.

2.5. Results

Figure II-3a-d shows one typical shot gather in this studied data set. It is evident that the recorded surface waves are highly spatially aliased and dispersive. In the hydrophone component (Figure II-3 a) and vertical geophone component (Figure II-3 b), it shows very strong Scholte waves (Label A, D in Figure II-3), P-related interface waves (Label B in Figure II-3), which mask all the reflection signals (Label C in Figure II-3) except of some near offset traces. Because of the inadequate time delay between shots, the Scholte waves from both the present shot (Label D in Figure II-3) and the previous shot (Label A in Figure II-3) are present in the shot record, which bring severe contamination to reflection signals (Sun and Berteussen, 2010). This contamination affects long-offset reflection signals even up to 3 seconds, which reduce the quality of far-offset AVO analyses that help delineate carbonate reservoir rock types and

permeability heterogeneity. Also, because of the differences between the physical measurement characteristics of hydrophones and geophones, the vertical component is compromised by surface waves more severely than the hydrophone record. The situation is even worse in the horizontal components (Figure II-3 c, d) where all the reflection signals are destroyed by the surface waves. All the contaminations appearing on the vertical component due to surface waves also severely reduce the S/N of inline/crossline geophone record. The horizontal geophone, unlike the vertical geophone, also record the strong acoustic waves trapped in the water layer that acts like a wave guide enhanced by the shallow water environment and a hard sea bottom. Meanwhile, the reflected converted waves recorded in horizontal components are much weaker than the P wave response, which is also a reason for the degraded data quality. In this case, the appearance of extremely low S/N on the horizontal components is thus attributed more to the sediment physics and less to geophone coupling as conventionally thought.

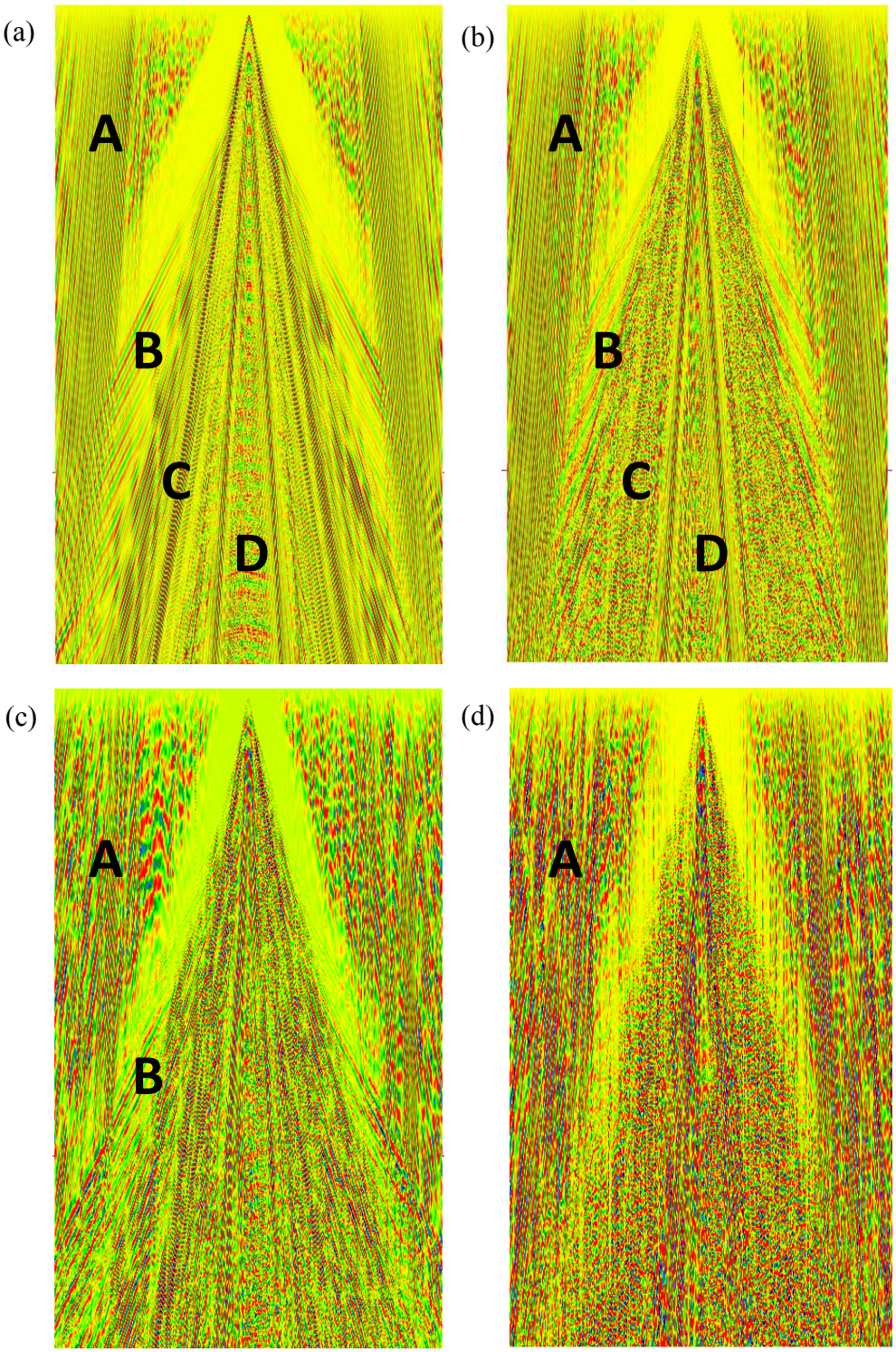

Figure II-3: A portion of the raw shot record after AGC (a) Pressure component (b) Vertical component (c) Inline component (d) Crossline component.

Figure II-4 shows the typical amplitude spectra of the 4-component sensors using a near-offset 4-component set in Figure II-3. The surface waves, with a dominate frequency about 10 Hz, have energy that is mostly concentrated in the frequency band of lower than 15 Hz on all the four components of the data. The signal strength of the hydrophone is approximately hundred times stronger than the three geophone receivers, which produce severe data-quality issues and result in inaccuracies in the wave-field decomposition and less use of the geophone components. The decomposition process would be effective if one is able to adequately suppress surface waves in the individual hydrophone and vertical geophone dataset prior to the PZ summation and further more processing.

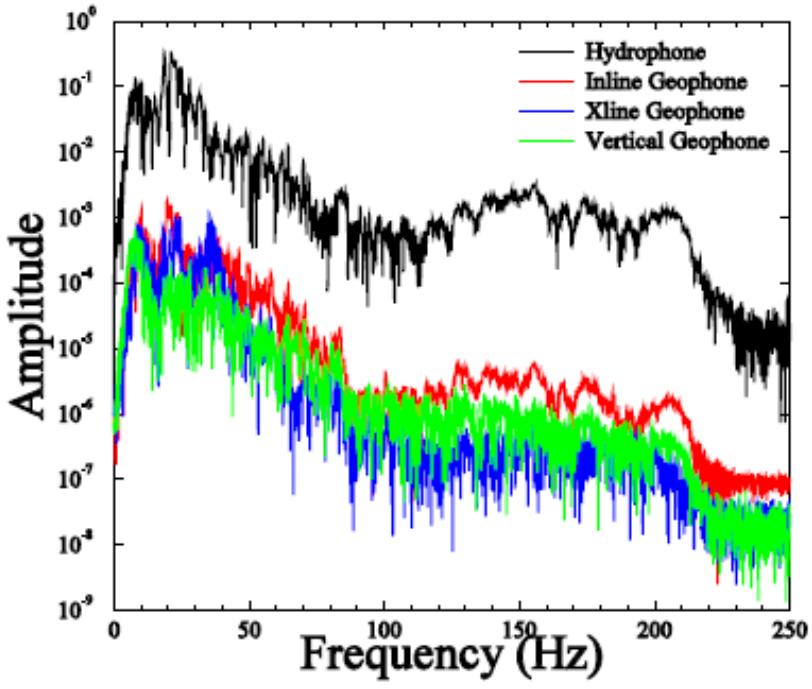

Figure II-4: Typical spectral of 4-component sensors from the shot in Figure II-3.

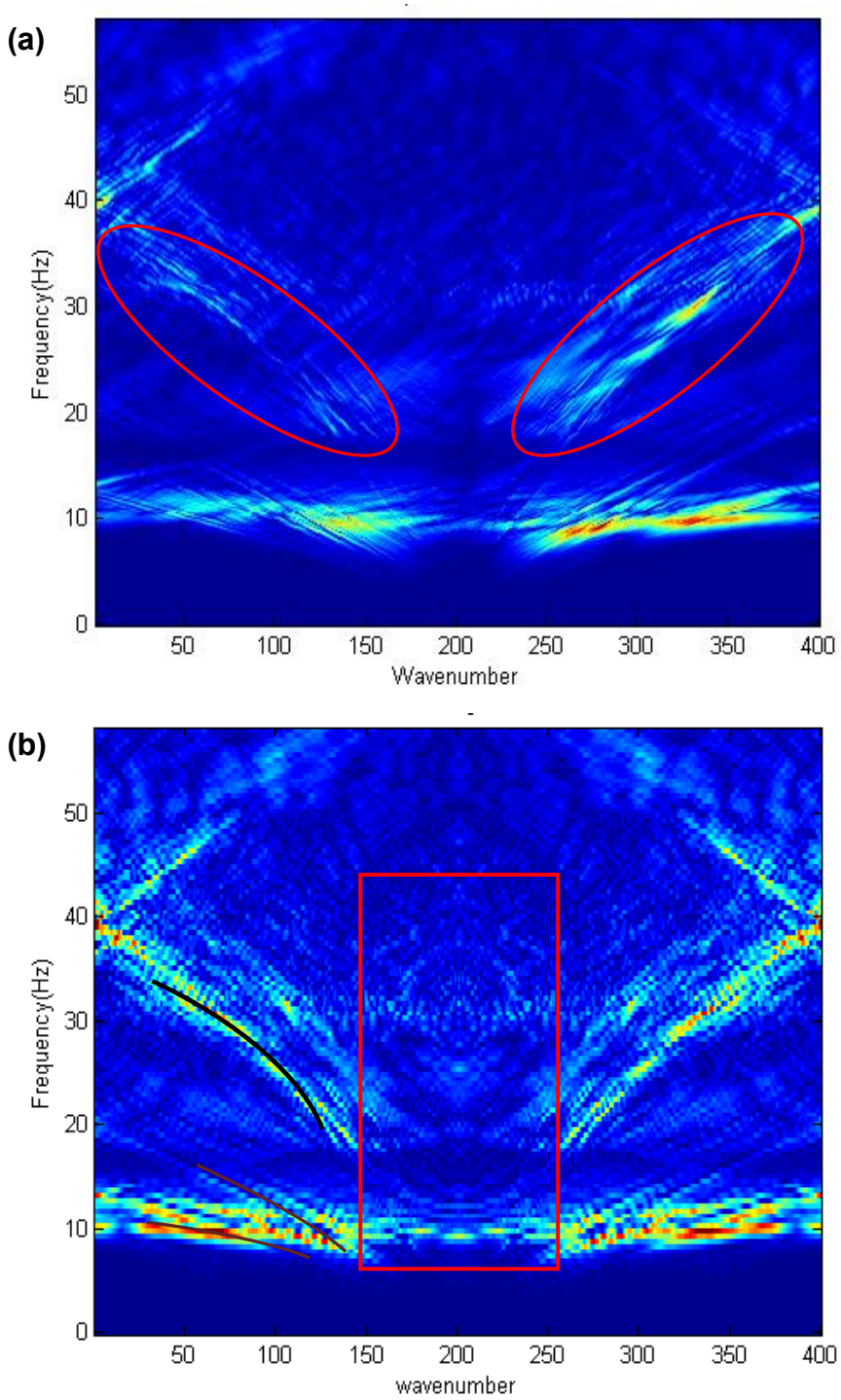

Figure II-5: (a) Frequency wavenumber spectrum of the Inline component using Fourier transforms. (b) Frequency-wavenumber spectrum of the Inline record at t = 600ms using TFK transform.

Figure II-5 shows the comparison of FK spectrum of inline component record in Figure II-3 between using FK transform and TFK transform. In the traditional FK domain, different seismic events affect each other and the energy is not balanced (red circle in Figure II-5a) due to collective interferences of seismic events. In addition, the reflection signal is very weak, which brings the challenge of defining a rejection zone for attenuation. Compared to the traditional FK transform (Figure II-5a), different seismic events are obviously separated, and the reflection signal (red box in Figure II-5b) is enhanced. The spatial aliasing of strong surface waves still affects the signal band of reflected waves, but the situation has improved nonetheless. The dipping events map onto curves instead of straight lines in the f-k domain (the curves lines in Figure II-5b), which means the velocity and frequency of the Scholte waves change in the shallow environment. The velocity of Scholte waves is in the range from 450m/s to 2100m/s. The dominant frequency of P-related interface waves is in the range from 20 Hz to 50Hz, with a velocity that varies from 1300 m/s to 3500m/s, which are more severely aliased than other waves in the seismic record.

Following the steps in previous section, we could design the diversity weighting function to extract or remove the Scholte waves, P-related interface waves and reflected waves separately on the multi-panel FK spectrum (Figure II-6) after the TFK transfrom. Figure II-7, Figure II-8 and Figure II-9 demonstrate a smaller set of traces of the hydrophone, vertical and inline geophone component data after adaptive subtraction of the surface waves, respectively. The data significantly cleaned up by the advanced filtering and the primary and multiple reflections can be seen at this stage. Since PZ

summation would be only minimally effective at removing surface waves, the improvement on the geophone components data benefits the further processing and interpretation. Instead of treating surface waves as unwanted noise, we preserve the P-related surface waves (Figure II-10) and Scholte waves (Figure II-11) which are from both the present and previous shots. Surface wave dispersion arises because of the velocity stratification of the Earth's interior, longer wavelengths penetrating to greater depths and hence sampling higher velocities. A well abstraction of surface wave brings the chance to infer the shear-wave properties of the sea bed. Very low velocity Scholte wave occurs in shallow environment. This observation leads us to further study the geology properties of the seafloor sediment.

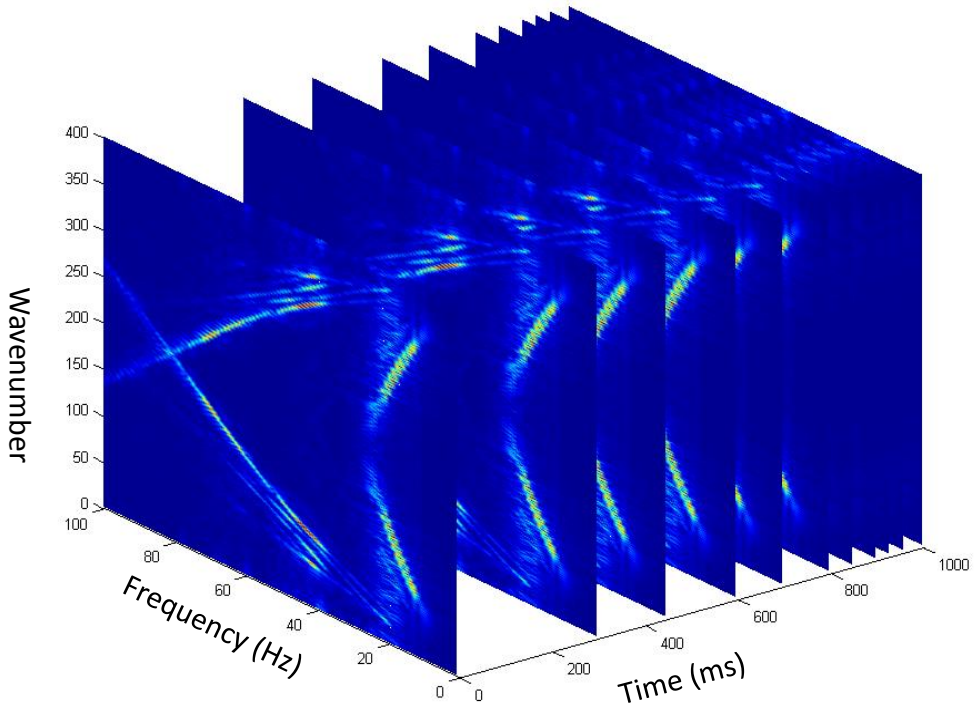

Figure II-6: Multi-panel FK spectrum after the TFK transform.

2.6. Conclusions

It is well known that Ocean Bottom Seismic in the Arabian Gulf suffers from the fact that there are very high velocity layers at very shallow depth. This traps the energy and causes strong interface waves as well as numerous multiples. The total effect is a degrading of the seismic quality. In this paper, we propose a nonstationary FK filter which allows dynamic analysis of the spectra of different seismic events over time. It is ideally suited to separate the effect of surface waves in the shallow water OBC survey. This method helps enhance the data quality of all 4C components for seismic data interpretation. In addition, the extracted surface waves can provide an additional means of predicting shear velocity of the seabed. On the other hand, surface wave in this environment can be used to predict shear velocity, attenuation of the seabed. Therefore, a good separation between reflection signals and surface waves is an essential prerequisite for the success of multicomponent exploration in these shallow water environments.

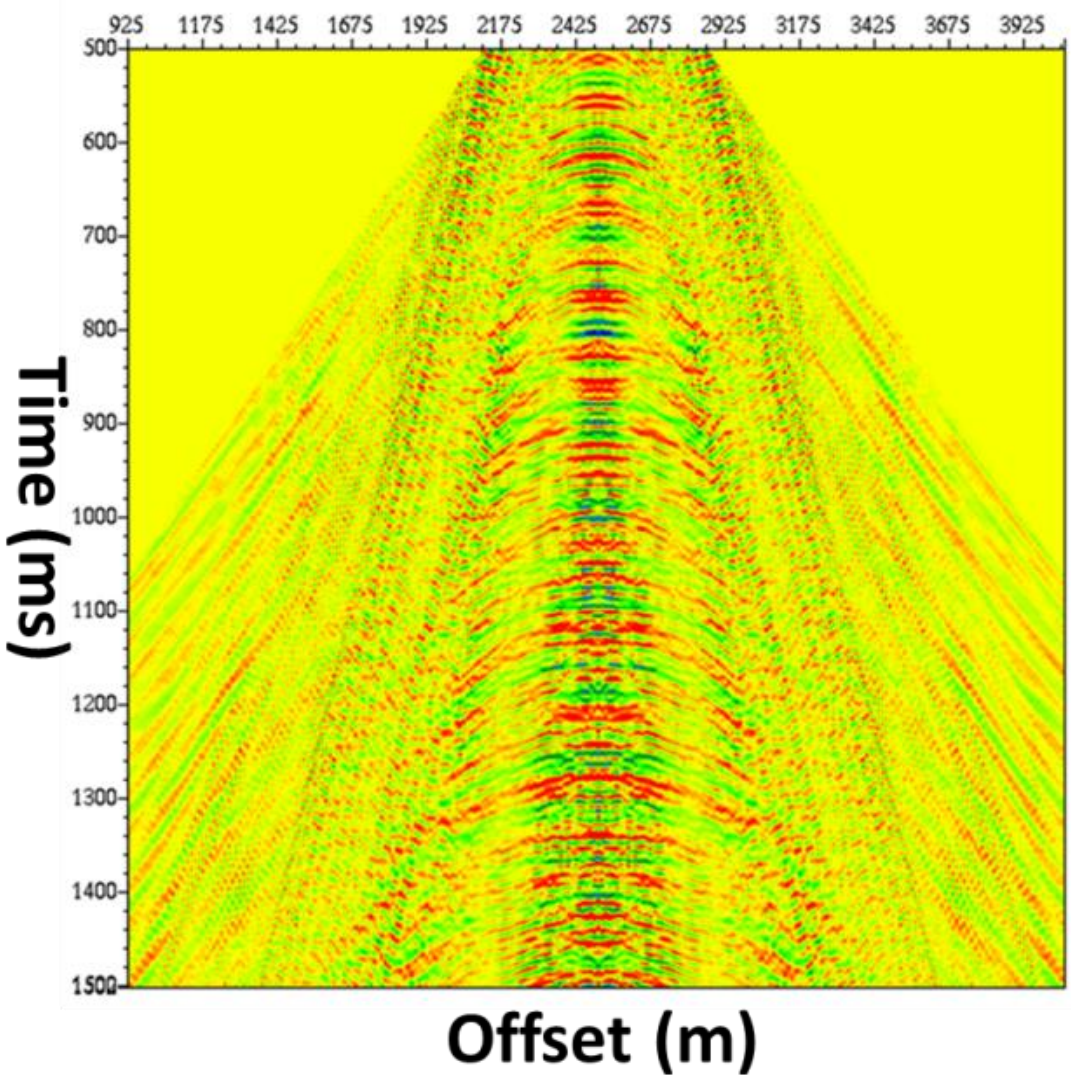

Figure II-7: Portion of the pressure component after filtering.

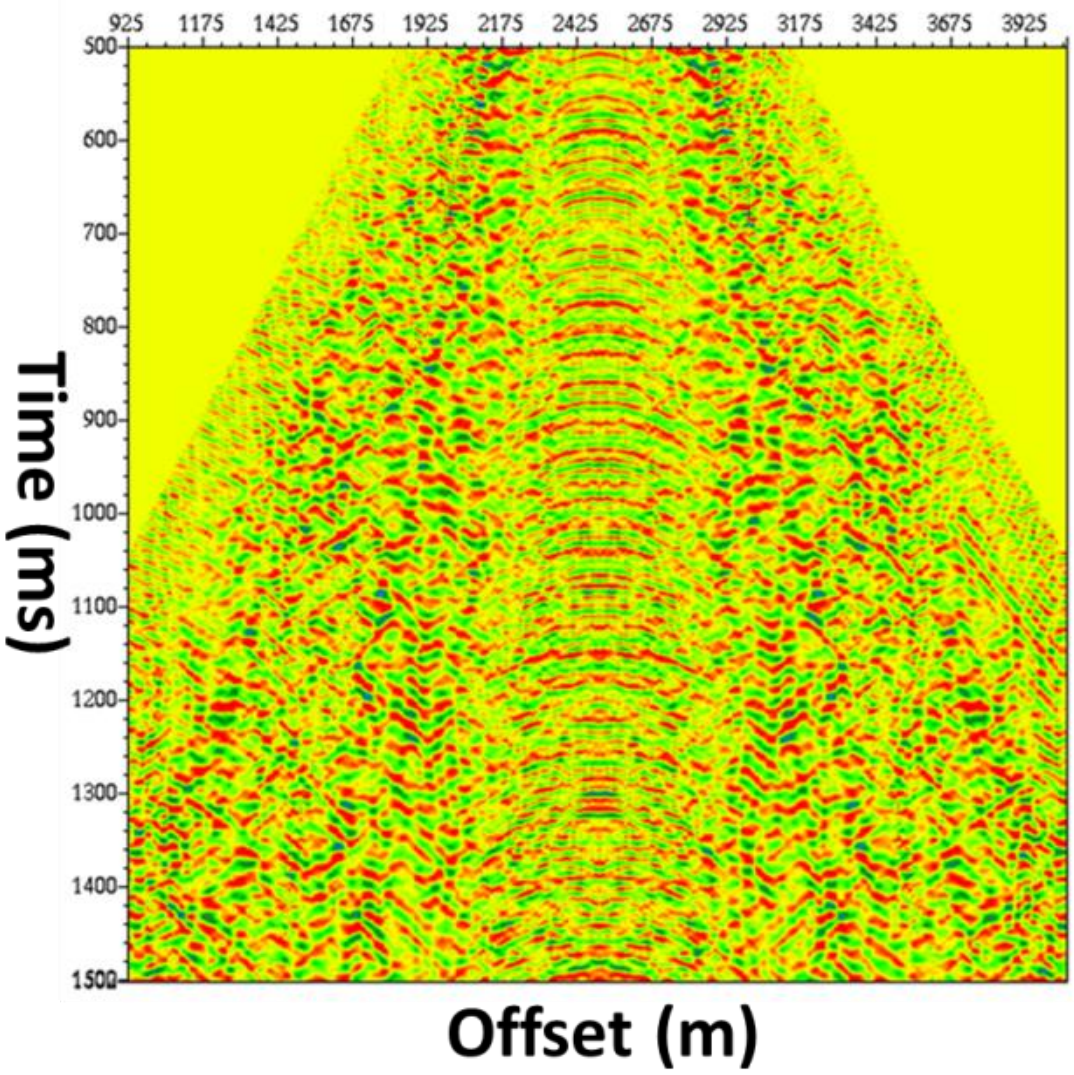

Figure II-8: Portion of the vertical component after filtering.

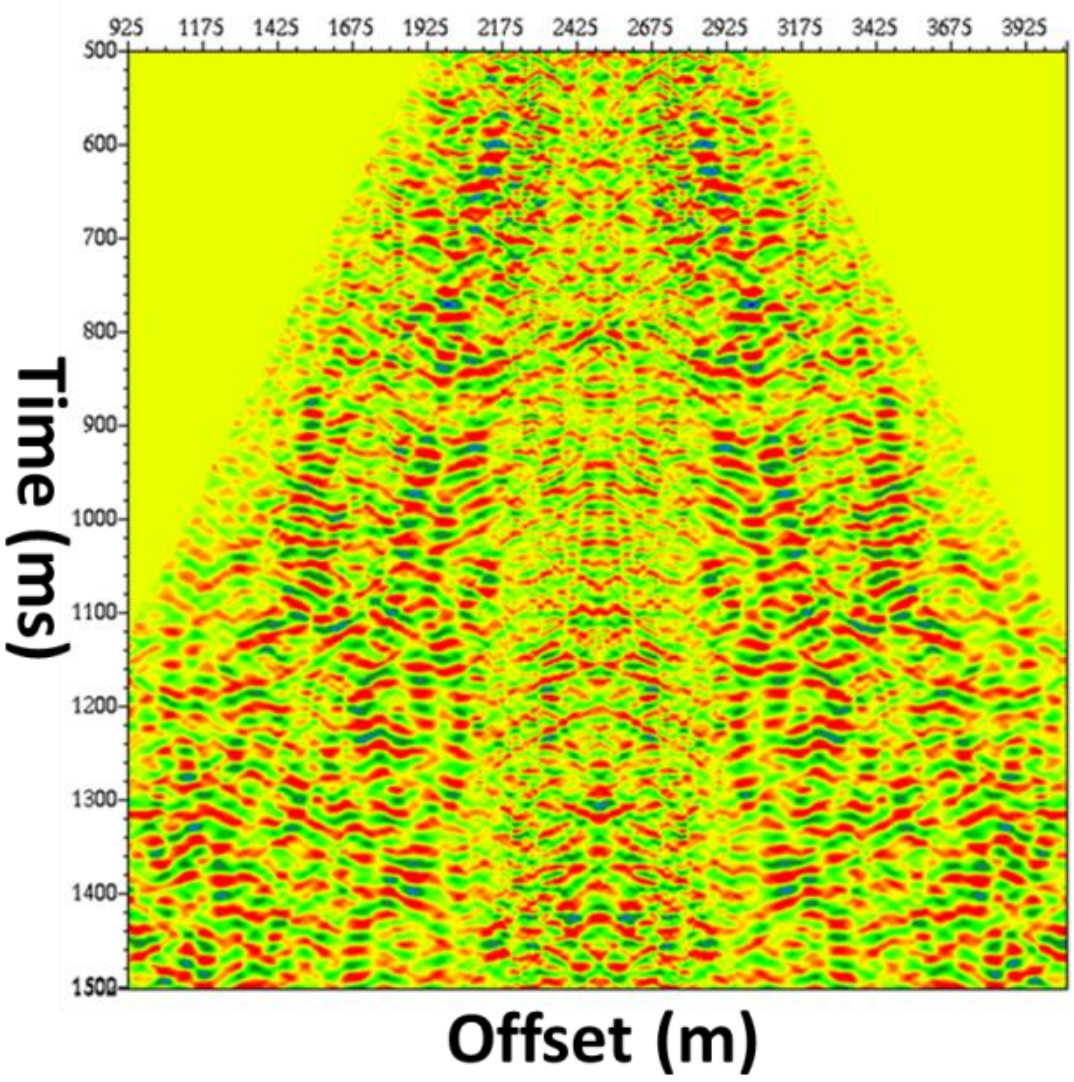

Figure II-9: Portion of the inline component after filtering.

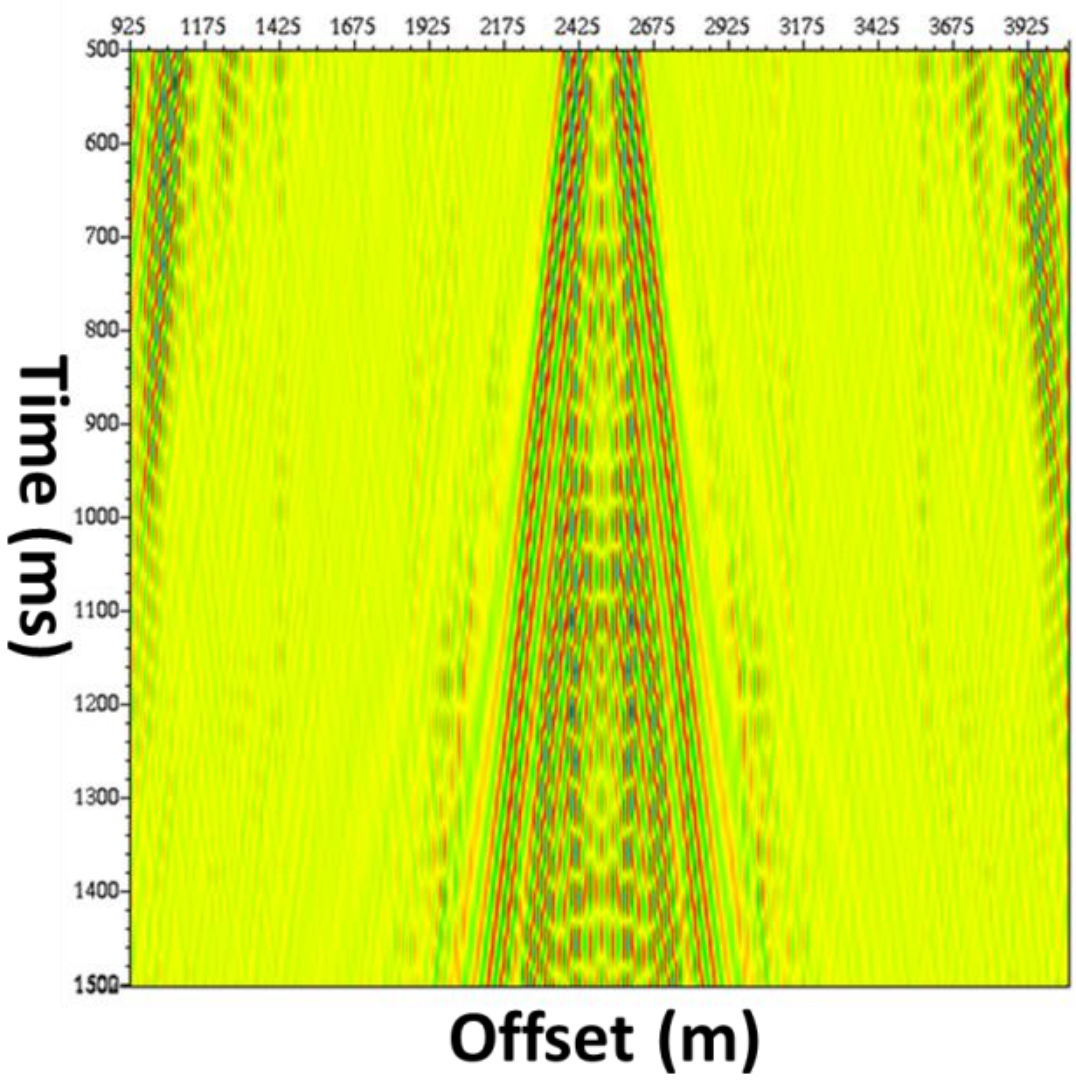

Figure II-10: Extracted Scholte waves from the pressure component.

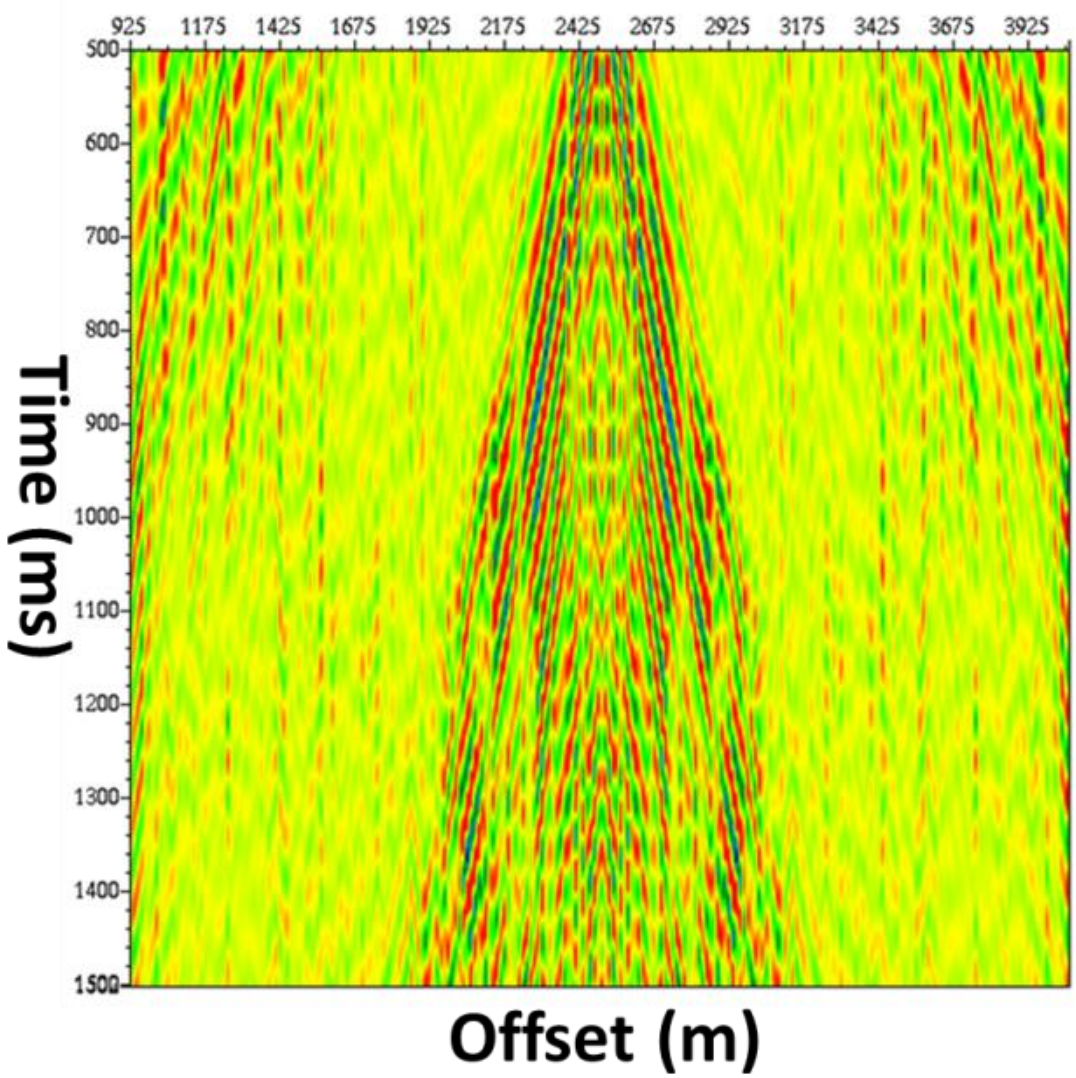

Figure II-11: Extracted P-related surface waves from the pressure component.

CHAPTER III

EFFECT OF SCHOLTE WAVE ON ROTATION OF MUTI-COMPONENT OBC SEISMIC DATA IN SHALLOW WATER ENVIRONMENT OF THE ARABIAN GULF*

3.1. Summary

Extracting both shear-wave (S) and compressional (P) energy from the multi-component seismic data is beneficial to estimating subsurface elastic properties and interpreting mode conversions. Because the orientation of geophones is not ideal in the field acquisition, reorientation is an important procedure to provide reliable information about the geophone direction and polarity for the P/S wave decomposition. Polarization analysis is designed to identify different phases, based on covariance matrix analysis. It

---

*Part of the data reported in this chapter is reprinted with permission from ". Improving OBC data quality of the geophone components in shallow-water Persian Gulf through advanced time--frequency analysis." by Zhang, Z., Sun, Y.F., and Berteussen, K., 2012 Proc., 82nd SEG Annual International Meeting, Las Vegas, Nevada, 4-9 November, 1131-1135, Copyright 2012 by SEG and from "Effect of Scholte wave on rotation of multi-component OBC seismic data in shallow water environment of the Arabian Gulf." by Zhang, Z., Sun, Y.F., and Berteussen, K., and Ali, M., 2-13. *Proc.*, 83rd SEG Annual International Meeting, 22-27 September, Houston, Texas, 1233-1238, Copyright 2013 by SEG.

cannot lead to an accurate directional analysis if signal and noise have similar spectral characteristics, or if the S/N is high in the original data. Without efficient removal of the Scholte waves, conventional polarization analysis can generate severe artifacts and render the data almost useless for the reservoir characterization. Therefore, a better and accurate preprocessing is needed before rotating multicomponent OBC data in this shallow water environment for the reservoir property estimate. Time or frequency-dependent polarization followed by a bandpass filtering is the conventional polarization analysis. Highly dispersive and aliased surface waves collected in the Arabian Gulf present unique challenges to these methods for the following reasons: First, due to the extremely shallow water depth and the hard sea bottom, the recorded strong surface waves occupy the same regions of FK and FX as the reflected waves. Simple filtering methods are incapable of directly handing these situations. Second, scattered noises induce phase differences between different components of motion. Finally, due to the interference between body waves and surface waves, it is very difficult to recover the polarization attributes of each individual wave field in a single domain. These facts above motivate us to develop a more sophisticated TFK polarization analysis method, which could be more efficient in dealing with the complex wave propagation and the very low S/N of the OBC data in the shallow water environment. We further propose a two-step rotation work-flow, in which raw data first go through non-stationary FK filtering and then TFK polarization analysis.

3.2. Literature Review

Due to the inertial effects of water layer, the discontinuity of horizontal motion generates large amplitude and phase distortions in the form of rotations when the water and sea-bottom motion are out-of-phase (Duennebier and Sutton, 1995). The receiver cannot accurately record the true ground motion in the three orthogonal directions. Those adversely influence the processing results for the converted wave extraction from horizontal components and PZ summation for the water column multiple suppression. To minimize the detrimental effects of the geophone coupling, 4C data must be rotated from field-acquisition coordinates to radial/transverse space where the radial component is parallel to the source-receiver vector.

The polarization properties of elastic waves are related to the source-receiver direction and affected by elastic properties of subsurface. Many techniques are proposed based on the employment of coherence estimation for the polarization analysis of multi-component data. To characterize the particle motion, the techniques basically fall into two categories: covariance-based analysis using triaxial data from a single sensor and data analysis from arrays of sensors. Comparatively, covariance-based analysis on a single sensor is more maturely developed and widely used in the field of seismic oil exploration. These implementations have two major objectives: 1) to design filters to distinguish events in complex and overlapping wave-fields and (2) to estimate the direction of particle motion.

Theoretical development of the polarization analysis was first been given by Stratton (1941) for implementation in the magnetic field. The polarization attributions of

plane waves in the unbounded-isotropic media were described through a polarization ellipse. With recent advances in seismic acquisition techniques, polarization analysis allows us to extract more polarization attributes by computing this polarization ellipse from the multicomponent seismic data. Flinn (1965) then introduced the polarization filtering using recti-linearity and the direction of particle motion for the multi-component seismic data processing. Different approaches (Samson and Olson, 1981; Jurkevics, 1988; Shieh and Herrmann, 1990; Perelberg and Hornbostel, 1994) were proposed based on this research for identification and separation of different wave fields in the time domain. Jackson et al. (1991) implemented the singular value decomposition (SVD) to obtain the polarization attributes with the assumption that the background noises are random. The instantaneous polarization attributes (Morozov and Smithson, 1996) was proposed for surface waves suppression and shear wave splitting identification in the frequency domain. Diallo et al. (2006) combined the previous work and brought the time-frequency concept into the polarization analysis. Galiana-Merino et al. (2011) implement the time-frequency polarization analysis for seismic noise array processing for microzonation studies. Tan et al. (2013) utilized S transform to achieve the time-frequency dependent polarization filter for ground roll attenuation. All of these approaches are designed in either time or frequency domain, without considering phase information.

However, for the actual field data, the frequency spectrum, phase information and the polarization characteristics all change with time. Only implemented the polarization filtering in one or two domain, signals with other different attributes that arrived

simultaneously cannot be identified. Therefore, compensating for the phase and frequency distortions related to vector infidelity is essential for the accurate 3C processing.

3.3. Theory

3.3.1. Wave Polarization

Seismic waves can be distinguished by the directions of their oscillation. P wave's particle motion is perpendicular to the wave-propagation direction while the particle motion of S waves is parallel to the direction of wave propagation. Both of these two types of body waves form a straight line on the oscillation panel. For the surface waves, their particle motion is circular in the oscillation panel but is also parallel to the propagation direction. This oscillation property of waves is described as wave polarization. When body waves arrive with surface waves together, within a certain time window, the particle motion forms an ellipse on the oscillation panel, which is called the polarization ellipse (Figure III-1).

This polarization ellipse is constructed through eigen analysis where the major axis **Y'** of the ellipse is defined by the vector with the largest eigen value. The input data $\vec{V}$, the vector of the particle displacement, can be decomposed into $\overrightarrow{Vs}$ and $\overrightarrow{Vn}$, where $\overrightarrow{Vs}$ is linear polarized body waves and $\overrightarrow{Vn}$ is circular polarized surface waves (Figure III-2). This ellipse is the key to solving the polarization attributes, which reveals the range of amplitudes and phases of collected seismic data.

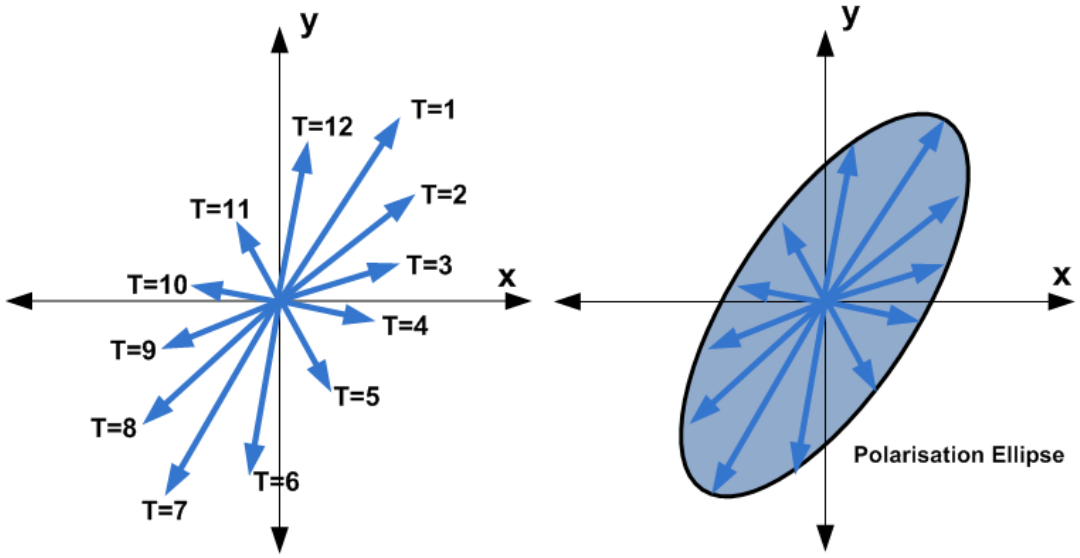

Figure III-1: Formulation of polarization ellipse (Pethick, 2015)

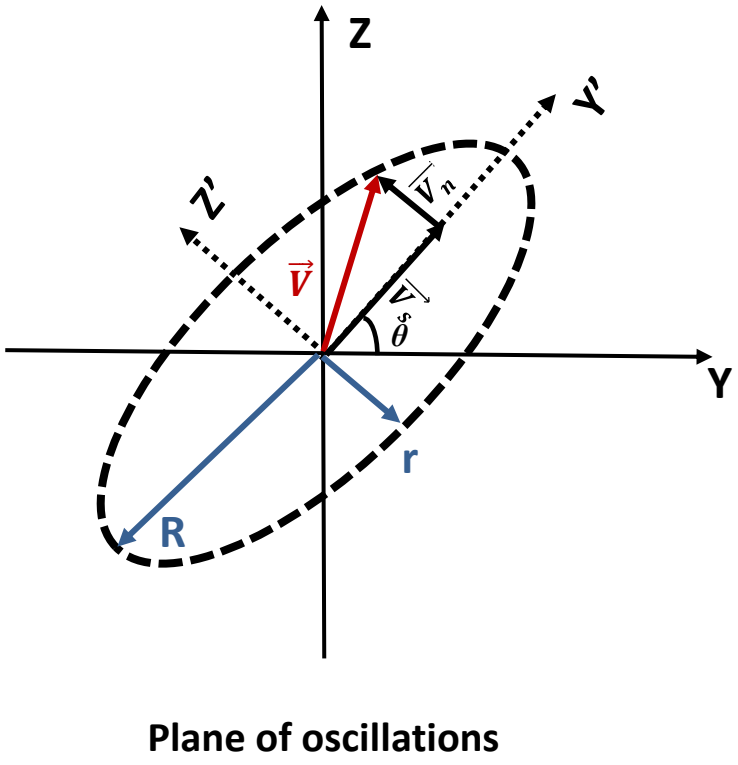

Figure III-2: Signal decomposition. Collected signal $\vec{V}$ can be divided into two vectors, $\overrightarrow{Vs}$ and$\overrightarrow{Vn}$, where $\overrightarrow{Vs}$ is mainly caused by signal and $\overrightarrow{Vn}$ is caused by noise.

Several polarization attributes are important to characterize the propagation features based on a pure elliptically polarized signal. R and r are the semimajor axis and the semiminor axis of the ellipse, respectively (Figure III-2). Large R/r ratio represents more linear polarized waves in the arrived signals, while a smaller value means more surface waves existed. The angle θ (Figure III-2) between major axis of the ellipse and the horizontal axis is called the rise angle, which distinguish the horizontal polarized wave (θ equals to 90 degree) from the vertical polarized wave (θ equals to 0 degree). Those polarized attributes are calculated through polarization analysis and implemented for the wave-mode separation.

Polarization analysis in the time domain is based on covariance analysis. It is in good condition when reflection signal and noise are in less coherence and the S/N is relatively high. However, in the shallow water environment, surface waves are high dispersive. In reality, reflected signals arrive with randomly mixed wave-fields containing various frequencies (wavelengths), spatial characteristics, phases and polarization states. Characterizing a recorded signal with these four parameters can be implemented to describe the propagation properties accurately.

Based on Fourier's theory, each trace component can be expressed as a superposition of sinusoids that have different frequencies. Figure III-3 shows the synthetic 3C data in the time at the bottom row (from the left to right: radial, transverse and vertical component) and its sinusoids decomposition at different frequencies in the top four rows. Simply analyzing the data in the time domain leads to large uncertainty.

The hodogram plots shown in the rightmost column of Figure III-3a using the three components in time domain cannot reveal the particle motion intuitively. Alternatively, we can first consider the signal one frequency at a time, instead of one component at a time. At any particular frequency, there are sinusoidal contributions to all three components, which, when combined, give elliptical motion in the 3D space (Figure III-3b). In the same way that the separate trace components are superposition of sinusoids, the particle motion can now be thought of as a superposition of ellipses.

Wavenumber ω is the spatial frequency of a wave, which is defined as the number of waves that exist over a specified distance. In a simplified wave equation:

$$y(x,t) = A\exp(i(kx - \omega t))$$

for particular receiver at a specific location x_0 , wavenumber turns to the phase related item, based on wave equation :

$$y(x_0,t) = A\exp(i(kx_0 - \omega t))$$

Therefore, the wavenumber effect on polarization is actually the phase effect on polarization. A linear polarization can be viewed as the combination of a horizontally linear polarized wave (R in the first column) and a vertically linear polarized wave (Z in the third column) in the same phase. If phase-shift is introduced in between the horizontal and vertical component, elliptical polarization is obtained. When the phase shift is exactly equal to 90 degree, the circular polarization is created. Decomposing the signal into different phases provides a better understanding of the wave polarization. Similar to frequency decomposition, any signal in time domain can be expressed as a superposition of sinusoids that have different phases (Figure III-4).

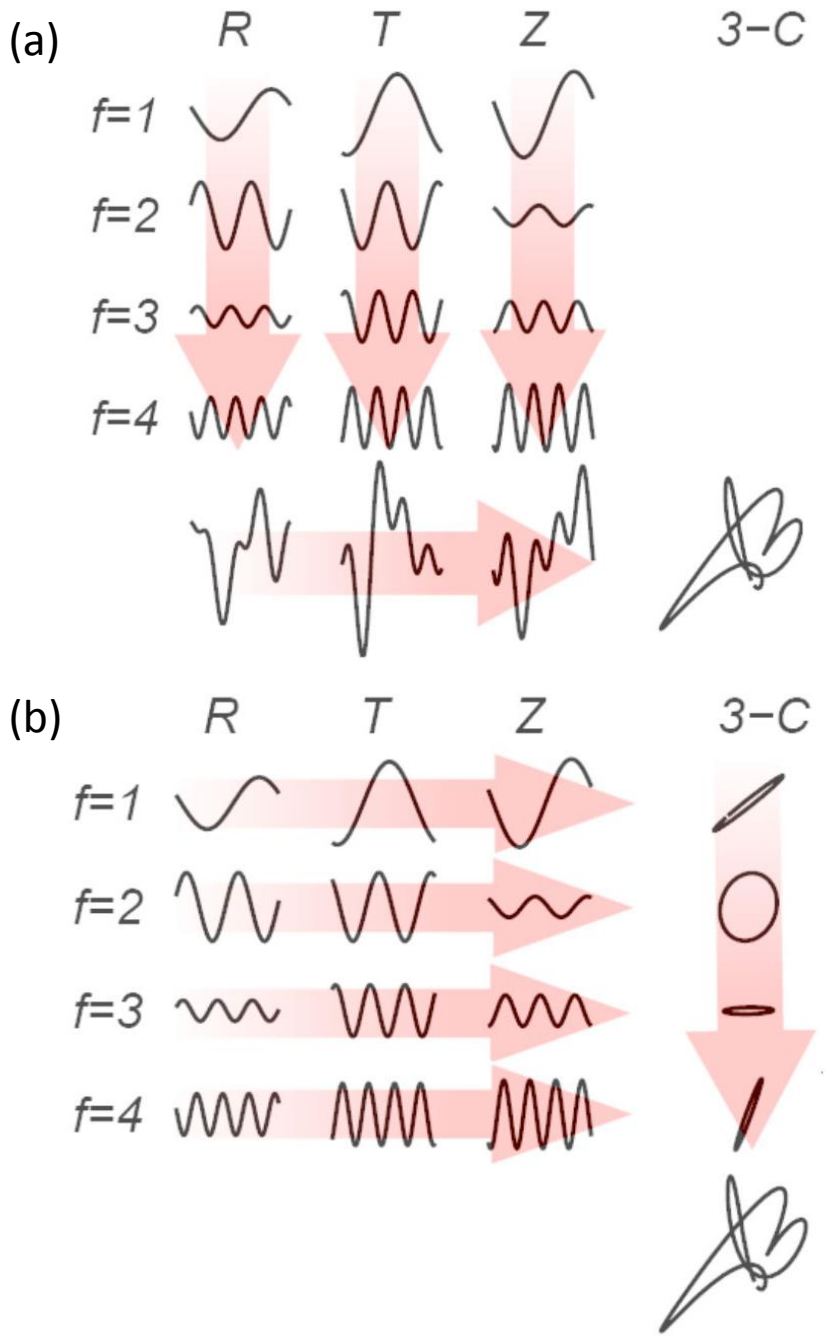

Figure III-3: (a) Fourier decomposition of a multicomponent synthetic trace. (b) Polarization ellipse at each frequency (Modified after Pinnegar, 2006).

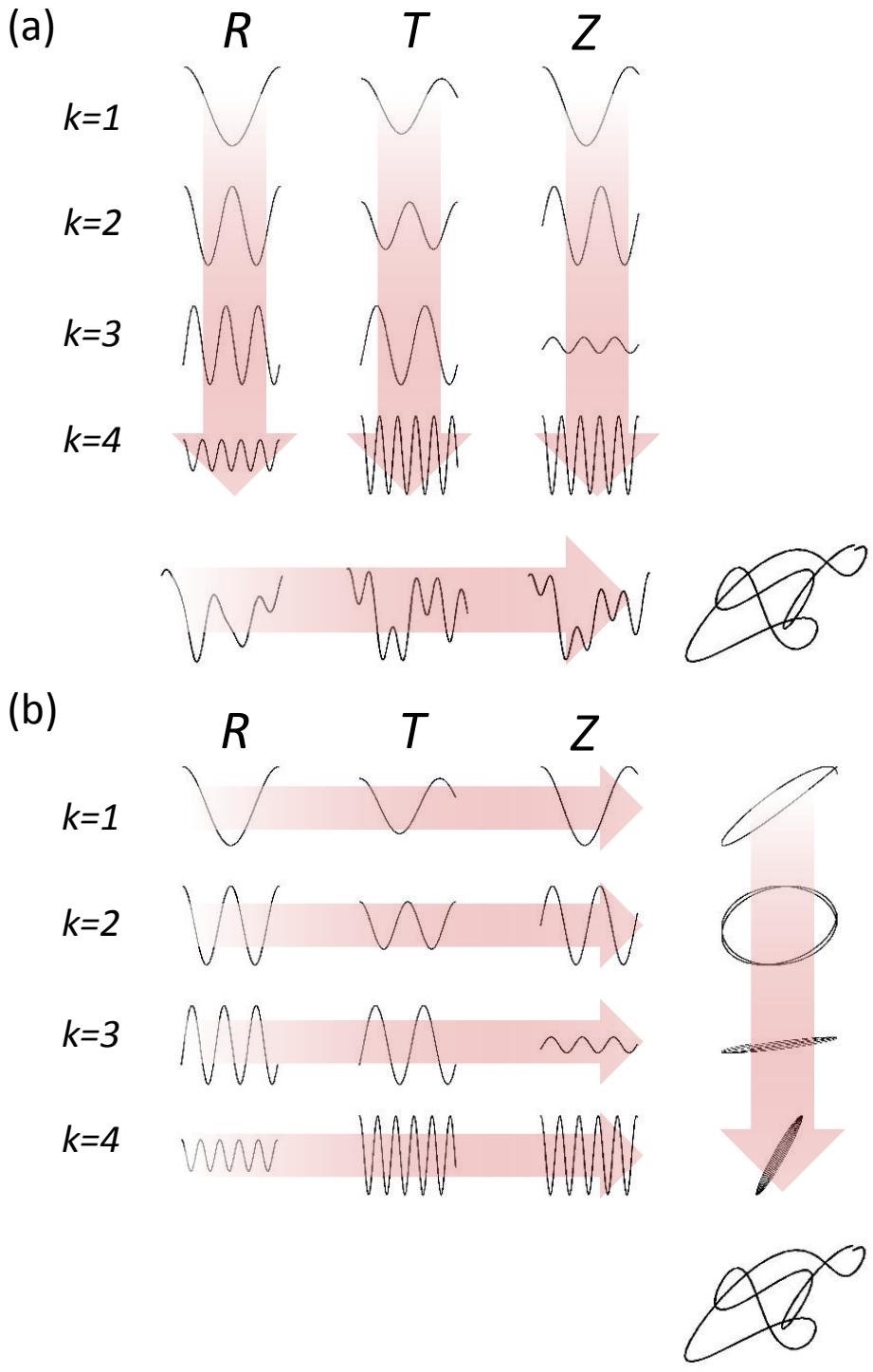

Figure III-4: (a) Fourier decomposition of a multicomponent synthetic trace. (b) Polarization analysis at different phases.

3.3.2. Covariance Analysis

Covariance analysis decomposes the information from the different geophones into the elements of the covariance matrix. The estimation of the covariance matrix reveals seismic wave-front parameters, specifically velocity and waveform. For a specific data window with L samples, the covariance matrix is the product of the data matrix with itself, which is given as:

$$C_x = \frac{1}{L}\sum_{i=1}^{L} x_i x_i^H$$

where $[\cdot]^H$ indicate complex conjugate transpose. For 3C data $(t) = (S_x(t), S_y(t), S_z(t))^T$, the covariance matrix is defined as:

$$C(t) = \begin{bmatrix} I_{xx}(t) & I_{xy}(t) & I_{xz}(t) \\ I_{yx}(t) & I_{yy}(t) & I_{yz}(t) \\ I_{zx}(t) & I_{zy}(t) & I_{zz}(t) \end{bmatrix}$$

where

$$I_{ij}(t) = \frac{1}{L}\int_{t-L/2}^{t+L/2} \big(S_i(\tau) - \mu_i(\tau)\big)\Big(S_j(\tau) - \mu_j(\tau)\Big)\, d\tau \ , \ i,j = (x,y,z).$$

$\mu_i(t)$ is the mean value of the $S_i(t)$ in the moving window.

The eigenstructure form derived from the covariance matrix is very useful to the understanding and the implementation of covariance applications, such as polarization analysis, velocity prediction and coherency estimation. It is defined as:

$$C_x = \sum_{i=1}^{M} \lambda_i v_i v_i^H = V \Lambda V^H$$

where V is the matrix of eigenvectors, $V = (v_1 v_2 ... v_M)$, λ_i is the corresponding eigenvalue ordered such that $\lambda_j > \lambda_k$ for j<k, and Λ is a diagonal matrix of eigenvalues. Purely

rectilinear ground motion has only one nonzero eigenvalue and purely elliptical polarization has two nonzero eigenvalues. For 3C seismic data, the polarization ellipsoid is constructed with eigenvector as the axis orientations, and eigenvalues as the corresponding energy components.

3.3.3. Polarization Analysis in Time Domain

The polarization characteristics of a seismic event change in time. Therefore, polarization analysis is usually done by eigenanalysis of the covariance matrix within a time window for a given time sample points. There eigenvectors ($\overrightarrow{V_1}(x_1, y_1, z_1)$, $\overrightarrow{V_2}(x_2, y_2, z_2)$, $\overrightarrow{V_3}(x_3, y_3, z_3)$) with three corresponding eigenvalues ($\lambda_1 > \lambda_2 > \lambda_3$) are obtained. If only one seismic arrival exists within the selected time window, the most complex signal that is possible is an elliptically polarized signal. The direction of polarization is defined by the V_1 with the largest egigenvalue λ_1. The horizontal azimuth angle Φ and the apparent incidence angle Θ are obtained based on the three components of V_1 (Jurkevics, 1998):

$$\Phi = \arctan(\frac{y_1}{x_1}),$$

$$\Theta = \arccos(|z_1|).$$

The degree of ellipticity is defined as the ratio between any two axes of the polarization ellipsoid:

$$\text{Principal ellipticity} \qquad e_{21} = \sqrt{\frac{\lambda_2}{\lambda_1}}$$

$$\text{Subprincipal ellipticity} \quad e_{31} = \sqrt{\frac{\lambda_3}{\lambda_1}}$$

$$\text{Transverse ellipticity} \qquad e_{32} = \sqrt{\frac{\lambda_3}{\lambda_2}}$$

where $e_{21} = e_{31} = 0$ is for purely linear polarization and $e_{31} = 0$ for purely elliptical polarization waves. The degree of rectilinearity is defined as:

$$RL(t) = \frac{\lambda_2 + \lambda_3}{2\lambda_1}$$

which is 1.0 for pure body waves and 0 for pure Rayleigh-wave motion.

Once the polarization attributes, rectilineartiy and incidence angle, are obtain by covariance analysis, the polarization filter can be constructed as the weight function $\tilde{R}$ times the directivity function $\widetilde{D}_i$. Within the time window L, the directivity functions are defined as:

$$\widetilde{D}_i(t) = \frac{1}{L} \sum_{r=-(L-1)/2}^{(L-1)/2} V_{1i}(t + r\Delta t)$$

where V_{1i} is the i-th component of the eigenvector with largest eigenvalue and Δt is the sampling rate, $i = (x, y, z)$.

The weight function is obtained on the basis of rectilinearity or ellipticity:

$$\tilde{R}(t) = \frac{1}{L} \sum_{r=-(L-1)/2}^{(L-1)/2} RL(t + r\Delta t)$$

and we use rectilinearity in our case.

For 3C data $S(t) = (S_x(t), S_y(t), S_z(t))^T$, the filtered data can be calculated by multiplying the weight function and the directivity function with the original data:

$$S_x{}'(t) = S_x(t)\tilde{R}(t)\widetilde{D}_x(t),$$

$$S_y'(t) = S_y(t)\tilde{R}(t)\tilde{D}_y(t),$$

$$S_z'(t) = S_z(t)\tilde{R}(t)\tilde{D}_z(t).$$

3.3.4. Polarization Analysis in Frequency Domain

A rectilinear arrival is easily detected in the time domain by the covariance analysis since each sample in the time window is close to summing along the wave arrival direction (Rutty and Greenhalgh, 1999). However, if the non-rectilinearly polarized event is dominated, the single energy is located in a plane. The covariance matrix analysis in the time domain fails to identify this as a linear event and spectral coherency matrix in frequency domain shows its advantage.

The spectral matrix is defined as

$$Sp(f) = \begin{pmatrix} S_{xx}(f) & S_{xy}(f) & S_{xz}(f) \\ S_{yx}(f) & S_{yy}(f) & S_{yz}(f) \\ S_{zx}(f) & S_{zy}(f) & S_{zz}(f) \end{pmatrix}$$

Where the diagonal terms are power spectra and the off-diagonal terms are cross-spectra among three components. The orthogonal eigenvectors and three eigenvalues can be obtained by

$$Sp(f)u(f) = \lambda(f)u(f) \text{ and } |Sp(f) - \lambda(f)E| = 0 .$$

The direction of wave polarization is defined the largest fraction of wave energy and can be obtained as the first eigenvector $\boldsymbol{u_1}(f)$.

3.4. Method

In principle, the linear polarization of waves can be used to determine the direction of the geophones, and in this way non-rectilinearly polarized waves (surface waves) can be distinguished from rectilinearly polarized waves (body waves). However, in reality, wave polarization is related to time, frequency, and wavenumber (Donno et al., 2008). It is inaccurate to recover the polarization attributes of wave types in one single domain, particularly when residual surface waves exist. The following proposed TFK polarization analysis method (Zhang et al., 2013) combines with the traditional polarization analysis technique for time and frequency dependent polarization analyses in the decomposed TFK domain to measure the wave motion.

In the TFK domain, three-component seismic data can be presented in a general form:

$$X(t, f, k) = (x^1(t, f, k), x^2(t, f, k), x^3(t, f, k))$$

where x^1 , x^2 and x^3 represent the vertical, radial and transverse components, respectively. Considering a time interval containing N samples with sampling rate Δt in time, for each TFK point, auto and cross-variances can be defined as:

$$C(t, f, k) = \frac{\sum_{i=1}^{N} X(t + i\Delta t, f, k) X^{*T}(t + i\Delta t, f, k)}{\sum_{i=1}^{N} \left| X(t + i\Delta t, f, k) \right|^2}$$

where * denotes conjugate, and T transpose. Three complex eigenvalues and three eigenvectors are obtained by solving the characteristic equation of C. The eigenvector

$V_1(t, f, k)$ with the largest eigenvalue points to the main polarization direction, defining a polarization ellipsoid. It also provides the degree of polarization which is related to the order and orientation of the three components. In our case, we use the rectilinearity modified from Jurkevics (1988) as the polarization degree:

$$RL(t, f, k) = 1 - \left(\frac{\lambda_2(t, f, k) + \lambda_3(t, f, k)}{2\lambda_1(t, f, k)}\right)$$

Polarization attributes, reciprocal ellipticity ρ and the rise angle θ, are calculated for each ellipsoid (Jurkevics, 1988; Zhang et al., 2013; Diallo et al., 2006):

$$\rho(t, f, k) = \frac{\lambda_2(t, f, k) + \lambda_3(t, f, k)}{2\lambda_1(t, f, k)},$$

$$\theta(t, f, k) = \arccos \frac{V_{3x}(t, f, k)}{|V_3(t, f, k)|}$$

where V_{3x} is the x component of the eigenvector V_3. Linearly polarized events (body waves with low ρ) and nonlinearly polarized events (surface waves with high ρ) can be distinguished through the reciprocal ellipticity. Rise angles provide the information to identify the vertically polarized events (P waves and Rayleigh waves) from the horizontal polarized events (S waves).

Considering the pattern of particle motion and surface wave propagation directions, we can design the polarization filtering to eliminate the residual surface waves which overlap with body waves in the TFK domain. The smoothing operators are used as a point-by-point gain control to modulate the rotated records (Zheng and Stewart, 1992; Nguyen et al., 1989), so the filtered seismograms $\tilde{X}(t, f, k)$ are given by:

$$\tilde{X}(t, f, k) = X(t, f, k)\tilde{R}(t, f, k)\tilde{D}(t, f, k)$$

where N is the length of the moving window in time domain and the weight functions are calculate through:

$$\tilde{R}(t, f, k) = \frac{1}{N}\sum_{i=1}^{N} RL(t + i\Delta t, f, k)^{L}, \tilde{D}(t, f, k) = \frac{1}{N}\sum_{i=1}^{N} V_1(t + i\Delta t, f, k)^{J}$$

Therefore, combining the previous result in Chapter II, the proposed two-step workflow is describe in Figure III-5. It has following steps:

(1) Apply the TFK transform on the original data and get the 3D result TFK(t,f,k) in the TFK domain. The input raw data first goes though 1D Fourier transform over the spatial variable, and then the variable S transform over time.

(2) Design the FK filtering at each specific time in the TFK domain based on the frequency and wavenumber properties to eliminate surface waves.

(3) Design suitable filters R(t,f,k) and D(t,f,k) in the TFK domain on the basis of polarization attributes to separate out residual surface waves.

(4) The filtering is imposed on the resulting spectrum within which the undesired energy is zeroed out.

(5) Invert the filtered record through an inverse ST and an inverse FT to put the data back into the time domain.

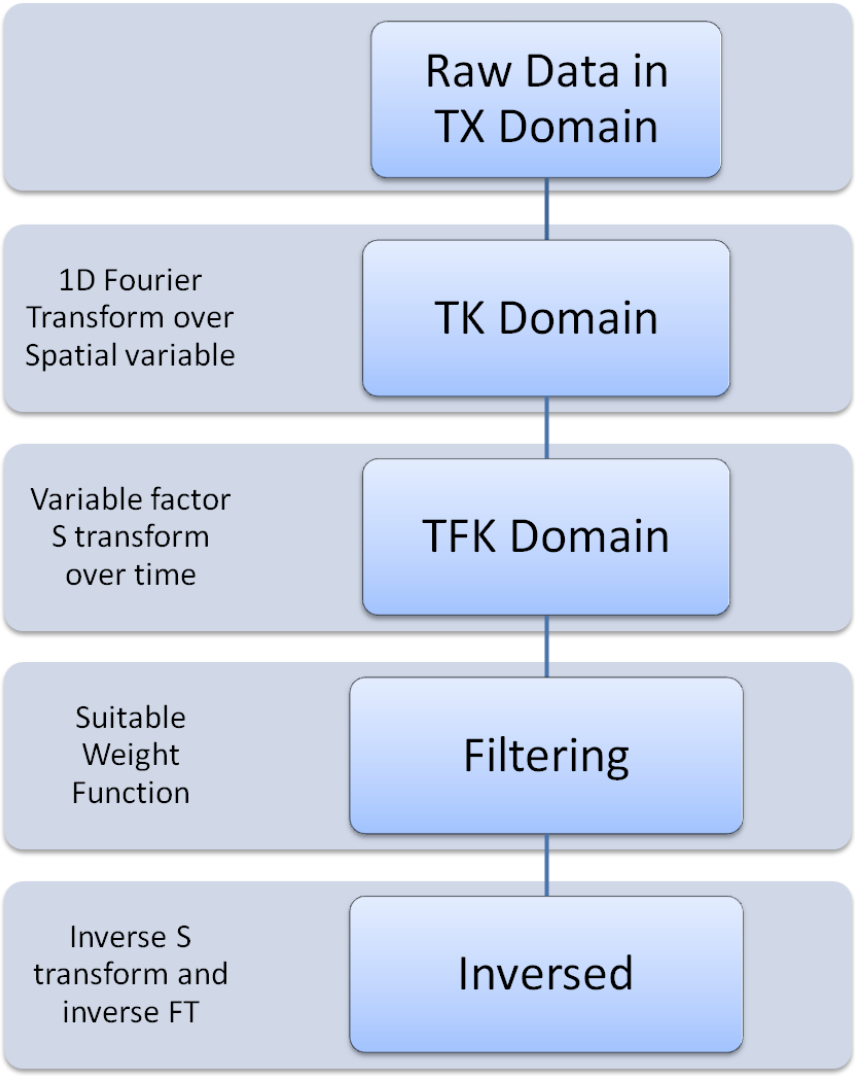

Figure III-5: Workflow of the two-step TFK polarization analysis

3.5. Results

A 2D 4C OBC data set used for this study was acquired in the Arabian Gulf where the locale has a very shallow water depth. The receiver interval is 25m and the time sampling interval is 2ms. Surface waves in this data set include the trapped waves in the water column and the interface waves generated in the hard sea-bottom, all of which influence the data quality and interpretation of the 4C data (Figure II-3). The coupling of the inline geophone is normally better than the cross-line geophone component; the noises recorded in the cross-line geophone can pollute the vertical component due to the energy leakage. Therefore, the vertical component appears to have a lower S/N than the inline component in our record shown in Figure II-3, which indicates the poor ground coupling issue existed in this acquisition.

The wave dispersion shows clearly in the FK domain in Chapter II (Figure II-5). The TFK filtering demonstrates efficient attenuation of surface waves in this shallow water environment (Zhang et al., 2012, 2014). However, the spatial aliasing from strong Scholte waves (Label A in Figure II-4) and P-related surface waves (Label B in Figure II-4) still contaminate the signal band of reflected waves (Label D in Figure II-4) in the TFK domain, which leads to residual surface waves for polarization analysis. Surface wave polarity is unstable, as even a small amount of noise contribution can lead to large changes in the dip and induce anomalous polarization (Pinnegar, 2006). Figure III-6 illustrates these problems using the transverse component after TFK filtering and the time-dependent polarization analysis. Residual Scholte waves and noise overprint on the reflected signals. Low values in rectilinearity (Figure III-6b) indicate elliptical

polarization (blue color, close to 0) that damages the linear polarization (red color, close to 1) of body waves. This result demonstrates that directly analyzing the polarization in a single domain, either time or frequency, will bring artifacts to the rotated result.

We further analyze polarization attributes in the TFK domain combining information of time, frequency and velocity. Figure III-7 shows the reciprocal ellipticity and the rise angle in the TF domain for a certain wavenumber. Low values in reciprocal ellipticity (blue color in Figure III-7a) indicate linear polarization of body waves in the frequency zone from 20 Hz to 40 Hz, which correlates consistently with the reflected signal in the FK domain. The random red dots, indicating high ellipticity values, are possibly related to the interference from P-related surface waves, which is consistent with the analysis from the FK domian. A large rise angle (denoted by red color in Figure III-7b) indicates vertically polarized events, where the main polarization direction is perpendicular to the horizontal axis, while the blue color in Figure III-7b corresponds to horizontally polarized events. A comprehensive interpretation based on these two attributes provides the way to separate the vertically polarized reflections (P waves, blue color in Figure III-8a and red color in Figure III-7b) from those with horizontal polarization (S waves, blue color in Figure III-7) (Diallo et al., 2006).

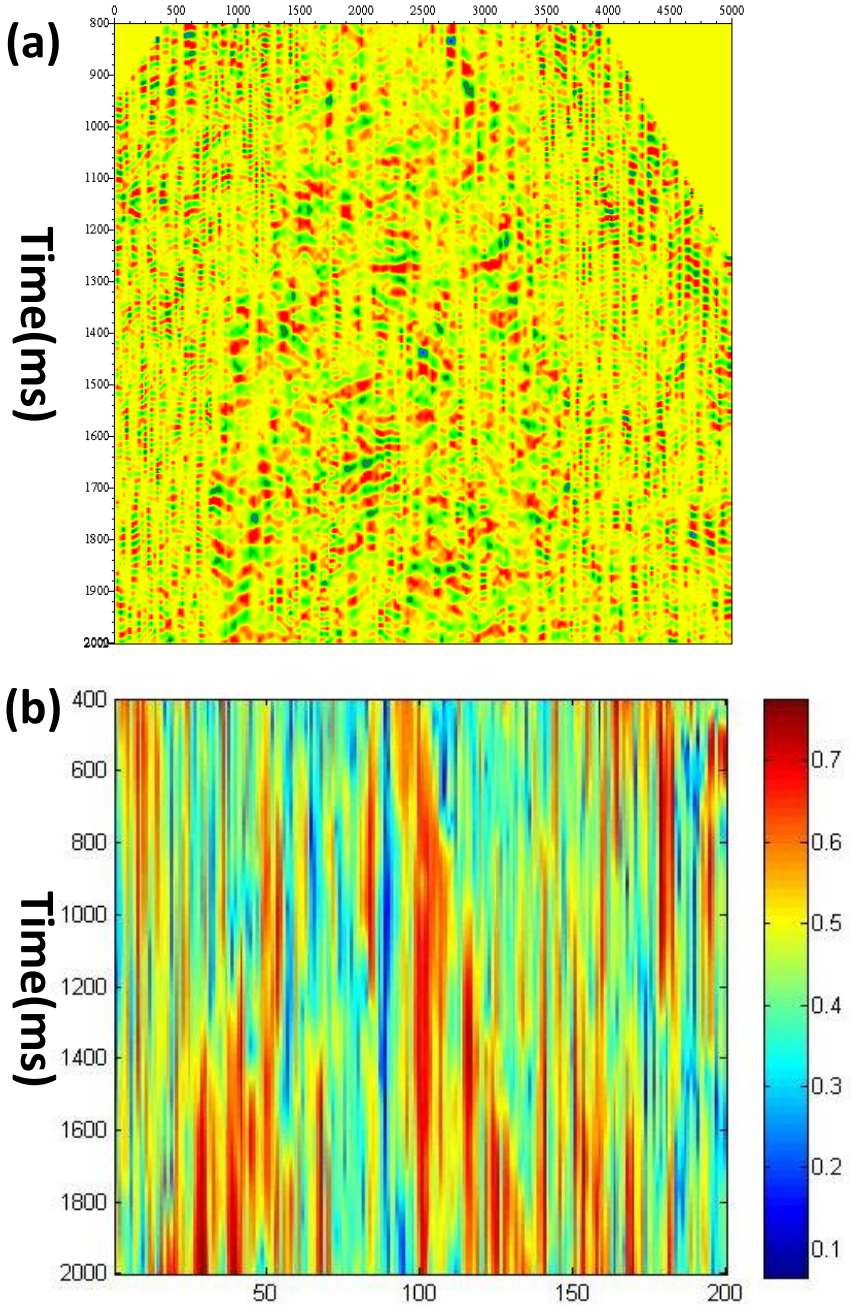

Figure III-6: (a) Transverse component after the time-dependent polarization (b) Degree of polarization. High value indicates perfect linear polarization (body waves) and low values for elliptical polarization.

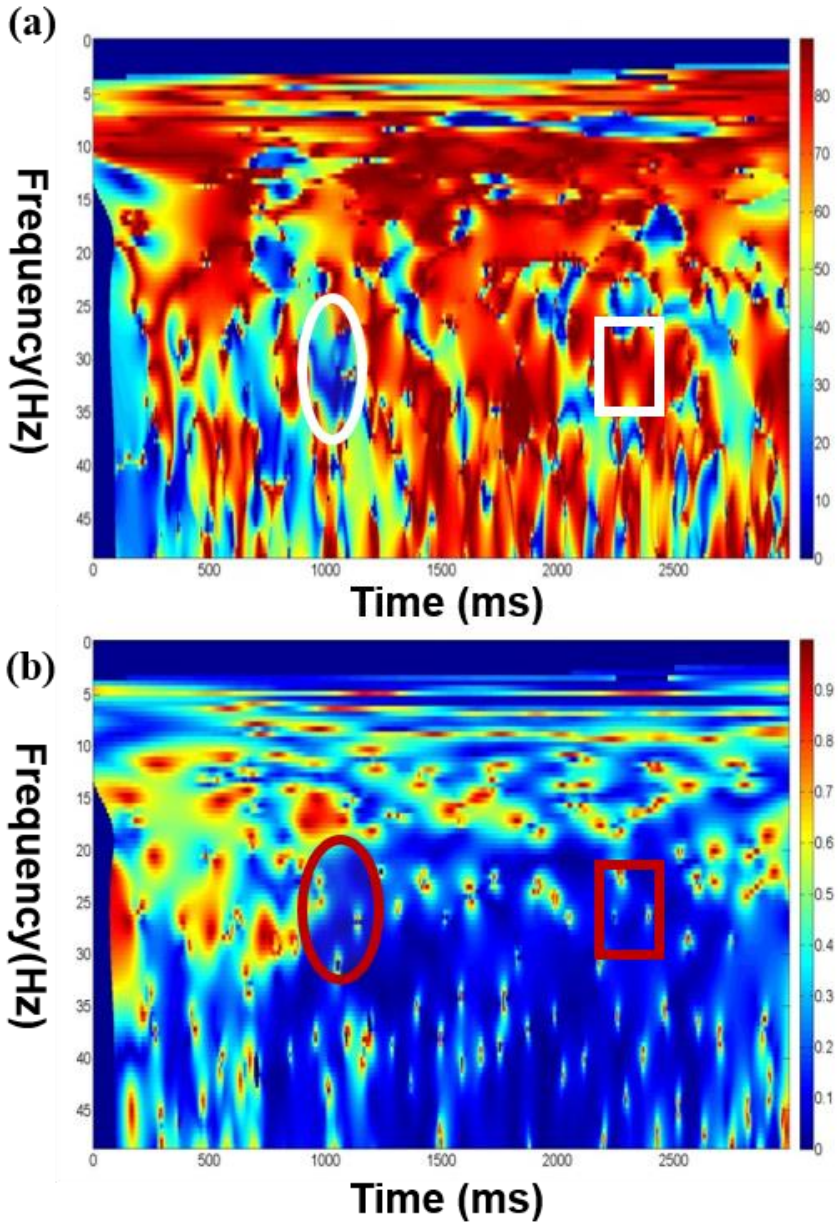

Figure III-7: (a) Computed reciprocal ellipticity. (b) Computed rise angle.

From the polarization attributes interpretation, two distinctive zones are selected. Strong P waves (red circle in Figure III-7a and white circle in Figure III-7b) occurs around t = 1400ms and strong S waves (red rectangle in Figure III-7a and white rectangle in Figure III-7b) are seen around t = 2400ms. To confirm these results, the hodogram analysis (Figure III-8) is used for a visual analysis over these two time windows. In Figure III-8a, the major motion is linear in the vertical-radial plane, and the displacement in the vertical direction is larger than that in the horizontal, as is expected for P waves. The particle motion of S waves is more complicated; the hodogram (Figure III-8b) shows that the amplitude of the radial component is larger than that in the vertical. Thus we can conclude that converted S waves exist in this time window. Well log data shows the top of the reservoir is located around 1300ms on two-way travel time. The strong P waves identified here can be related to the primary reflection from the reservior top and S waves are the PSS converted waves. This prediciton is also consistent with the modeling and processing results (Berteussen et al., 2014) in this field.

Figure III-9, Figure III-10 and Figure III-11 show the results of TFK polarization analysis after time-varying filtering. By the comparison of the transverse component in Figure III-11 with that of only time-dependent polarization analysis in Figure III-6a, the processed record in Figure III-11 shows that the S/N of the data is much improved and the reflected layers become much easier to interpret after TFK polarization analysis. The strong signal in the transverse component could be the PSS converted waves. This improvement on the rotation of OBC data could be very beneficial for subsequent processing, interpretation and shear wave estimation.

3.6. Conclusion

Rotation of three geophone components is one of the key procedures in the processing of 4C OBC seismic data, particularly when the geophone orientation is unknown or incorrect. Traditional polarization analysis can only be accurate if the S/N is high and surface waves are not highly dispersive. In this paper, we have demonstrated the adverse effects of Scholte waves on 3C rotation, and proposed a TFK polarization analysis method and a two-step work flow: TFK filtering followed by the proposed TFK polarization analysis. The method provides more reliable information about orientation and improves data quality which is important for the further processing of the converted waves in horizontal components.

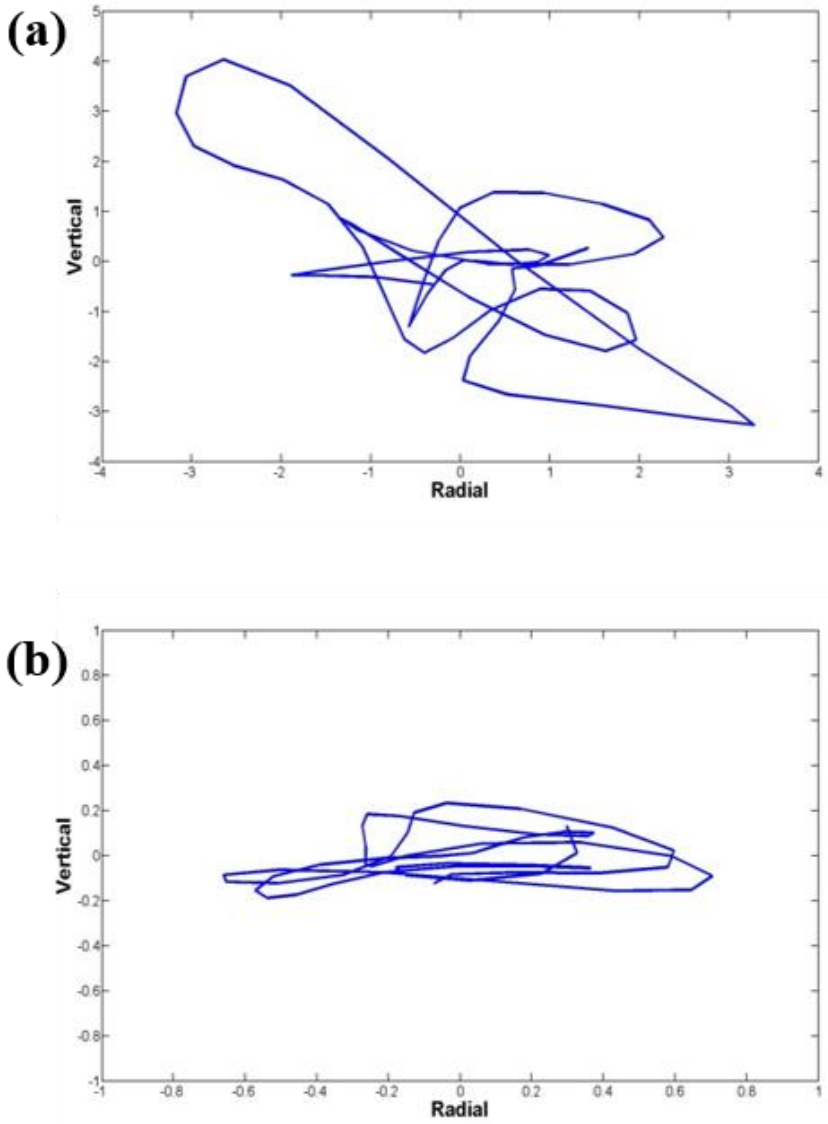

Figure III-8: (a) Hodogram showing the particle motion over the time window t=[1350, 1500] ms. (b) Hodogram showing the particle motion over the time window t = [2260, 2380] ms.

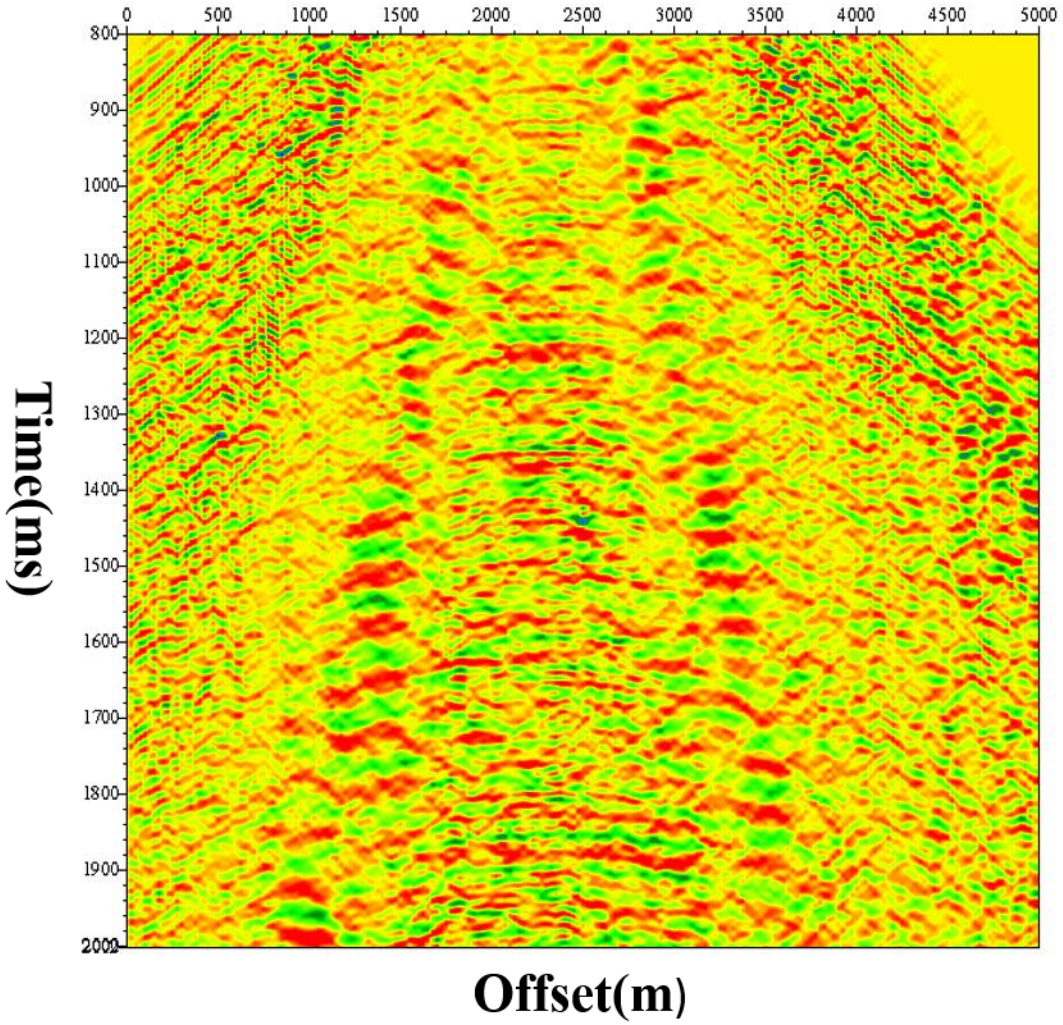

Figure III-9: Vertical component after TFK polarization analysis.

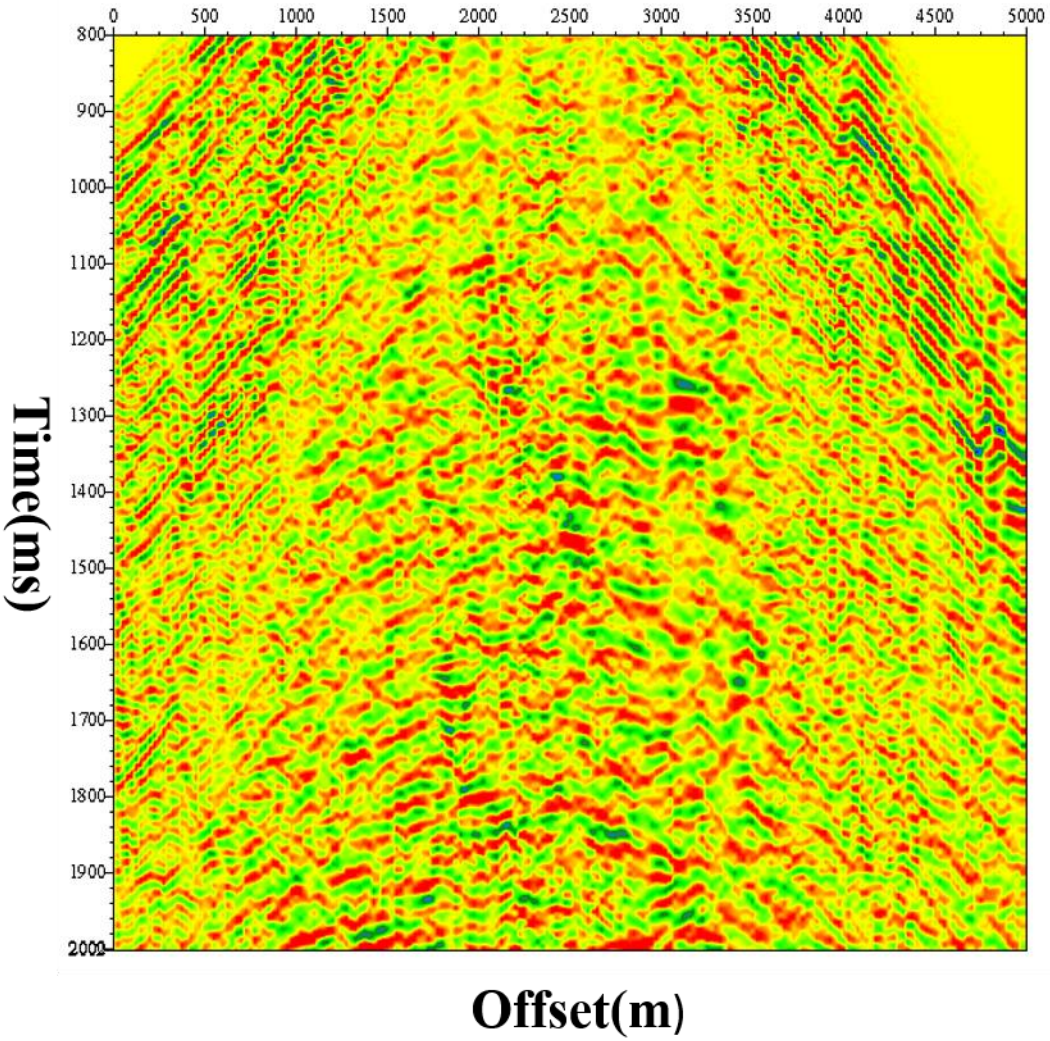

Figure III-10: Radial component after TFK polarization analysis.

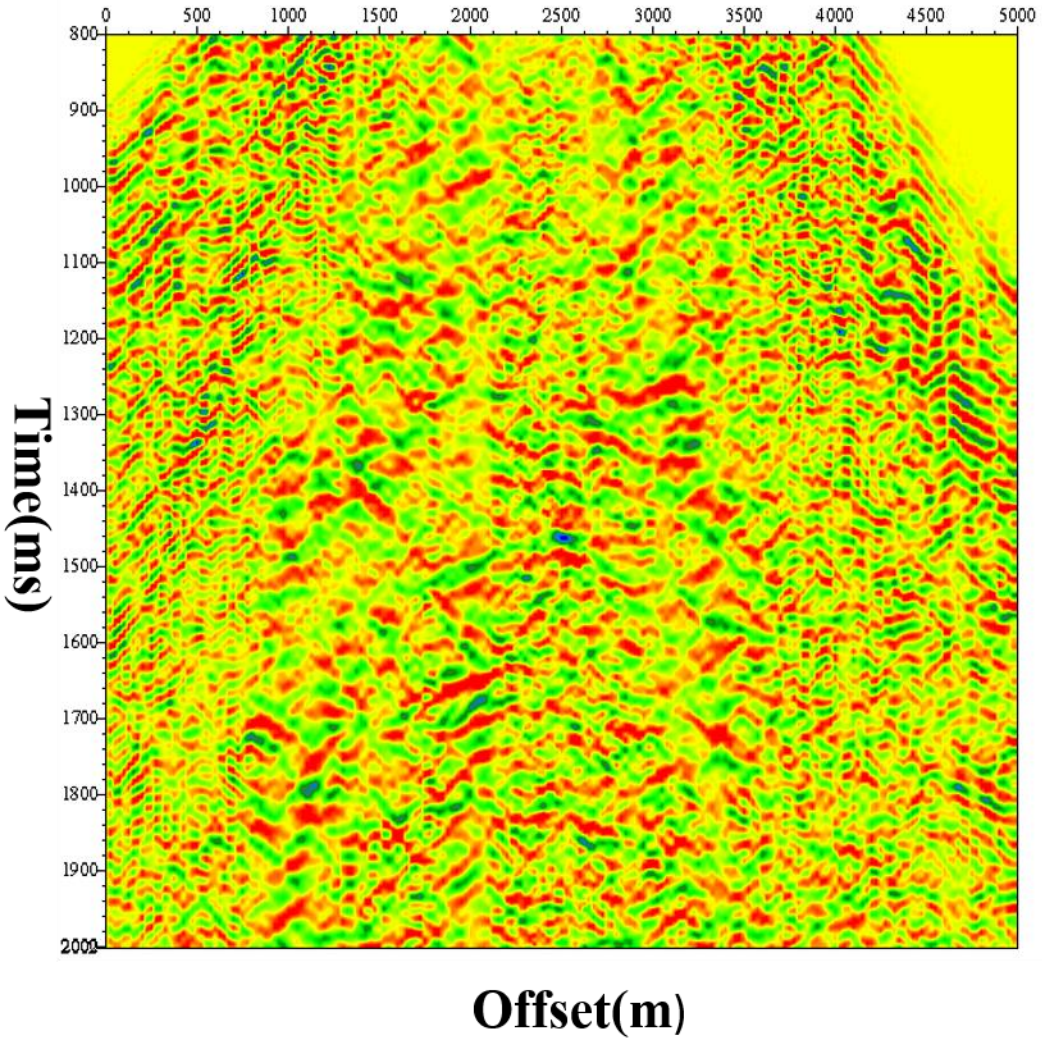

Figure III-11: Transverse component after TFK polarization analysis.

CHAPTER IV

SEISMIC DATA PROCESSING

4.1. Summary

The primary objective of the seismic processing is to obtain images of subsurface structures and other geological information from the acquired raw data for structural interpretation, stratigraphical and depositional analysis and reservoir property estimation. Most processing techniques used today for marine data processing have been developed for deep-water environment. However, because of the shallow nature of the water in offshore Abu Dhabi fields, and because of congestion from oil field hardware there, poor acquisition system leads to low quality seismic datasets. On the other hand, the development of OBC seismic in the shallow environment leads to the great potential in converted shear-wave data acquisition. The P wave data may fail to image subsurface structures when salt dome or gas chimneys exist, while shear wave data have the advantages in those situations (Berg et al., 1995). Due to the difference in acquisition schemes between the tow-streamer and the ocean bottom cable, exiting processing sequence cannot be simply implemented onto the 4C dataset. Therefore, a new 4C seismic processing sequence is needed for seismic data quality improvement, better shear wave detection and subsurface structure imaging.

No single "correct" processing sequence exists for a given volume of data. In this chapter, we will discuss the processing sequence based on one 2D 4C seismic test line from the offshore UAE. The acquired data from all four components (one hydrophone

and three geophones) will be applied; the hydrophone and vertical component aim for P waves, and two horizontal components aim for shear waves. The objective is to 1) image the substructure through both P and S waves and 2) preliminarily verify the existence of direct shear waves, which has been demonstrated by the modeling results.

4.2. Literature Review

The general processing flow of the seismic data involves noise attenuation, velocity analysis, NMO correction and stacking, in order to get the final structural section. Processing the 4C data collected in the shallow water environment is based on this general processing flow, however, we need improve the noise attenuation model and alter the velocity analysis.

Shallow OBC acquisition results in high amplitude, scattered noises. One common operational approach to reduce noises is to calibrate the vertical geophone (Z) and sum it to the hydrophone (P), where these two detectors share the same polarity for the upcoming wave-field and opposite polarity for the down-going wave-field (Loewenthal et al., 1985; Barr and Sanders, 1989; Dragoset and Barr, 1994; Rosales and Guitton, 2004; Ishiyama et al., 2008; Basu et al., 2012). By eliminating noises, structural information can be extracted from the seismic data. There are several known method for performing this PZ summation. Ball and Corrigan (1996) first proposed the generalized dual-sensor model to estimate the coupling differences for processing the data contaminated with cross-ghost. Schalkwijk et al. (1999) introduced the elastic

decomposition equation into the design of the frequency-dependent calibration filter for deep ocean-bottom field dataset. Gaiser et al. (2002) further studied the vertical coupling effects on amplitude and phases by a least-squares operator in the frequency domain.

The common principle of the above methods is that they implement the equation of wave propagation to reduce the down-going waves in the selected time frame that only contains the primary reflections. Both peg-leg multiples and receiver ghost can be separated out theoretically. The well picked window and calibration parameters, achieved when noise-to-signal ratio is low, are necessary. However, in the shallow water environment, OBC data contains various types of noise ranging from random spikes or bursts to coherent ground roll waves, which bring difficulties in achieving the full benefits of the PZ summation.

The velocity analysis and binning methods are different in the common-conversion-point (CCP) domain and the common-middle-point (CMP) domain, where the sorting is decided by the wave-mode of the input data. Wave-mode conversion occurs when the incident wave passes the boundary between two different layers of rock. For a natural 3D source-displacement, a three-vector receiver should theoretically record nine possible wave-modes, converted from P, SH and SV. The 3D nine-component (9C) surveys with both S and P-wave sources are designed to provide all nine wave modes, including both direct and converted shear wave modes. However, this technique is limited to onshore environment for VSP acquisition for now (Rusmanugroho and McMechan, 2012; Cultreri et al., 2005; Blouin et al., 2013), and it costs more to acquire

and process 9C data to get the S-wave (SV-SV and SH-SH) information. Current marine 4C technology is restricted to obtain the converted wave-modes (P-SV) from the downgoing P waves for structural imaging and interpretation (Johns, et al., 2006; Johns, 2007; Crompton, et al., 2005; Fjellanger, et al., 2006), fracture detection (Vetri, et al., 2003) and porosity trends identification (Martins and Davis, 2014). The velocity analysis of these converted waves is based on CCP principles, which consider the velocity difference between the down-going wave-field (P wave) and the up-going wave-field (SV-wave) (Rajput, 2010). Comparing to CMP, CCP has a higher requirement on azimuthal binning and needs an accurate pre-estimate on V_p/V_s ratio. Another issue in the above applications is all of these well-used methods only use two (hydrophone and vertical components) of the four components.

Few successful application have been implemented using the horizontal components in the shallow marine acquisition. Tatham and Goolsbee (1984) first demonstrated the existence of the seafloor-converted P-SV mode and proposed the techniques to obtain the SV-SV image from the towed-cable hydrophone data in the hard sea environment. Modelling results (Sun et al., 2009 and Berteussen and Sun, 2010) indicates the strong P-S conversion occurs at the sea bottom in the shallow water Arabic Gulf, where the conversion is more than a thousand times stronger than other deep-water environments (>100 meters depth) in the rest of the world. This presents a unique opportunity to estimate shear wave information from the OBC data acquired in this region.

To tackle these obstacles in 4C processing (noise attenuation and velocity analysis), a properly designed processing workflow is desirable for the estimation of P wave profiles through an accurate PZ summation, and it is also necessary for the extra shear wave's extraction from horizontal components.

4.3. Theory

4.3.1. Conversion at Water Bottom

In the shallow water environment, an incident P-wave can be converted to an S wave at the water bottom. Inadequate knowledge of the shallow-water characteristics of seismic wave propagation resulted in the ignorance or inappropriate consideration of shear wave detection. Tatham and Goolsbee (1984) indicates that P-to-SV mode conversion at the hard sea bottom can be considered as a secondary SV source in the far offset. This research motivates the project that explores the PS-S reflections in the OBS acquisition, where the direct shear waves are generated by the shear source at the seafloor and travels through the subsurface (Figure IV-1).

For a down-going incident P-wave in the water column, the energy decomposes into three possible wave fields: (1) a reflected P wave in the water layer; (2) a transmitted P wav in the solid layer; and (3) a converted SV wave transmitted in the solid layer. In this fluid-sold model, the P-P reflection coefficient, P-P transmission coefficient and P-SV converted transmission coefficient are defined as:

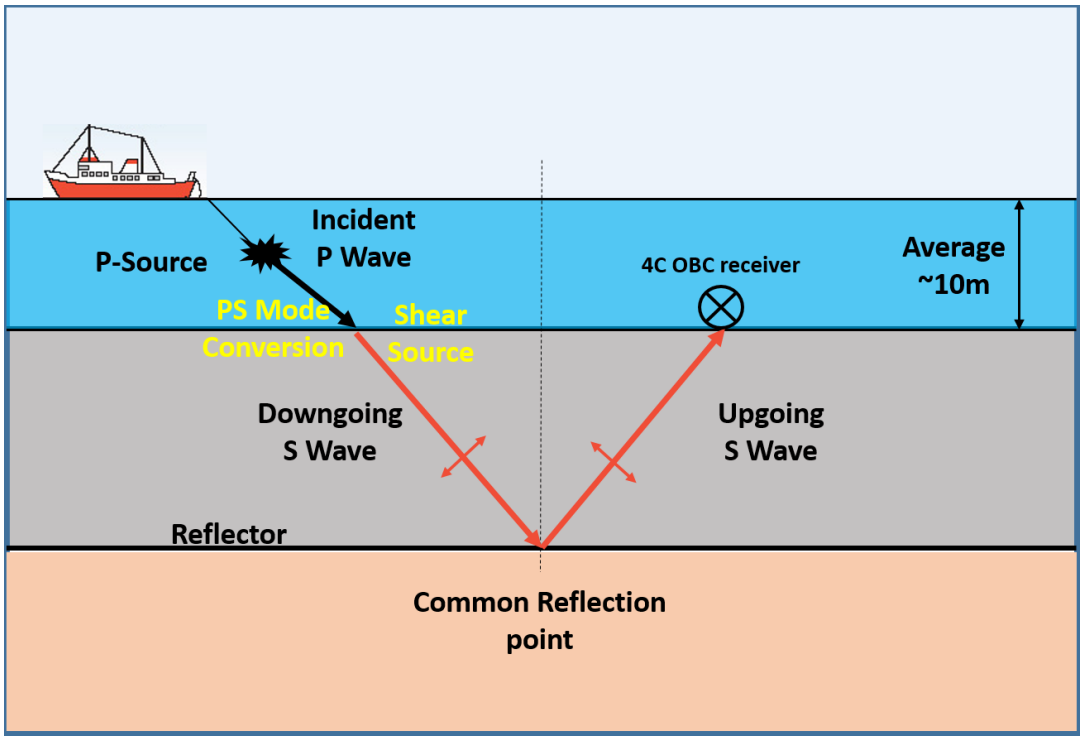

Figure IV-1: Illustrating PSS mode conversion at the sea bottom.

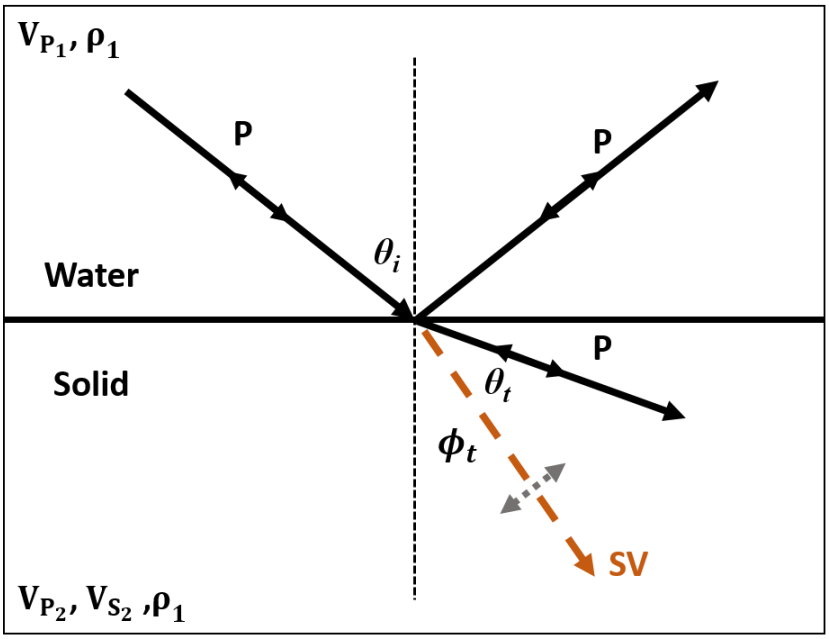

Figure IV-2: Sketch of the energy partitioning at a water-bottom interface.

$$R_{pp} = \frac{A_1\rho_2 V_{P_2}\cos\theta_i + A_2\cos\theta_i\cos\theta_t - \rho_1 V_{P_1}\cos\theta_t}{A_1\rho_2 V_{P_2}\cos\theta_i + A_2\cos\theta_i\cos\theta_t + \rho_1 V_{P_1}\cos\theta_t}$$

$$T_{pp} = (\frac{V_{P_1}}{V_{P_2}}) \times \frac{2B\rho_1 V_{P_2}\cos\theta_i}{A_1\rho_2 V_{P_2}\cos\theta_i + A_2\cos\theta_i\cos\theta_t + \rho_1 V_{P_1}\cos\theta_t}$$

$$T_{ps} = (\frac{V_{P_1}}{V_{S_2}}) \times \frac{2C\cos\theta_i\cos\theta_t}{A_1\rho_2 V_{P_2}\cos\theta_i + A_2\cos\theta_i\cos\theta_t + \rho_1 V_{P_1}\cos\theta_t}$$

with

$$A_1 = cos^2(2\phi_t) = B^2,$$

$$A_2 = 4\rho_2 V_{S_2} sin^2\phi_t \cos\phi_t,$$

$$B = \cos 2\phi_t \ ,$$

$$C = 2\rho_1 V_{S_2} \sin\phi_t \ .$$

where V_{P_1} and V_{P_2} are the P velocity in water and at the sea bottom, respectively; V_{S_2} denotes the S velocity. The corresponding angles are displayed in Figure IV-2. Figure IV-3 shows the variation of T_{PS}, T_{pp} and R_{pp} with the incident angle in a shallow marine model with the parameters: $V_{P_1} = 1500\frac{m}{s}$, $\rho_1 = 1000\frac{Kg}{m^3}$, $V_{P_2} = 3200\frac{m}{s}$, $V_{S_2} = 1400\frac{m}{s}$ and, $\rho_2 = 2500\frac{Kg}{m^3}$. The values are normalized by the energy of incident P-wave for comparison.

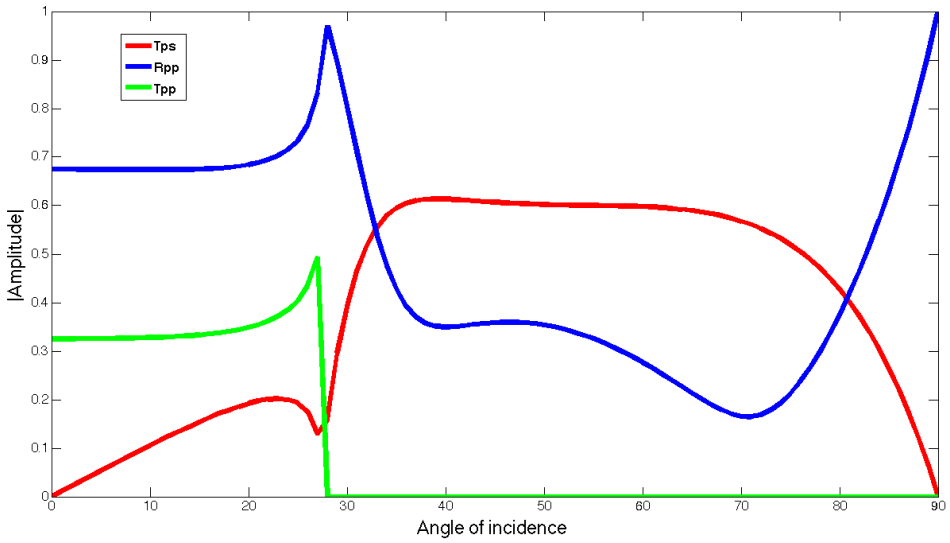

Figure IV-3: Reflection and transmission coefficients for fluid-solid interface for the model parameters: $V_{P_1} = 1500m/s$, $\rho_1 = 1000kg/m^3$, $V_{P_2} = 3200m/s$, $V_{S_2} = 1400m/s$ and, $\rho_2 = 2500kg/m^3$.

In this model, the PS conversion reaches maximal at an angle between 25 and 30 degrees and then decreases till reaching the critical angle but increases again at larger angles (Figure IV-3). The amplitude of PS (red line in Figure IV-3) converted wave is much higher than PP (blue line in Figure IV-3) transmission wave when the incident angle exceeds the critical angle, which means we expected to see strong PSS waves in the collected dataset. In order to verify the location of the maximal conversion, we continue to analyze the relation between the amplitude of converted wave and predefined parameters in modified models. Figure IV-5, Figure IV-6 and Figure IV-6 demonstrates the energy partition of T_{PS} as a function of the incident angle with varying V_{P_2}, V_{S_2} and ρ_2. Deceasing in P wave velocity of the solid leads to increasing of

the critical angle but decreasing the maximum conversion at the post-critical angle in Figure IV-5. Changes in shear velocity and density do not affect the location of the maximum conversion but the amplitude of the PS conversion (Figure IV-4 and Figure IV-6). In the shallow water environment of the Arabian Gulf, the typical P velocity varies from 3000 $\frac{m}{s}$ to 4800 $\frac{m}{s}$ and S waves from 1400$\frac{m}{s}$ to 2200 $\frac{m}{s}$based on the log data (Sun and Berteussen, 2009a). These values verified this model result is suitable for the case in our research areas.

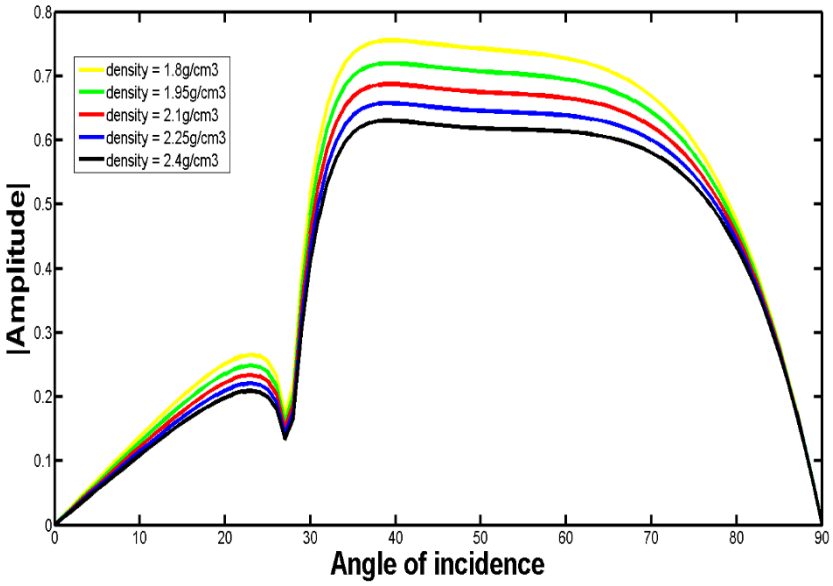

Figure IV-4: Transmission coefficient T_{PS} as a function of incident angle with varying density of hard sea bottom.

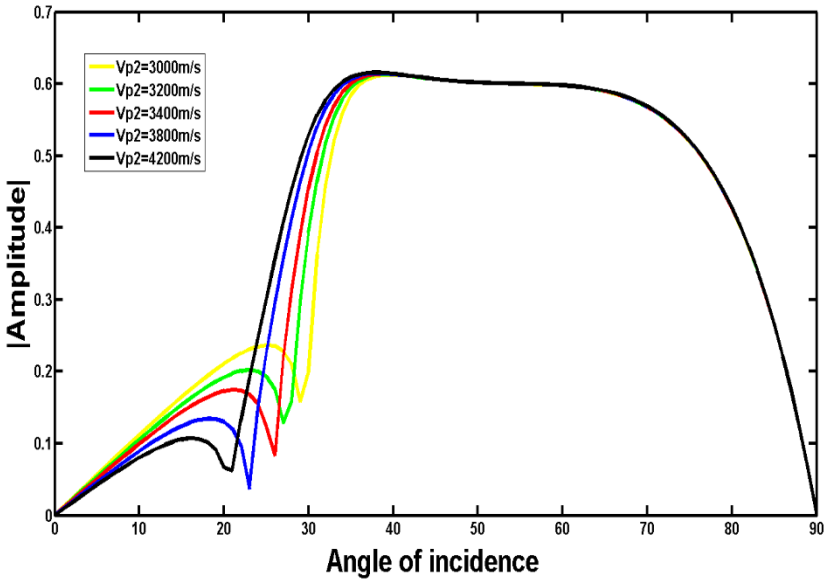

Figure IV-5: Transmission coefficient T_{PS} as a function of incident angle with varying P velocity of hard sea bottom

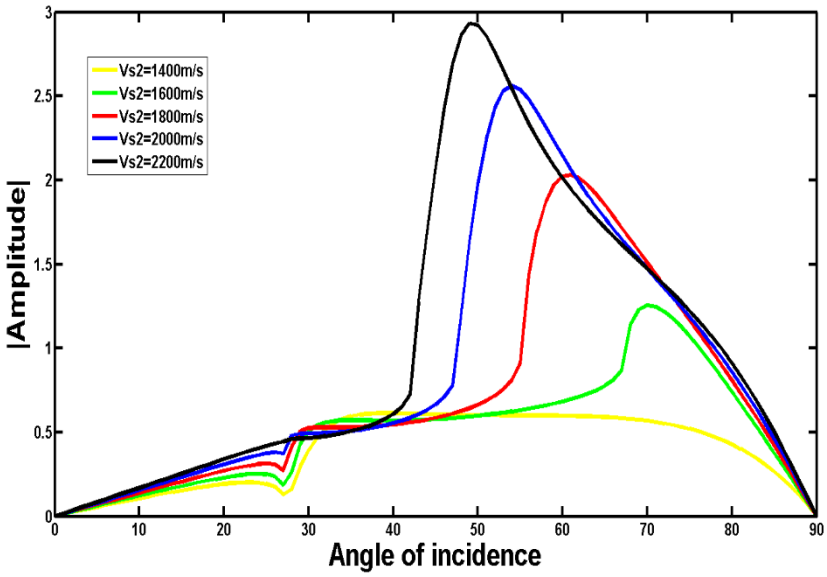

Figure IV-6: Transmission coefficient T_{PS} as a function of incident angle with varying S velocity of hard sea bottom

With the average water depth as shallow as 10 meters and the receiver interval with a length of 25 meters, even the nearest receiver already falls into the post-critical angle zone with acceptable amount of shear waves. The amplitude increases with the source-receiver offset and reaches maximal value at the offset of 4000 m. The SV energy transmitted into the subsurface is nearly a thousand times the amount of P wave energy at the far offset. Accordingly, this special direct shear wave reflection provides a new approach to image the subsurface structure.

4.3.2. Converted Wave Binning

CCP and CMP are two common binning methods, but have fundamental differences in stacking. CCP is basically designed for converted waves, where a down-going P wave converts to an up-going SV wave. The raypath involved in CCP imaging of P-SV wave is shown in Figure IV-7. The horizontal location of image point varies with depth and forms an asymptotic path, moving closer to the receiver as depth is decreasing, since the down-going P wave has a faster velocity than the converted S wave. This variation of the PS common reflection points with depth results in the complicated processing blocks in gathering, mapping and binning the PS wave, where the velocity analyses done with CCP data require pre-estimate of Vp/Vs ratio. In addition, CCP contains the issue that the positive-offset images are different from the negative-offset ones.

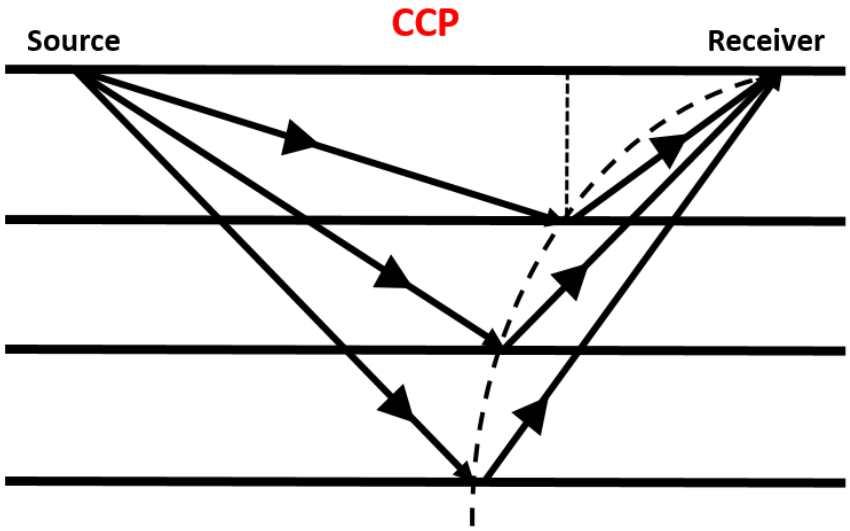

Figure IV-7: Raypaths illustrate propagation paths involved in CCP binning.

Robust CMP stacking algorithms are widely implemented for PP reflected waves but not applicable for the shear wave cases in conventional acquisitions. It has the advantages that the raypath is symmetric and the image points have constant horizontal location over depth (Figure IV-8). For any source-receiver pair in one CMP gather, the corresponding trace is positioned at the same common midpoint. The stacking imaging reflects one single bin located at the middle point between the source and receiver (Figure IV-9). On the other hand, for one CPP gather, the location of image points forms a curved wiggle across several stacking bins (Figure IV-9), which increases the complicity of static and normal-move out time adjustments. Therefore, with this straightforward common reflection point assumption, the processing algorithm of CMP is much simpler and more accurate than CCP.

In the shallow water environment, we expect strong PSS waves, where both downgoing waves and upgoing waves are S wave, as the discussion in the previous section. This special type of converted waves have the similar propagation ray path as the reflected waves without mode conversion (P-P and S-S). In contrast to the conventional PS converted wave, PSS are not applicable to CCP binning but to CMP binning, which lead to simpler processing sequence in velocity analysis and stacking. In addition, the direct shear source is often expensive or not applicable in marine environment. The research on PSS provides an efficient way to obtain the shear wave seismogram.

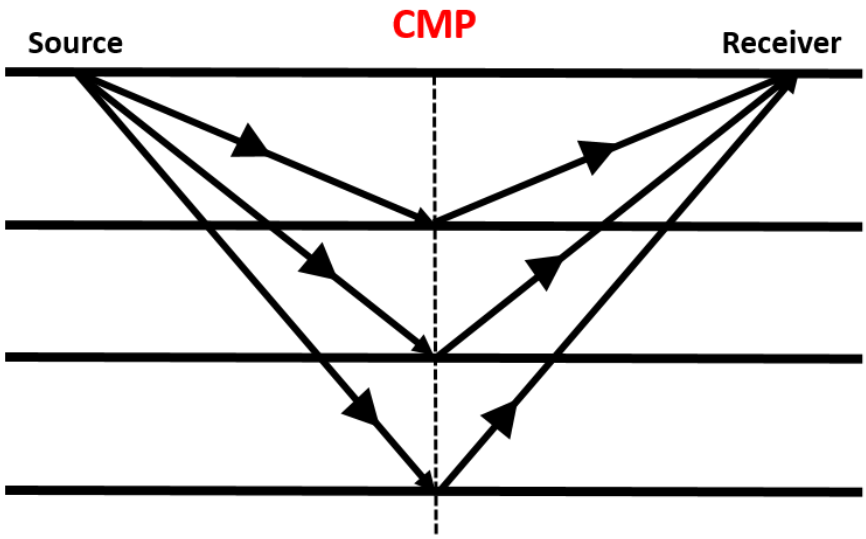

Figure IV-8: Raypaths illustrate propagation paths involved in CMP binning.

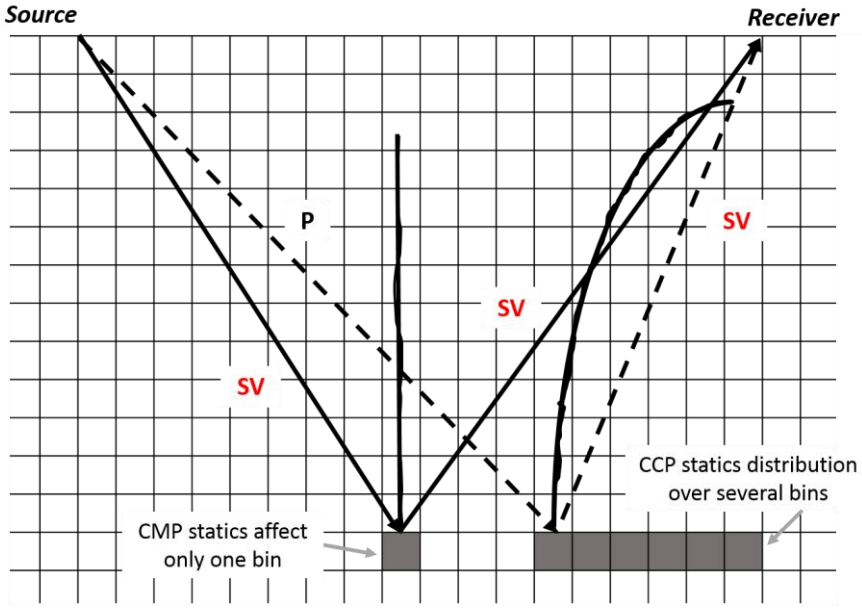

Figure IV-9: Comparison of CMP and CCP image for converted wave binning in different scenarios. (Modified after Hardage et al., 2011)

4.3.3. Phase Changes in Converted Waves

PSS wave involves significant phase variations with offset in the post-critical angle zone, while the stacking requires the stationary reflection phase over the gather for the integrity of the seismic event. Therefore, directly stacking the stretched inline seismogram over a large range of offsets may lead to event cancellations due to the phase changes.

Based on the Zoepritz Equations, Figure IV-10 shows the phase variaions with angle of incidence (equivalently, offset) in a fluid-solid model with the parameters: $V_{P_1} = 1500m/s$, $\rho_1 = 1000kg/m^3$, $V_{P_2} = 3200m/s$, $V_{S_2} = 1700m/s$ and, $\rho_2 = 2500kg/m^3$. In the near offset before the critical angle, it increases sharply to 90

degree incidence angle. When moving to the post critical angle zone, the phase shift occurs, eventually reaching to -π from the initial phase angle at π. At the far offset, the phase angle changes back to slightly below π. This property demands the model based partial stacking in the converted wave processing.

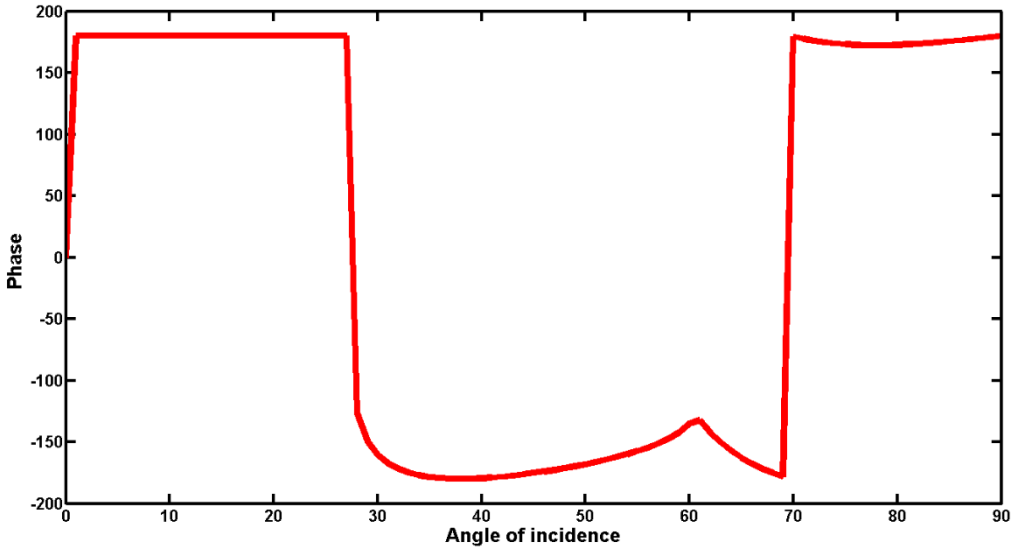

Figure IV-10: The phases changes of PSS wave as a function of incident angle for the model parameters: $V_{P_1} = 1500m/s$, $\rho_1 = 1000kg/m^3$, $V_{P_2} = 3200m/s$, $V_{S_2} = 1700m/s$ and, $\rho_2 = 2500kg/m^3$.

4.4. Method

The proposed processing flow is designed to address the highly dispersive surface wave issue, verify the existence of PSS waves and retain both P and S wave information from the 4C OBC data recorded in the shallow marine environment. The processing sequence for four components are constructed separately according to their different recording schemes.

The common type of noises contained in the 4C OBC data are spikes & noise burst, bubble energy, trapped guided waves, scholte waves and shear leakage. Bubble energy and spikes & noise burst can be eliminated by their very low frequency and high amplitude characters though frequency & amplitude filter. To attenuate the special aliased surface waves, mostly trapped guided waves and scholte waves, multi-domain FK filters are implemented. Due to the surface wave's low frequency and low velocity properties, the data first goes though the time-frequency analysis, bandpass filter, FK filter and f-x dip filter in the shot-domain, and then those operation are repeated in the receiver-domain, the offset domain and the CDP domain. After polarization analysis, the polarization filter is used to separate out the shear leakage and reduce the residual surface waves. At the end, CMP stacking can effectively reduce the random background noises.

To verify and extract the existence of PSS waves in horizontal components, special processing components need to be taken according to their propagation characters. The previous theoretical analysis in 4.3 indicates that the propagation of PSS wave forms a symmetric ray-path for CMP binning instead of CCP binning, which should make the processing simpler. However, when observing the modeling, a

complication is clear that these waves involves several phase changes in the post critical angle zone. This implies that ordinary stacking will cancel the desired seismic event, so the stacking has to be model dependent.

To summarize, 4C data processing is first done through variance filtering algorithm to enhance the overall S/N, and then can proceed individually 1) by processing the data in hydrophone and vertical components to obtain the P-P image, 2) by processing the data in the pressure, vertical and radial components to obtain an SV-SV image, and 3) by processing the data in the transverses component to obtain an SH-SH image. To obtain the shear image, the workflow involves special processing by 1) implementing CMP binning for the PSS wave due to its symmetric propagation path and 2) applying the model based partial staking with the shear log from nearby well as the guided velocity for the velocity analysis.

Combined with previous processing algorithm and methods, a fully 4C OBC pre-processing methodology in SeisSpace is:

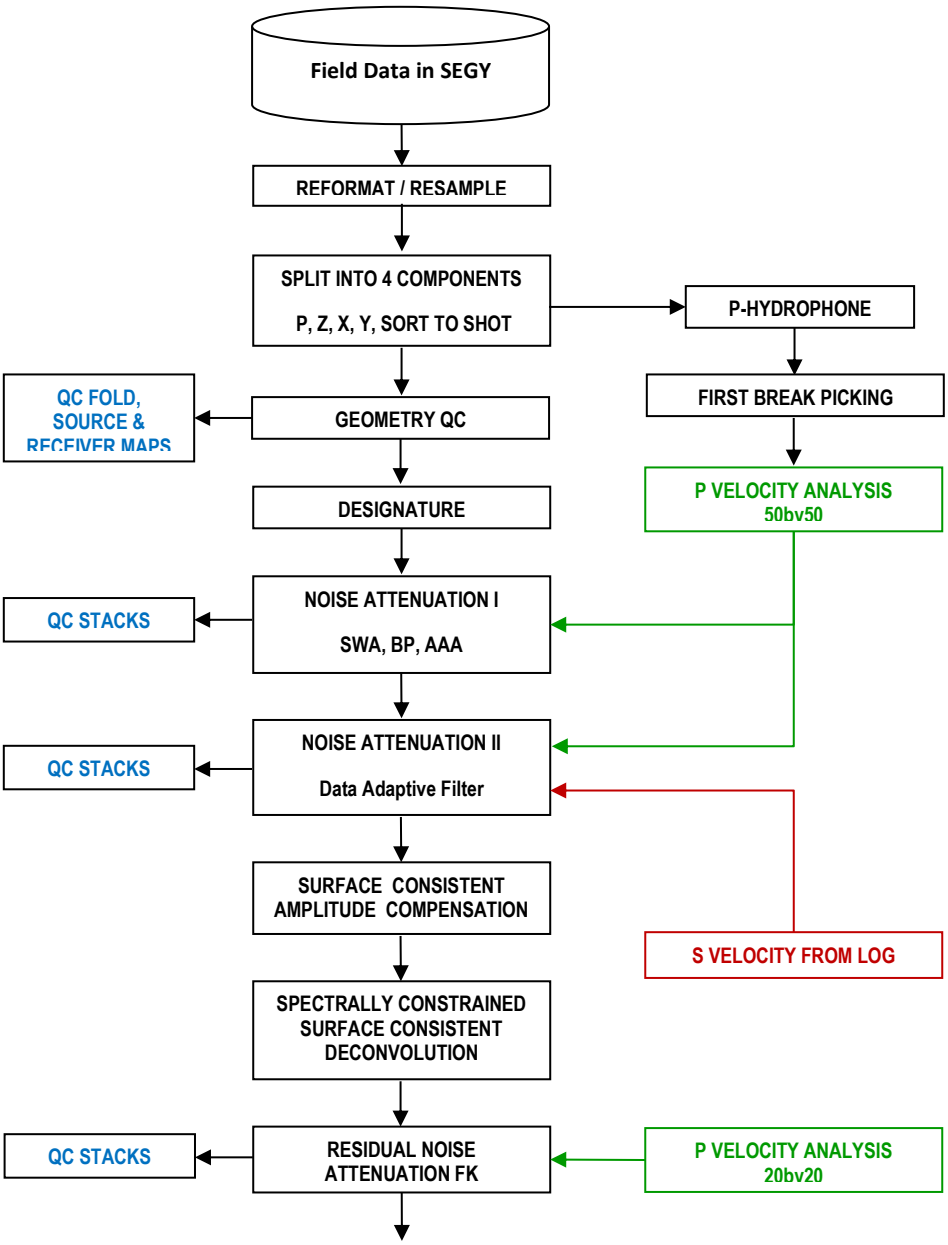

Figure IV-11: Processing work flow.

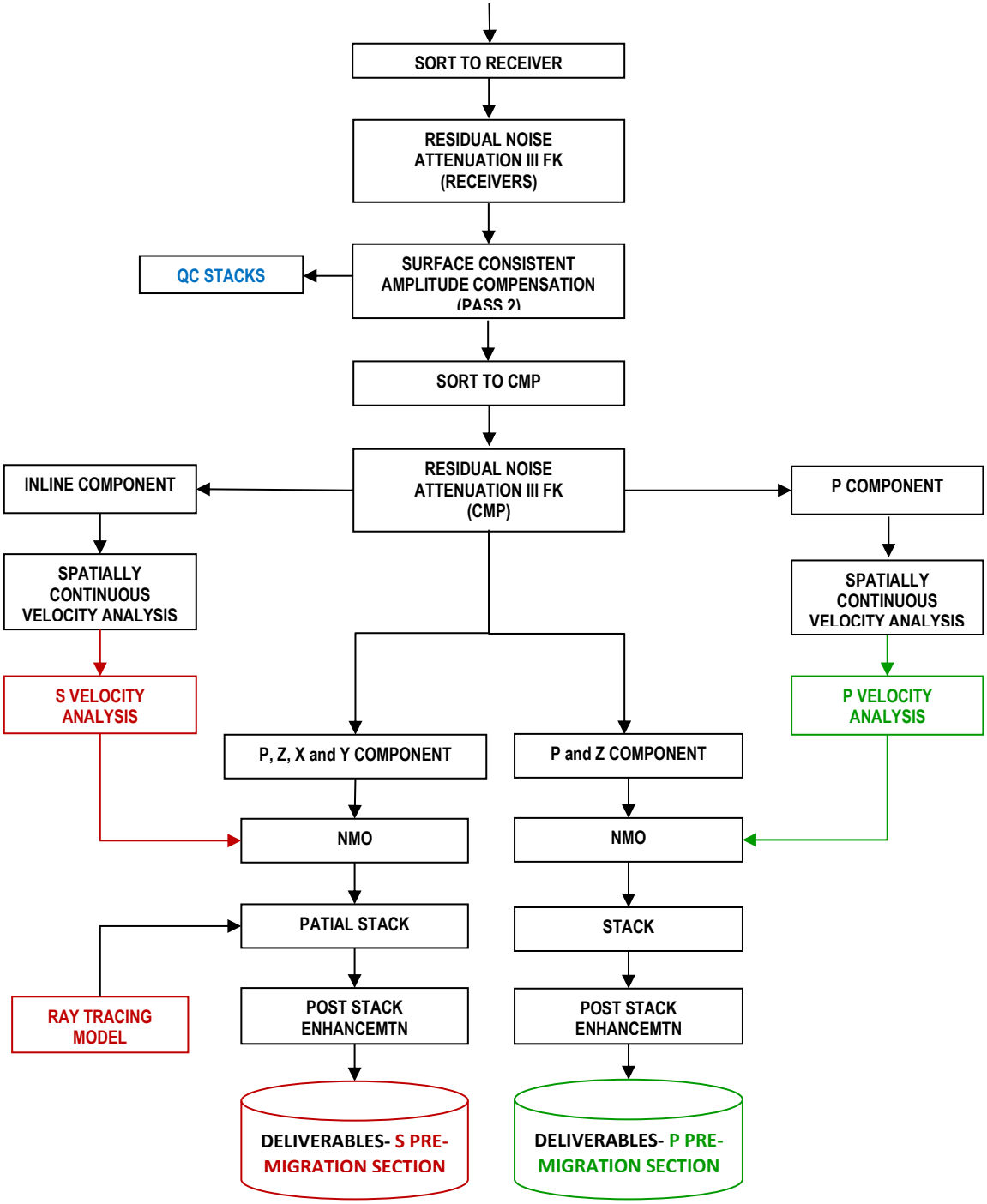

Figure IV-11: Continued.

4.5. Result

4.5.1. OBC Survey Overview

One 2D 4C OBC seismic line acquired in the shallow water offshore field was studied in this research. The data were received from the onboard field processing in SEG-Y format and then were reformatted to WesternGeco's internal processing source-gather seismic file format, where The survey includes one shot line and one receiver line. The shot line consists of 957 valid shot point from an air-gun source acquired at 12.5m intervals along the 63 degree north-east direction, while the receiver line parallels to the shot line, consisting of 322 4C receivers with 12.5m intervals (Figure IV-12). The recording delay is 58ms which proved to be inadequate for this specific acquisition condition and led to additional surface waves. The source-receiver offset ranges from -7851m to 11946m with the full coverage of PSS wave zones. The data was binned into 10m × 10m CDP bins having an average fold of 500 and maximum fold of 1228. These measurement guarantee the reliability of the stacking data (Figure IV-13). The detail acquisition parameters are list in the Table IV-1.

As discussed in the previous chapters, the recorded data suffers severe noise issues due to the harsh acquisition environment. Since this survey was acquired in an area of relatively low activity, the external noise was in the low level. The predominant incoherent noise types encountered during this survey were noise induced by tidal currents and noise induced by weather. The predominant coherent noise type encountered was the high amplitude Scholte wave typical for this area.

Figure IV-14 shows the one shot gather in this 2D seismic line. All four components are heavily contaminated by the ghost surface wave. Beside this, due to the inadequate coupling and vector in nature, geophone data also contains additional noise components including: shear leakage, background noise, source-generated noise, and instrument noise. All of those noises can be seen as coherent or incoherent energy in seismic gathers.

In order to get better understanding of the spectrum properties of different waves, the record was decomposed into different frequency bands. For pressure component (Figure IV-15), there are strong low frequency surface waves in the frequency zone 8-25Hz and the reflected signals dominate clearly in the zone 20-55Hz. Different from the conventional tow-streamer data, high frequency surface waves with velocity ranging from 1100 to 1300m/s occupy the same location as the reflected waves mainly in the frequency zone 45-70Hz and extend to even higher frequency band. There also exist strong acquisition footprints in the zone of 45-70 Hz. Vertical component (Figure IV-16) contains the same issues with both low and high frequency surface wave, but in a higher noise level. The reflect signal cannot be easily detected as the hydrophone component. For inline component (Figure IV-17), it is hard to define the reflected waves zone while the low frequency surface waves mainly locates in the frequency band below 25Hz. Surface waves are highly mixed with reflected waves in the crossline component (Figure IV-18).

The interactive spectral analysis of the hydrophone component is shown in Figure IV-19. The frequency-offset plot reveals that no significant meaningful signal

was present above 80Hz. Based on this finding, the data can be resampled to 4ms in order to make the processing effectively. Very high frequency (>80Hz) noise locates in the near offset traces, which is related to the coherent engine noise due to improper acquisition parameters.

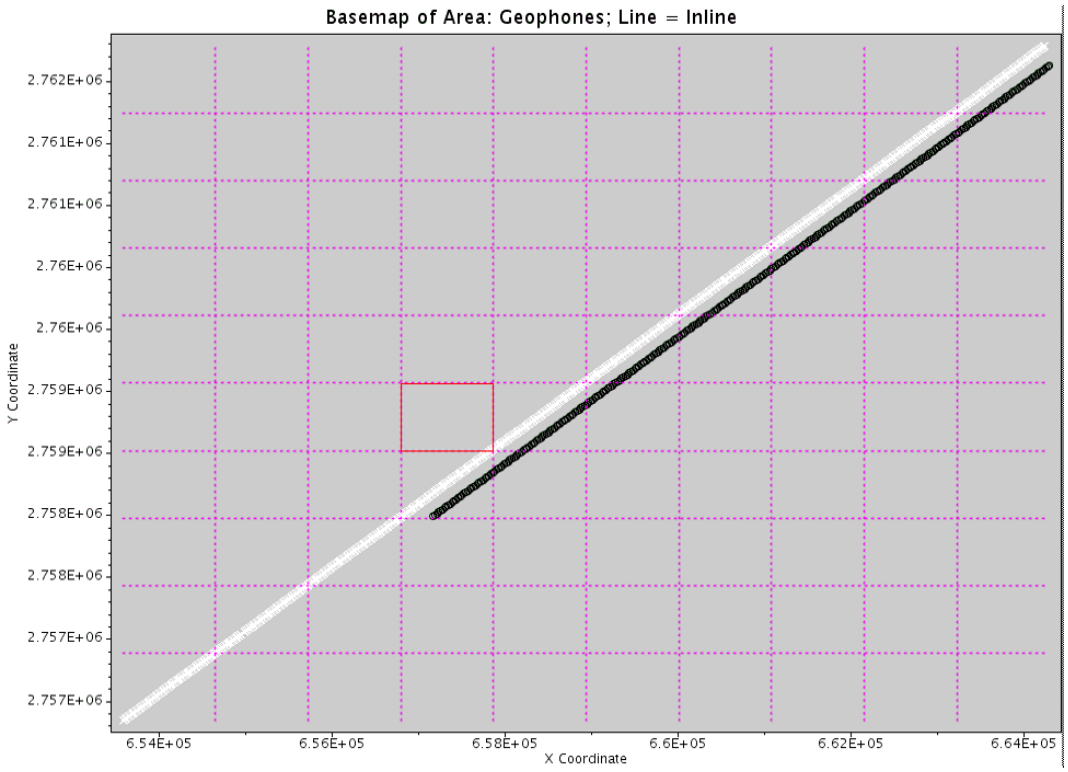

Figure IV-12: Base map of the 2D seismic line

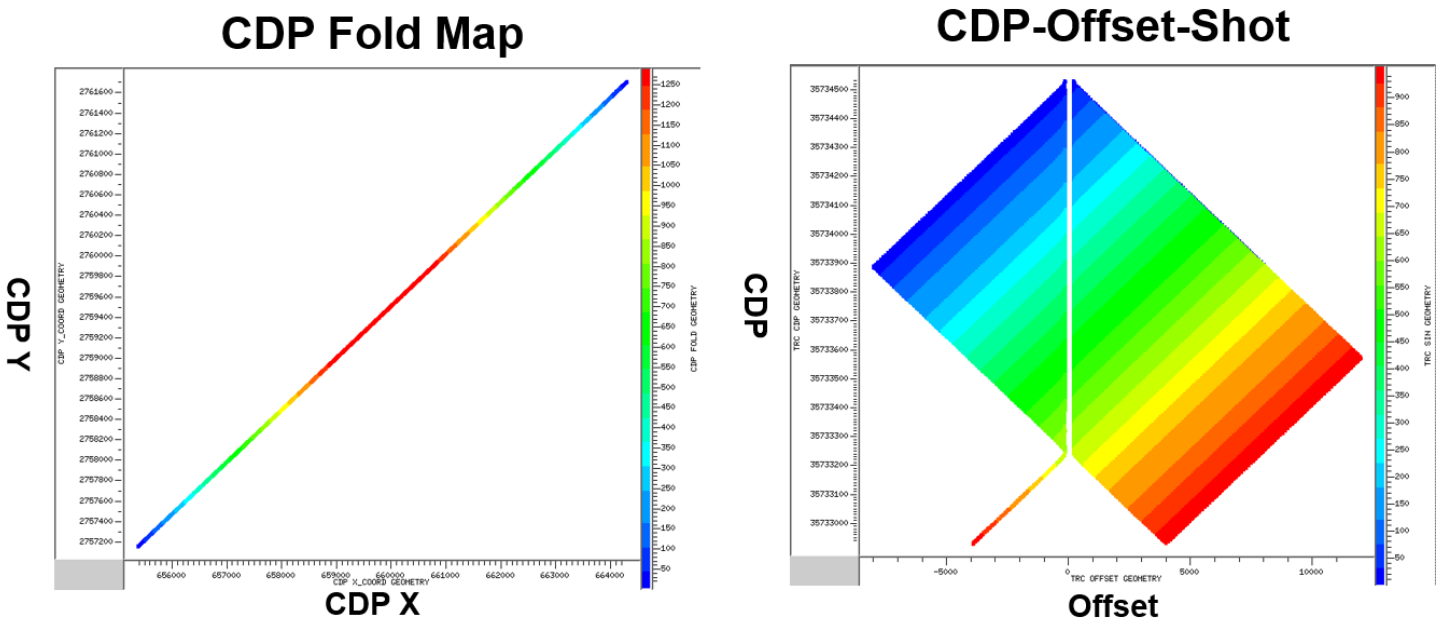

Figure IV-13: (a) CDP Fold Map; (b) CDP-Offset-Shot map of the 2D survey.

Table IV-1: Acquisition parameters

Total number of live groups	322
Total number of shot	957
Source type	Sleeve airguns
Source depth	4m
Source volume	1500cu/in
Source pressure	2000psi
Shot point interval	12.5m
Cable type	Q-seabed
Receiver group interval	12.5m
Receiver/Group	Single sensor
Source-receiver azimuth	63 deg
Total number of CDPS	1601
Maximum CDP fold	1288
Number of offset bins	101
Longest offset line	11946
Instrument low cut filter frequency	3Hz
Instrument high cut filter frequency	200Hz
Number of samples per trace	3585
Sample rate	2ms

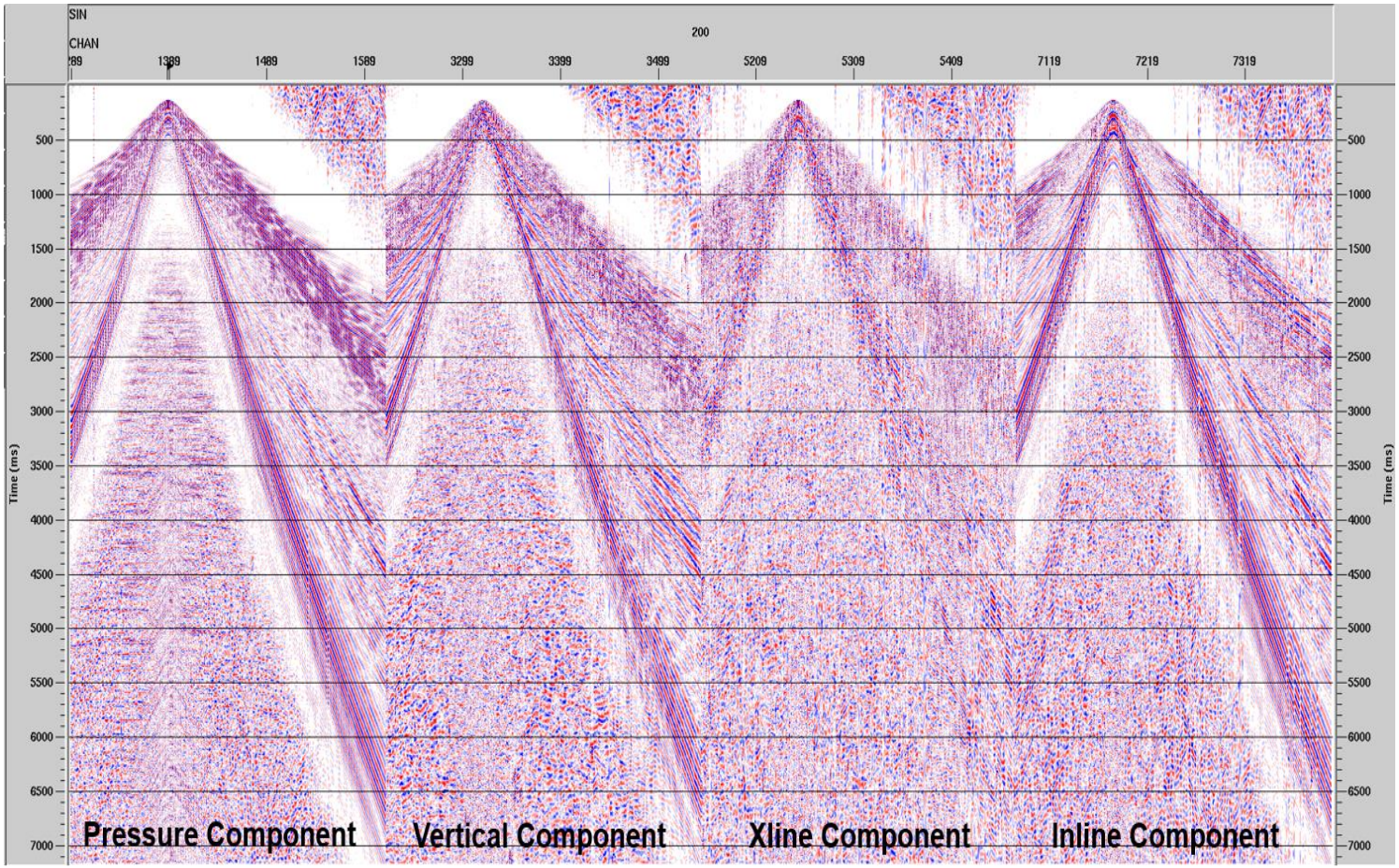

Figure IV-14: Typical 4C shot gather in the 2D line: Pressure Component, Vertical Component, Xline Component and Inline Component (from left to right).

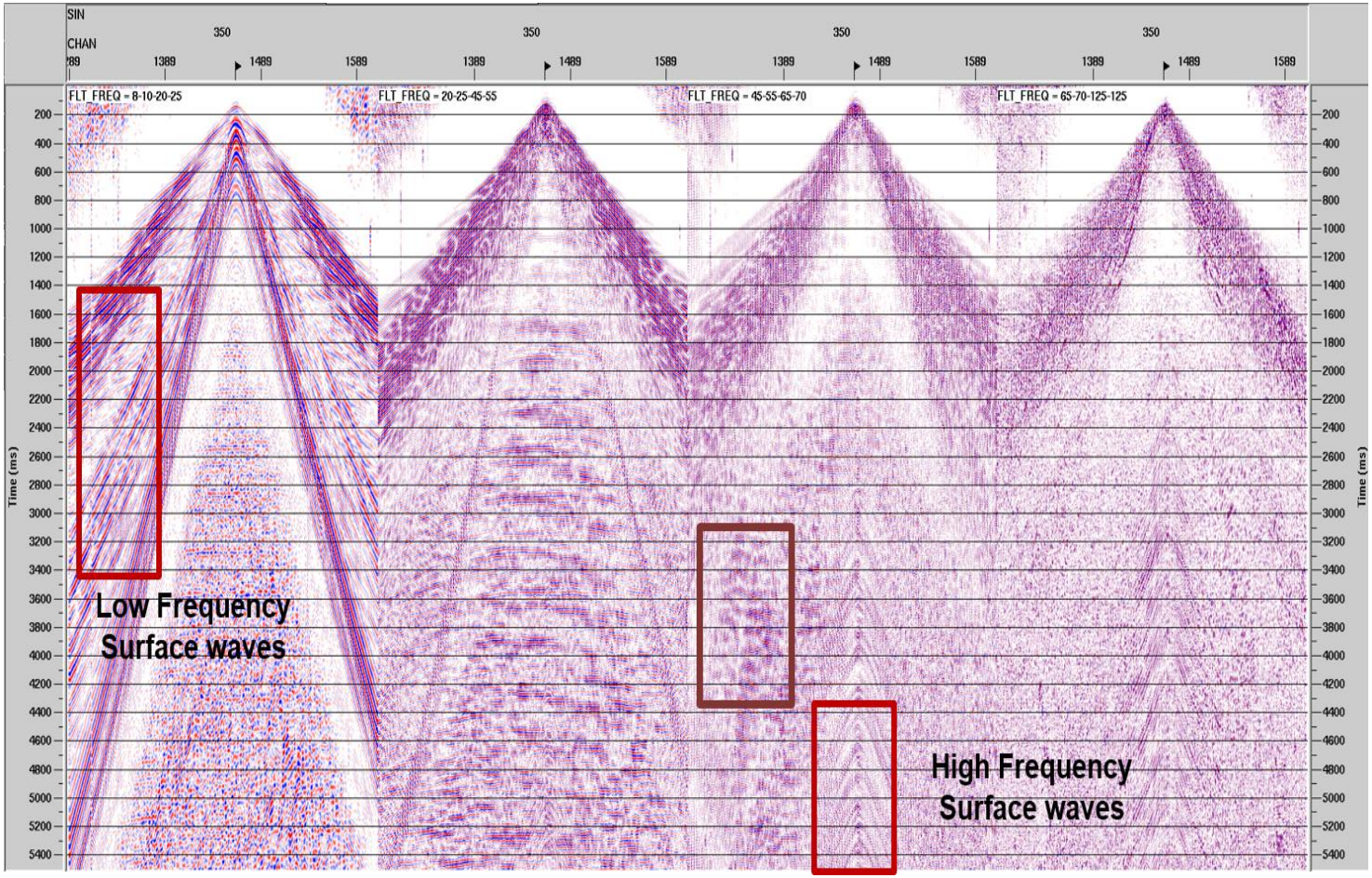

Figure IV-15: Frequency decompensation of pressure component

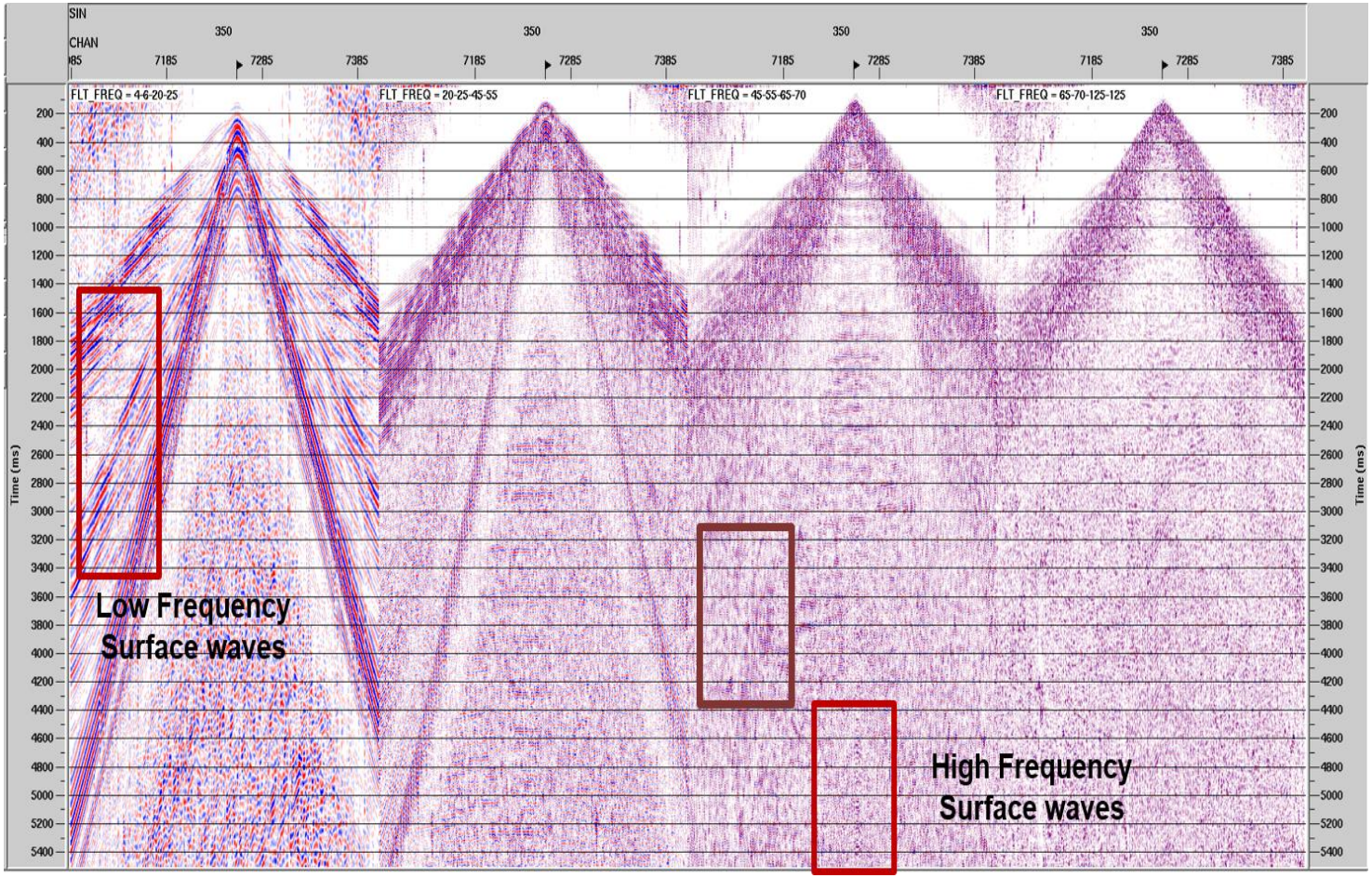

Figure IV-16: Frequency decompensation of vertical component

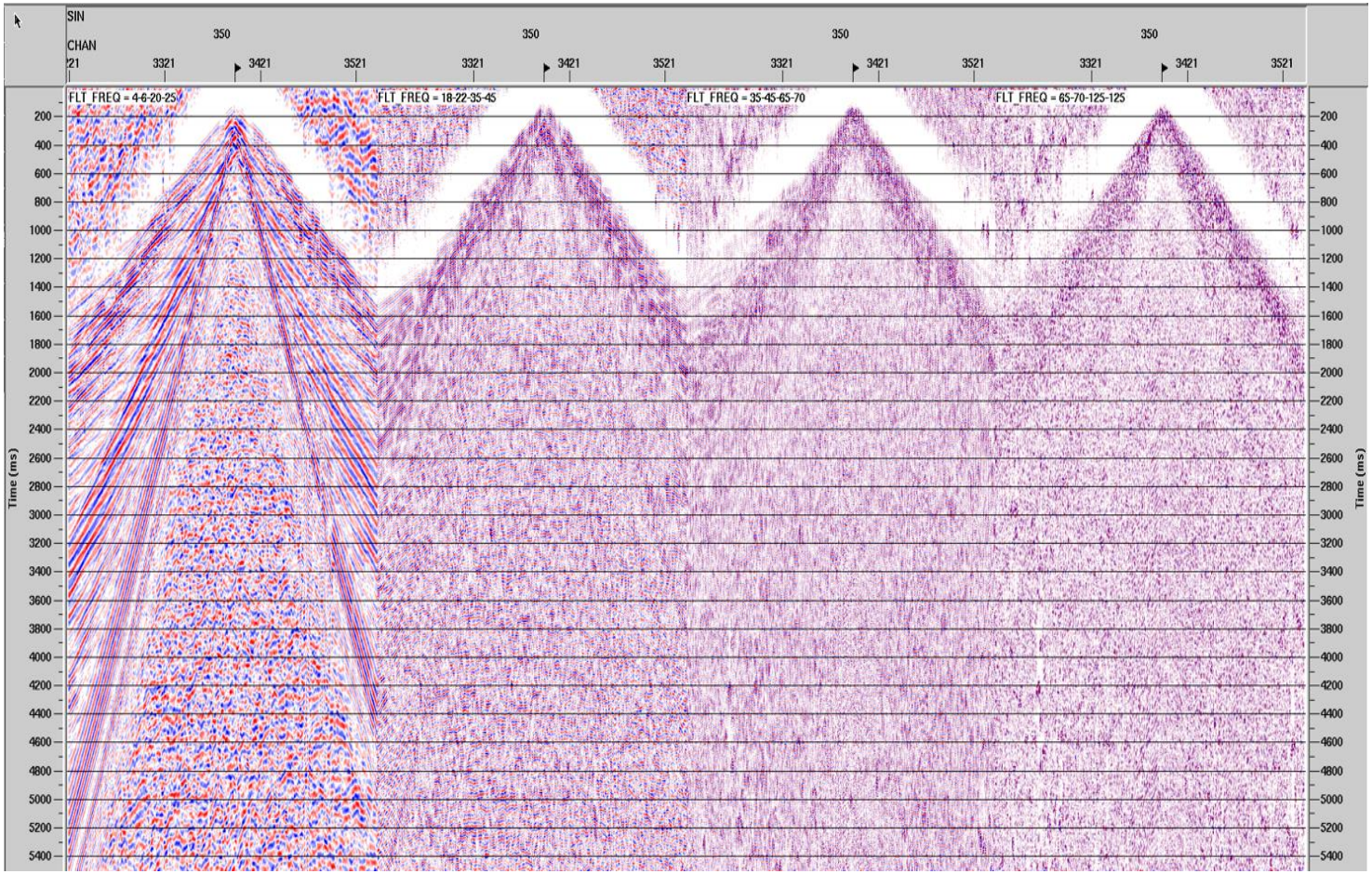

Figure IV-17: Frequency decompensation of inline component

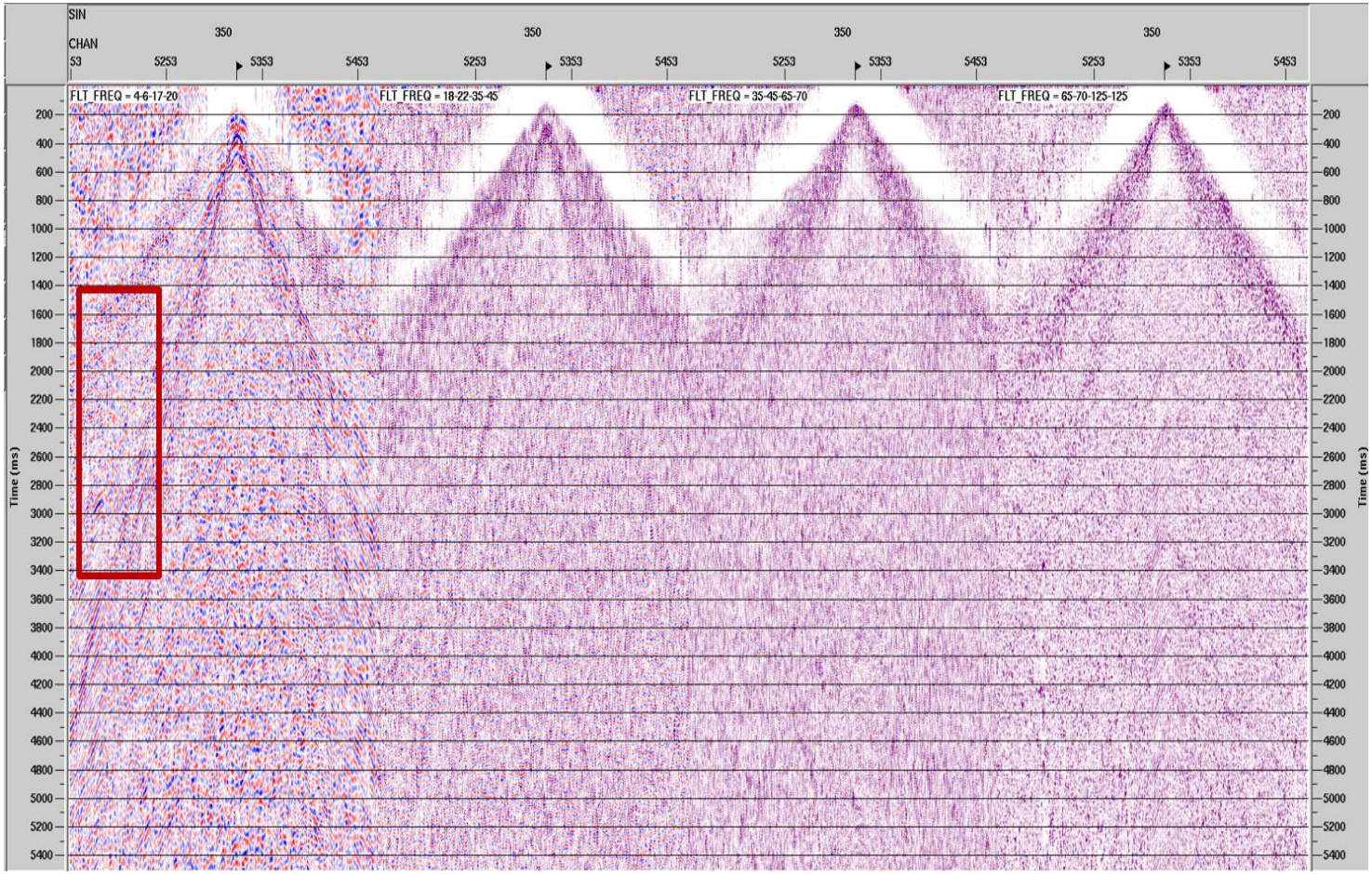

Figure IV-18: Frequency decompensation of crossline component.

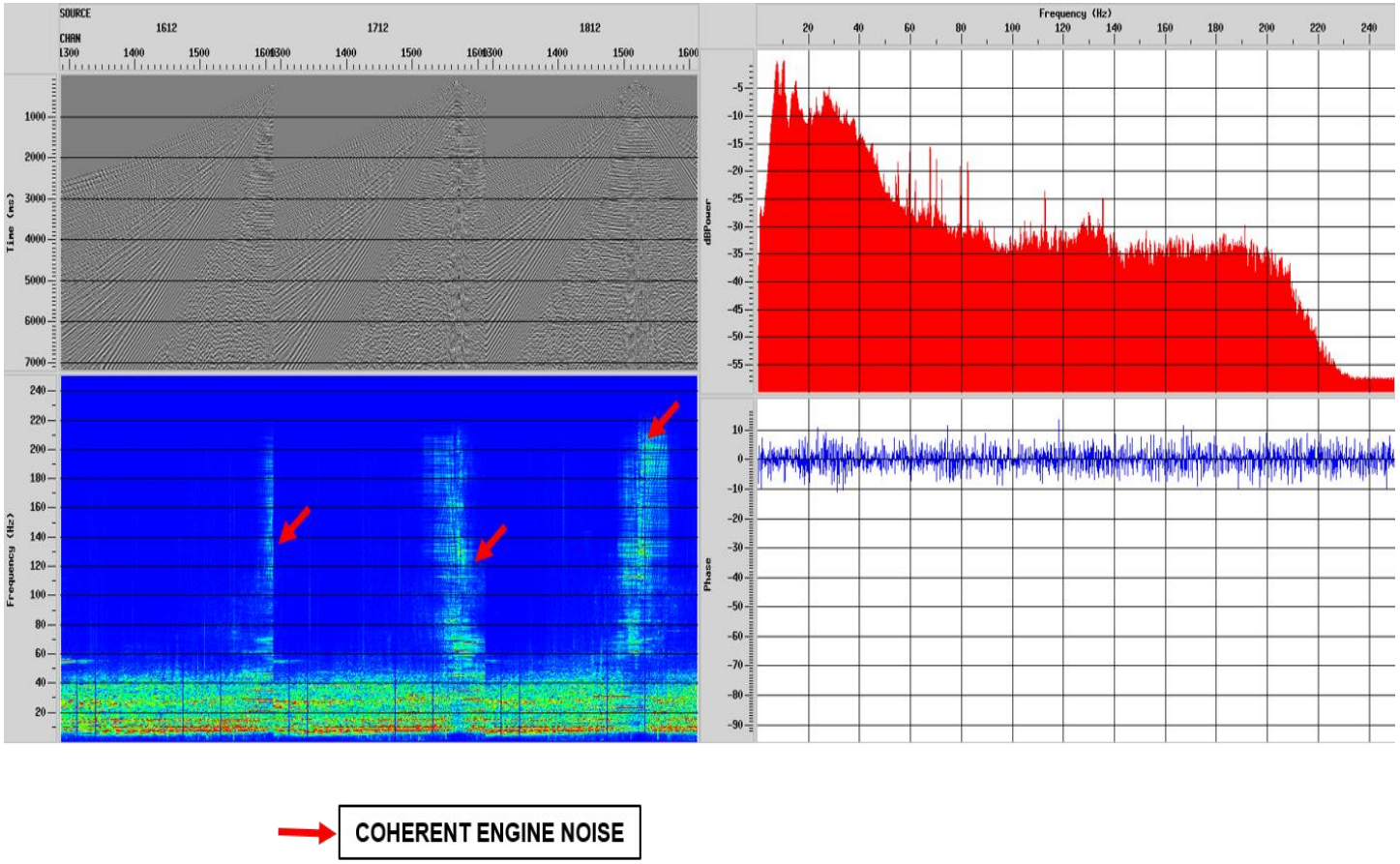

Figure IV-19: Interactive spectral analysis of the pressure component.

4.5.2. Well Log Data Analysis

We have access to information from a well close to the seismic line. The well logs include P and S-wave velocities for part of the well at the reservoir location. From this we calculated an average VP/VS ratio and used this to establish an expected S velocity depth profile.

Figure IV-20 lists the gamma ray, density, P and S velocity logs at the reservoir location. The gamma ray response indicates the local formation is relatively pure sand. Comprehensive interpretation of density and velocity logs shows that the reservoir top locates at 1.516 sec with depth about 2800m. With this limited log information (Figure IV-20), the average VP/VS ratio is calculated as 1.815. In order to derive the velocity log for the whole well section, one nearby water injection well (distance 102m) with full P velocity is referred to determine the P/S velocity profile for the seismic well tie.

Based on the information provided by the vendor and the well log interpretation above, the main objective is to image two oil and gas bearing formations from the seismic as follows:

- **For P section**: Arab formation at about 1.53 sec TWT and depth of 2790m at the crestal area and 1.6 sec, depth 3020m on the flank. Khuff formation at about 2.0 sec TWT and depth of 3990 m at the crestal area and 2.1sec, depth 4200m on the flank.
- **For S section:** Arab formation at about 2.78 sec TWT at the crestal area and 2.94 sec on the flank. Khuff formation at about 3.63 sec TWT at the crestal area and 3.82 sec on the flank.

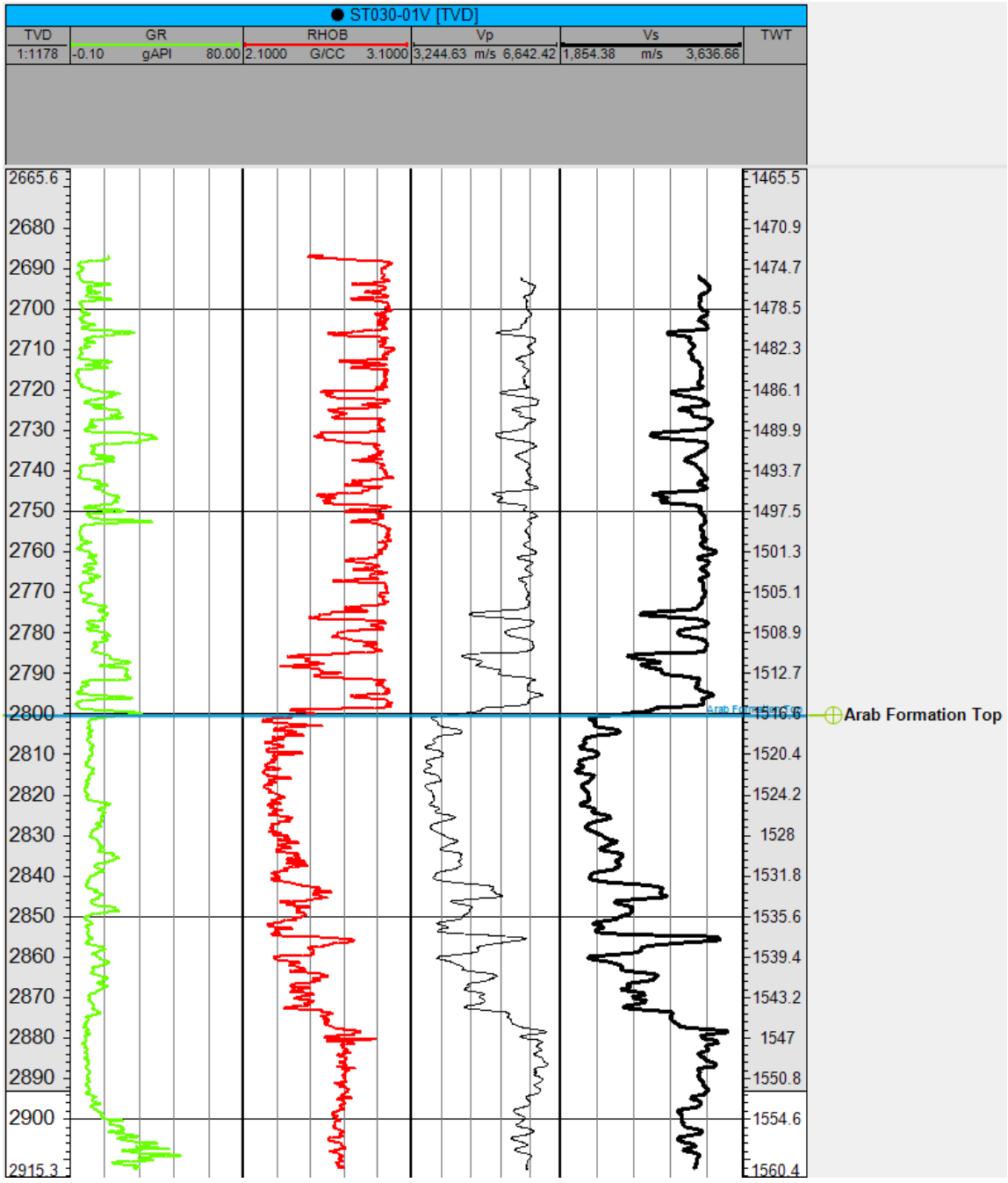

Figure IV-20: Gamma ray, density, P velocity, S velocity (from left to right) at the reservoir zone of the nearby well. The target formation is Arab Formation which is at 1.516 s of the two way travel time.

4.5.3. Modeling Result from Previous Work

Sun and Berteussen (2009a) performed the two-dimensional full-waveform elastic wave modeling with a 20-lay velocity model (Table IV-2) by directly solving the wave equations. The modeling result of inline component (Figure IV-21) demonstrates that the shear waves, which have the polarity changes, are generated at the water/seabed boundary and propagate deep into the solid layers.

Furthermore, we build the synthetic shear wave at the reservoir location using the well log data. Figure IV-22 shows that the correlation between the inline geophone at well location and the synthetics seismogram is great. This verifies that the horizontal geophones record strong PSS reflection waves generated by the shear source at the sea bottom. For further verification, we plot the very top part of three geophone raw records in Figure IV-23, Figure IV-24 and Figure IV-25. The inline component (Figure IV-23) shows very obvious polarity changes at the top part without any processing, while the seismic events are continuous in the vertical (Figure IV-24) and crossline (Figure IV-25) components.

All the elastic wave modeling, the seismic-well tie result and the field data demonstrate that the expected direct shear wave should exist in the 4C OBC records and the shear wave reflections at reservoir interfaces are strong.

Table IV-2: Twenty-layer velocity model parameters

Depth (m)	Density (g/cc)	Vp (m/s)	Vs (m/s)
0	1050	1480	0
15	2100	1994	750
35	2200	3080	1240
60	2450	4500	2110
95	2350	1586	1078
260	2620	3714	1799
560	2490	3257	1718
755	2350	3555	1747
1220	2470	4003	2075
1800	2650	5381	2905
1915	2530	4347	2293
2065	2530	3794	1857
2290	2630	5231	2630
2365	2560	4025	1994
2370	2680	5203	2681
2375	2500	3758	1924
2385	2310	3835	1935
2425	2380	4066	2047
2455	2550	4950	2607
2480	2660	5581	3000
2500	2660	5581	3000

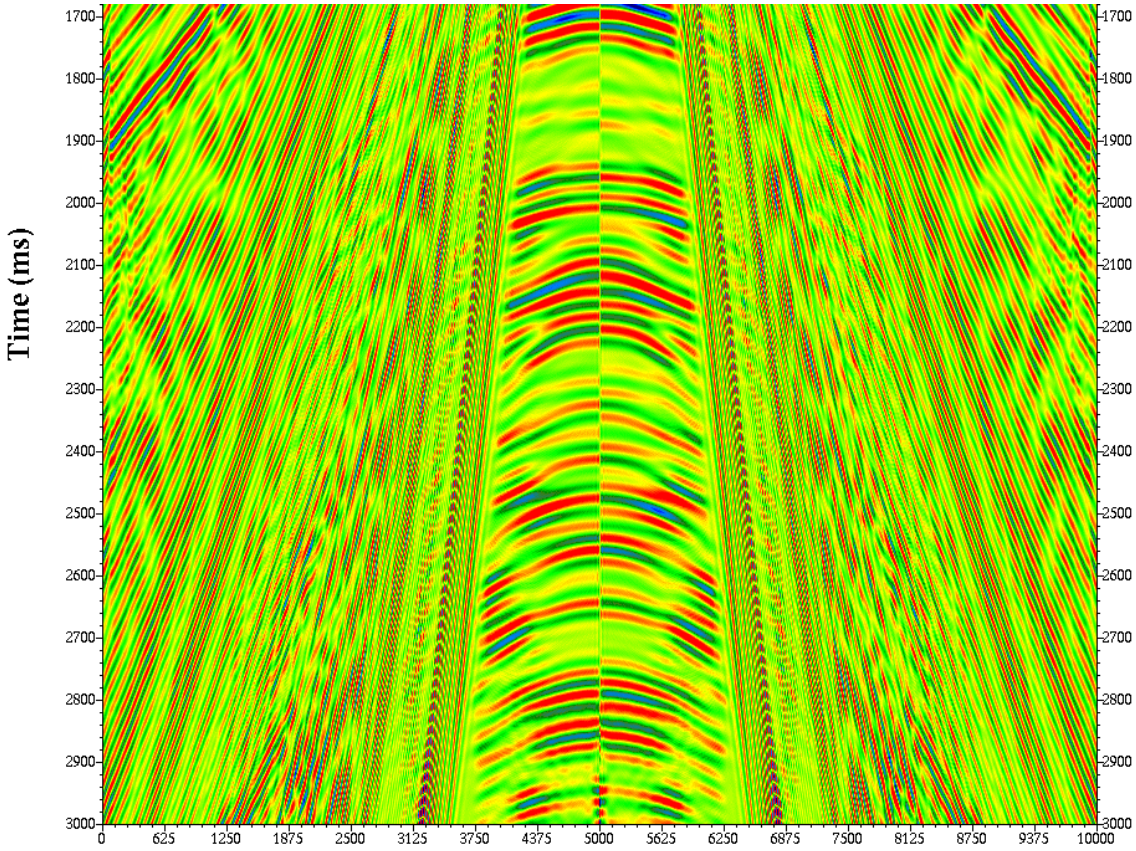

Figure IV-21: A portion of the synthetic inline geophone record obtained from 2D full-waveform elastic wave modeling using the 20-layer velocity model (Sun and Berteussen, 2009a).

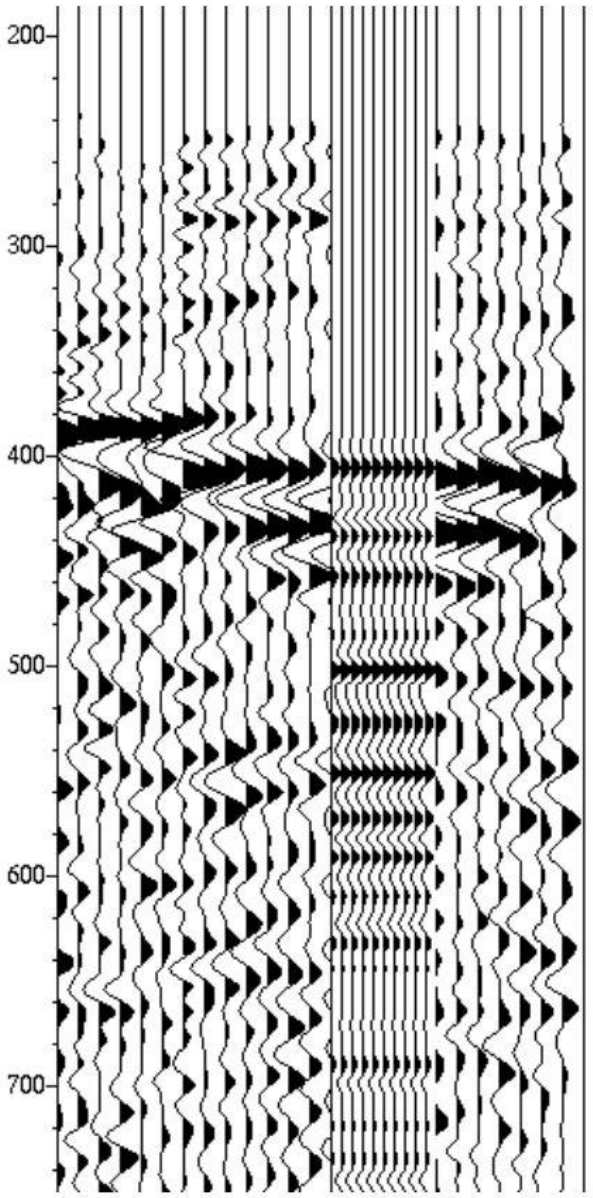

Figure IV-22: Comparison of offset inline geophone data with synthetic S-wave data (Sun and Berteussen, 2009a).

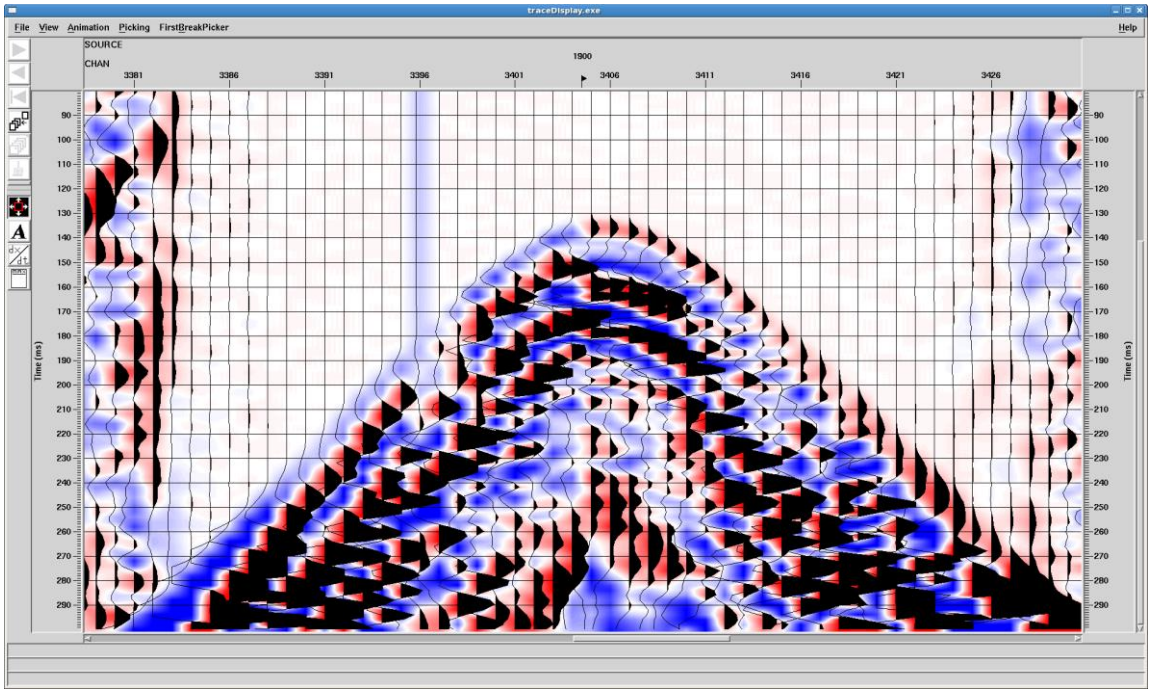

Figure IV-23: Enlarged part of the inline component of the shot gather close to the well location.

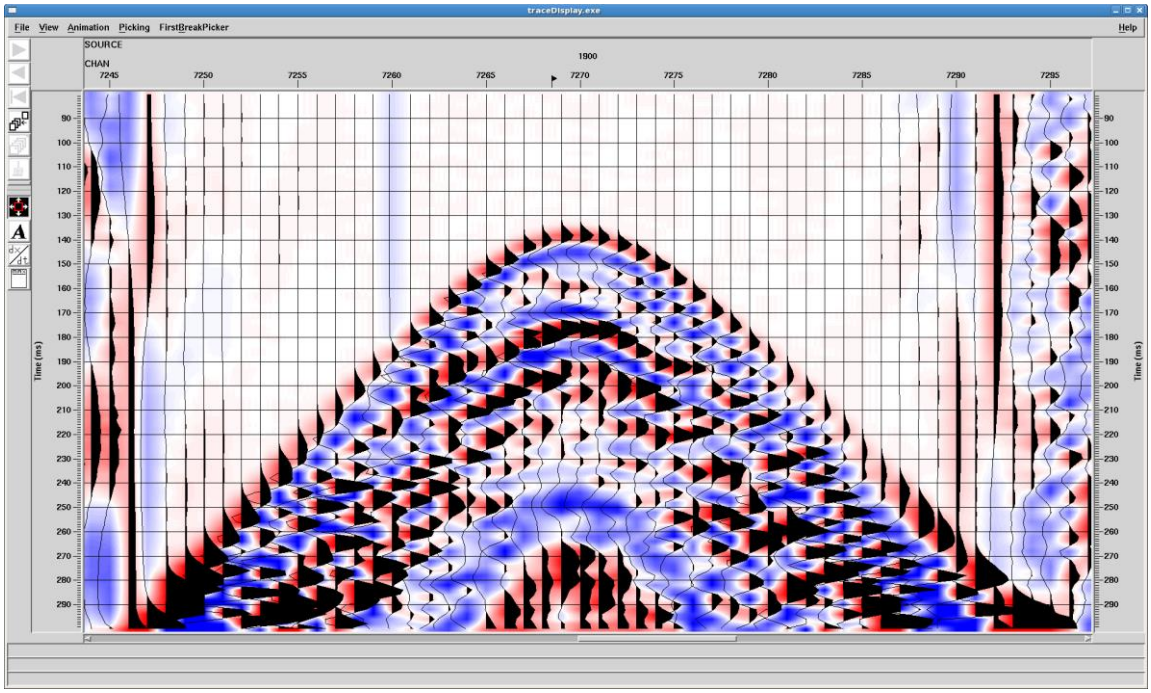

Figure IV-24: Enlarged part of the vertical component of the shot gather close to the well location.

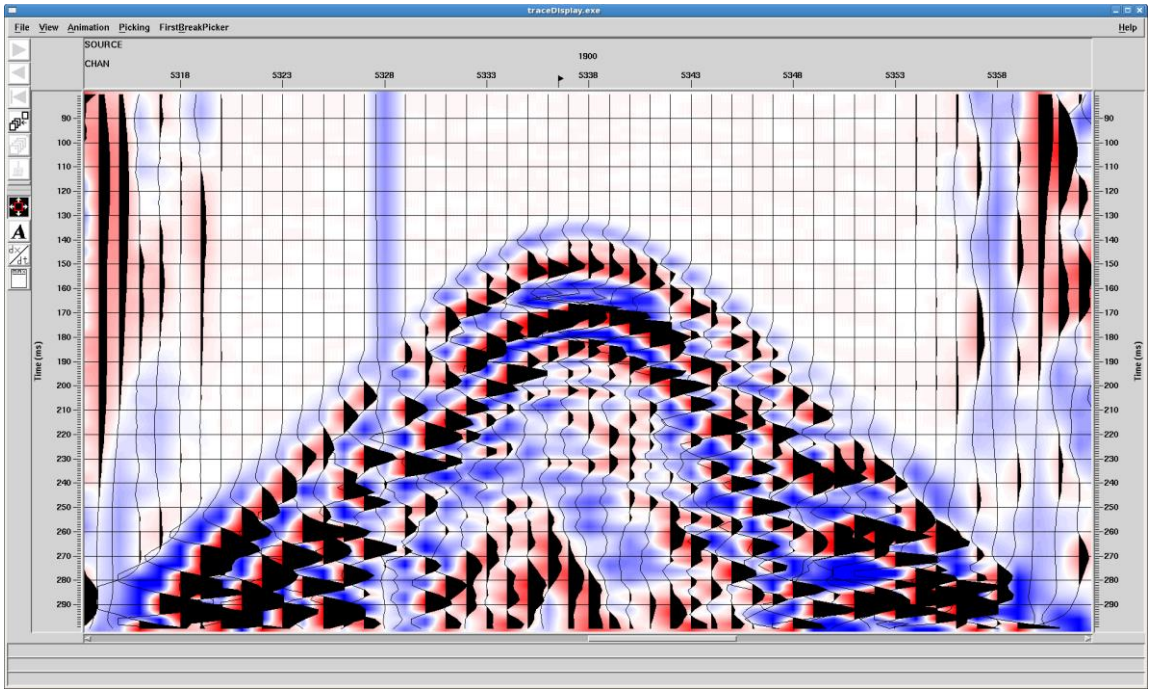

Figure IV-25: Enlarged part of the crossline component of the shot gather close to the well location.

4.5.4. Processing Result

The main objective of this processing project was to provide new seismic products to the exploration group with a structural image and the reservoir group for the purpose of reservoir development, modeling and inversion goals. The major data processing project goals are: 1) Enhancing S/N with advanced noise attenuation in multiple domains. Attention needed in processing flow for noise and other issues such as mud roll, random noise, anomalous amplitude, 3-component fidelity phase, coupling, and surface ghost, etc. 2) Improving pre-salt imaging and 3) Detecting the shear wave information from horizontal components.

We follow the designed workflow in the Figure IV-11 in Section 4.4. As we discussed in the previous chapter, the first step of the processing is to improve the overall signal to noise ratio. Beside the highly spatial aliased surface waves, the coarse P velocity analysis panel (Figure IV-26) indicates the records contain strong water-column reverberations (short period multiples) and interbeded multiples (large period multiples). The S velocity panel (Figure IV-27) indicates that the short period multiples are even more servere in the horizontal components, which exceedingly decrease the accuracy of the interactive velocity picking. With the goal of resolving the subsurface structure on the current stage, we make it a higher priority to attenuate surface waves and separate out the short period multiples.

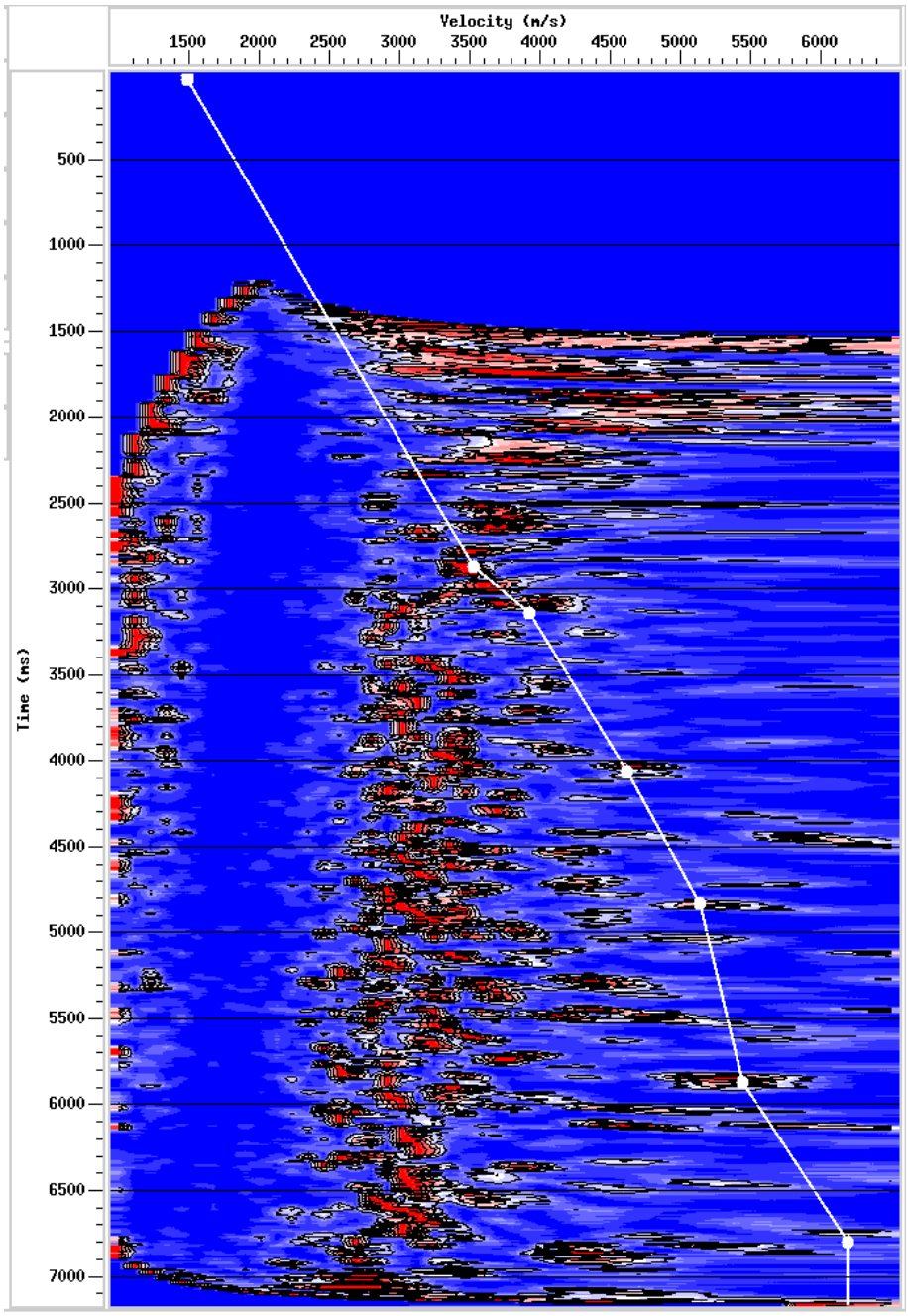

Figure IV-26: Velocity semblance panel of P velocity.

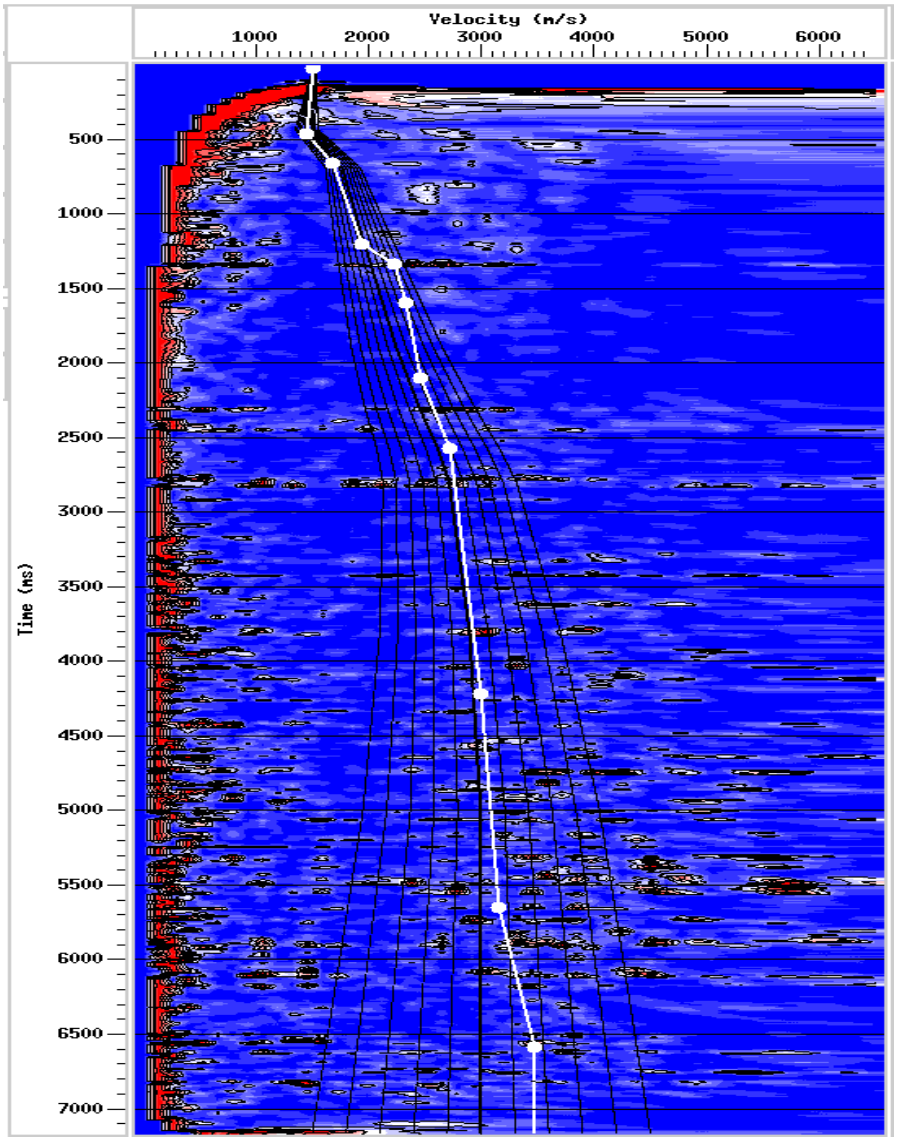

Figure IV-27: Velocity semblance panel of S velocity.

The workflow involves several rounds of de-noising process with various methods in different sorting domains. Anomalous amplitude attenuation (AAA) and data adaptive filter aim to attenuate random noise by transforming the processing gather into the frequency domain and applying different spatial median filter. Surface wave attenuation (SWA) and FK filter are approaches for coherent noise suppression, based on waves' velocity and frequency properties respectively. Predictive deconvolution is applied to eliminate the short period multiples. It is challenging to define one sorting domain to separate out both the receiver side noises and source side noises. Figure IV-28 shows the FK panel of hydrophone records (after short domain de-noising) in receiver sorting. The obvious surface wave energy appears as coherent noise where it is random noise and difficult to identify in the shot domain and eliminated by shot domain de-noising previously. Thus, the noise attenuation process is implemented in the receiver, shot and CMP domain. The comparison between the raw data and the processed record of the inline component (Figure IV-29) in the FK domain demonstrates that the processing sequence effectively eliminates most surface wave noises and the hidden reflected signals (hyperbolic line) turn up.

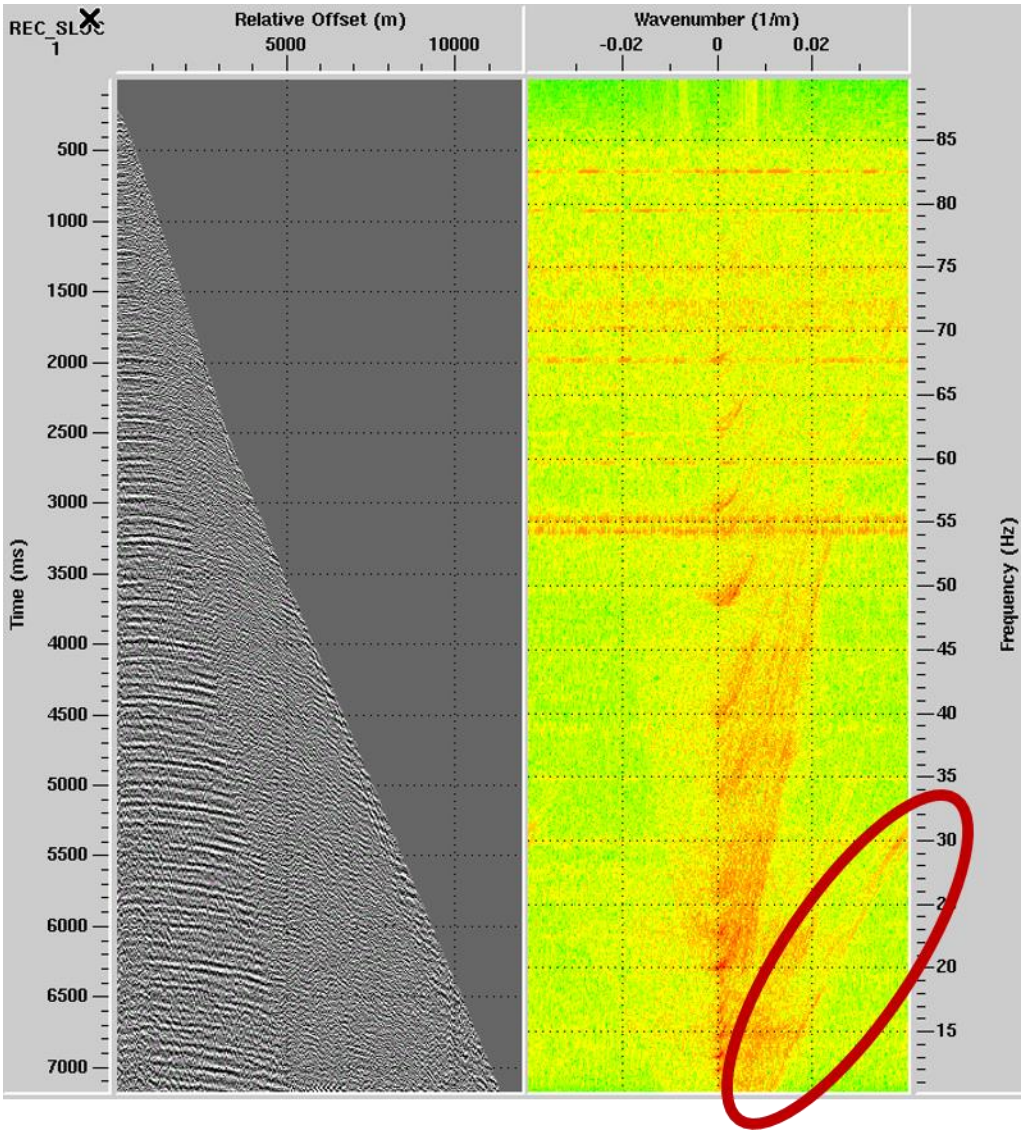

Figure IV-28: Residual noises exist at FK domain in the receiver domain after the FK in the source domain.

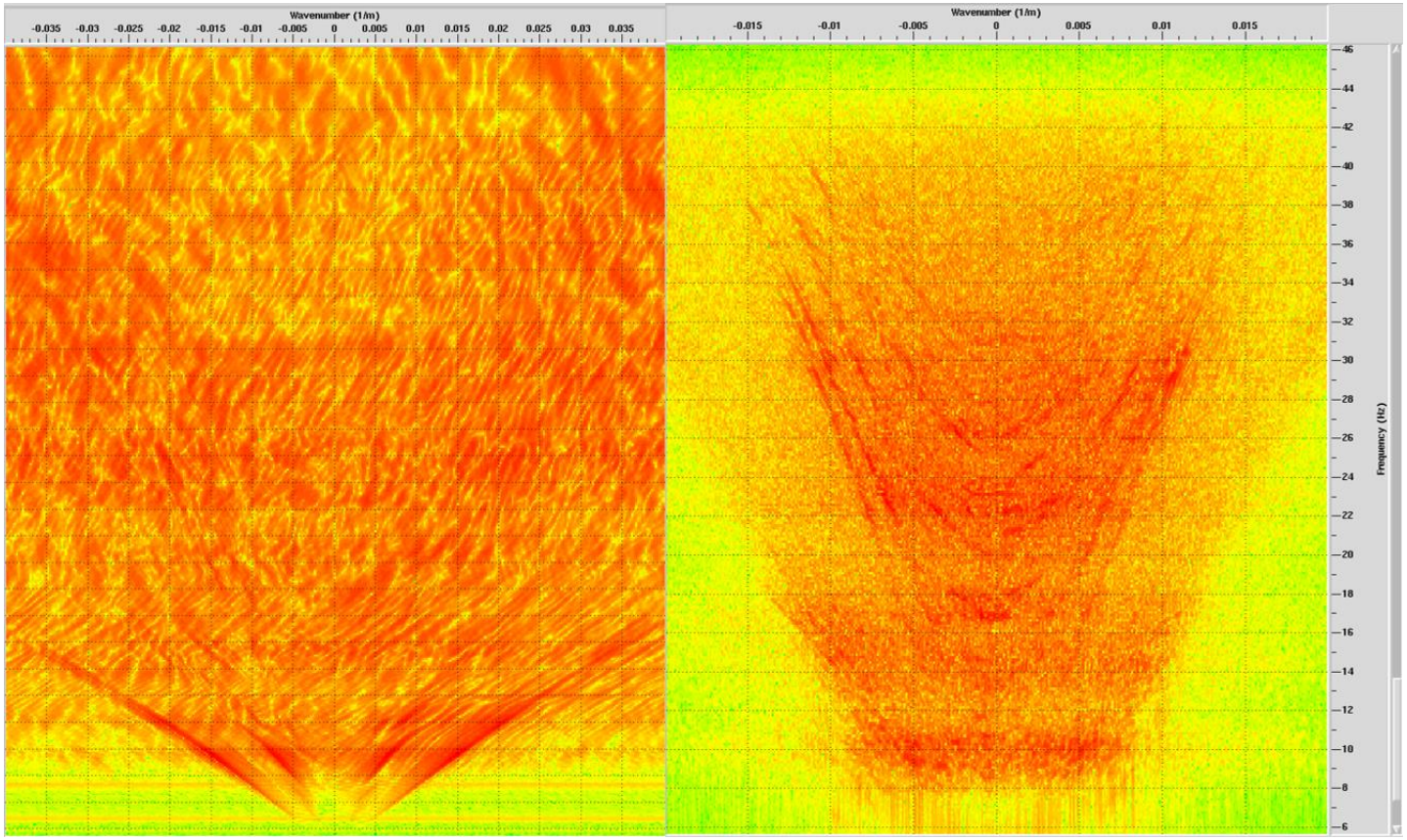

Figure IV-29: FK panel comparison of the inline component before and after the FK filtering.

The stacked P velocity section from the pressure component (Figure IV-30) shows the anticline structure exists near the well location below 1.3s, while other geological structure is relatively flat, which is consistant with the structure interpretation from the vendor. The P stacked section of vertical component (Figure IV-31) exhibits similar structure and furthermore verifies this result. Thus, we expect to obtain a corresponding structure section from the shear waves stacking response, if the PSS wave assumption is true and the processing sequence is reliable and applicable.

Figure IV-32 displays one CDP gather of the inline component after the NMO correction using the shear velocity. Distinct phase changes occur at offset=2000m and offset=4000m, which matches the Zoepritz modeling result (Figure IV-33). Based on this observation, partial stacking are utilized in the shear wave processing with three different offset ranges: 0-2000m, 2100-3900m and 3500-4500m. The SV-SV seismic sections often suffer the low S/N and low resolution issues, partially when the propagation path goes though the high heterogeneous subsurface in the shallow water environment. And two horizontal components contain higher noise level than vertical and pressure components. Therefore, the energy is not well balanced and the lateral event continuity is not sustained in the color-displayed SV-SV section from the horizontal components. The black-white display is used for the better structure detection and comparison on the current stage.

The near offset stacking (Figure IV-34, Figure IV-35, Figure IV-36, Figure IV-37 and Figure IV-38) shows best resolution and the anticline structure are clearly displayed on the stacked sections from all four components. Due to the complicated

phase changes in the middle offset range, the poor continuity of the seismic events influences the stacking result in this offset range (Figure IV-39, Figure IV-40, Figure IV-41, Figure IV-42 and Figure IV-43). We expect to have strong converted wave in the far offset. However, the far offset stacking (Figure IV-44, Figure IV-45, Figure IV-46, Figure IV-47 and Figure IV-48) suffers strong residual surface waves and the NMO stretch, which all result in a deteriorating structure in the stacked section. Thus, the near offset stacking of shear wave illustrates better resolution and high S/N.

In order to verify the reliability of the stacked sections, we compare the P and S stacked section in depth (Figure IV-49, Figure IV-50, Figure IV-51, Figure IV-52, Figure IV-53 and Figure IV-54). The S stacked section shows consistent and clear structural trend as the one from the P waves, which verify the existence of the PSS waves.

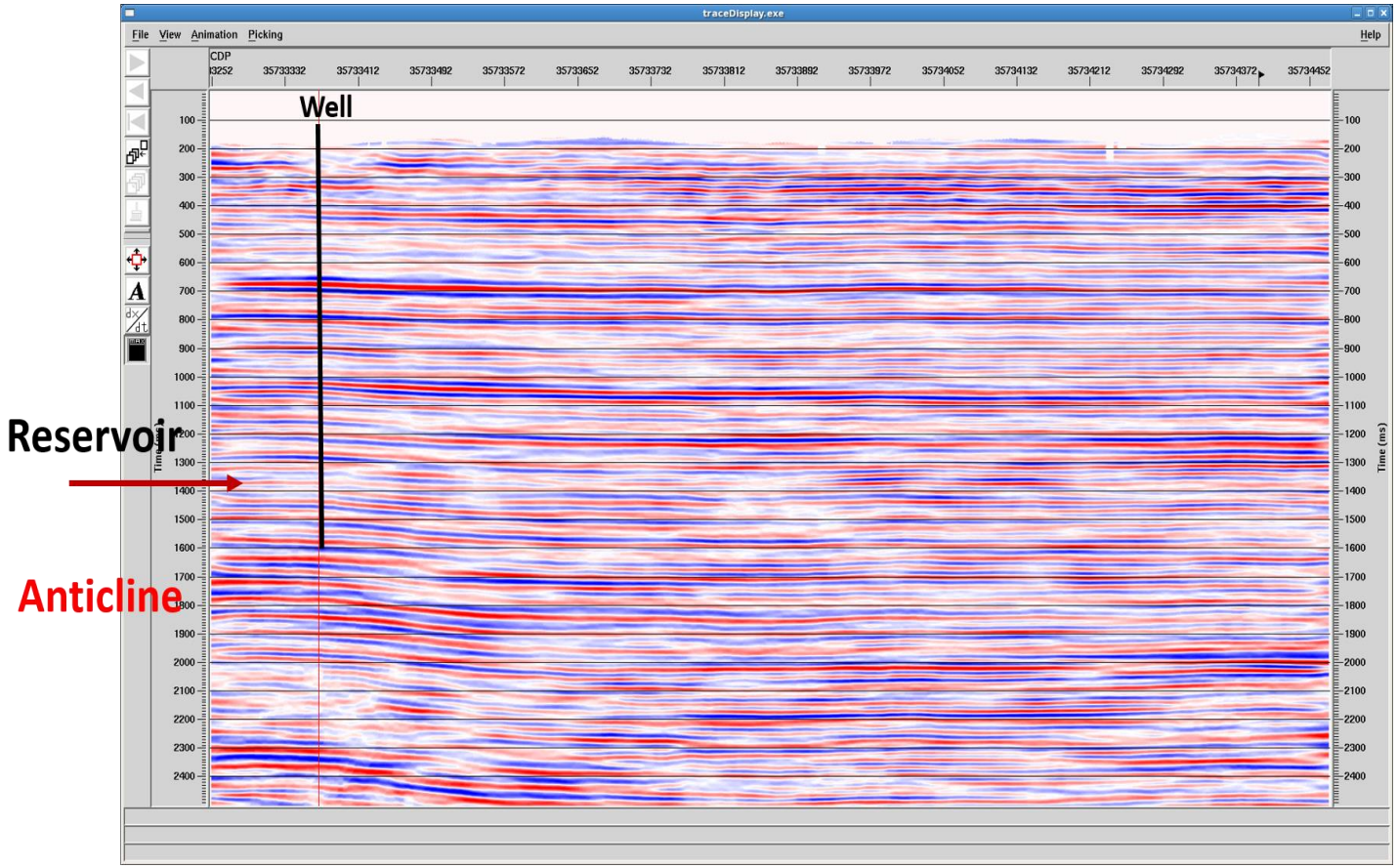

Figure IV-30: P stacked seismic section generated by initial processing data of the pressure component

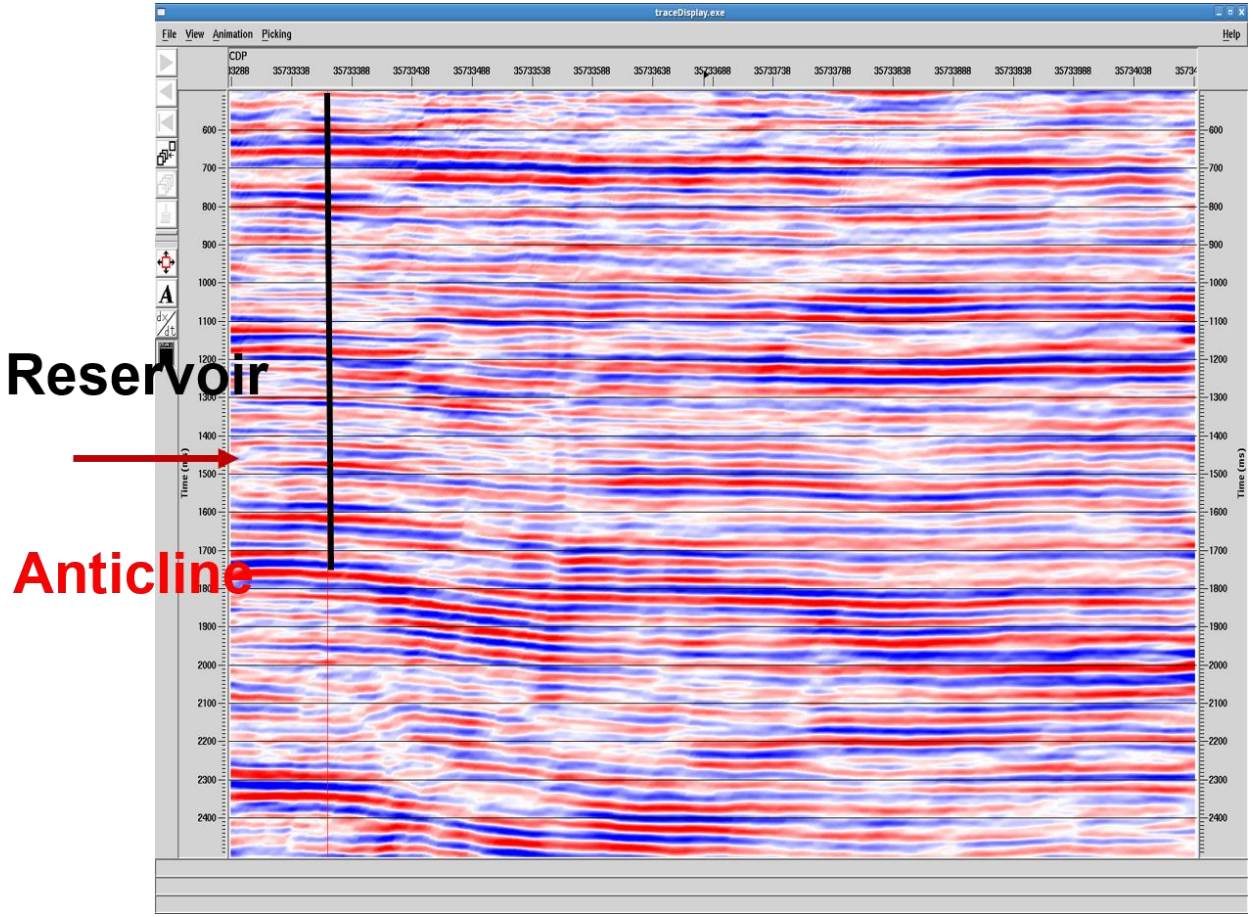

Figure IV-31: P stacked seismic section generated by initial processing data of the vertical component

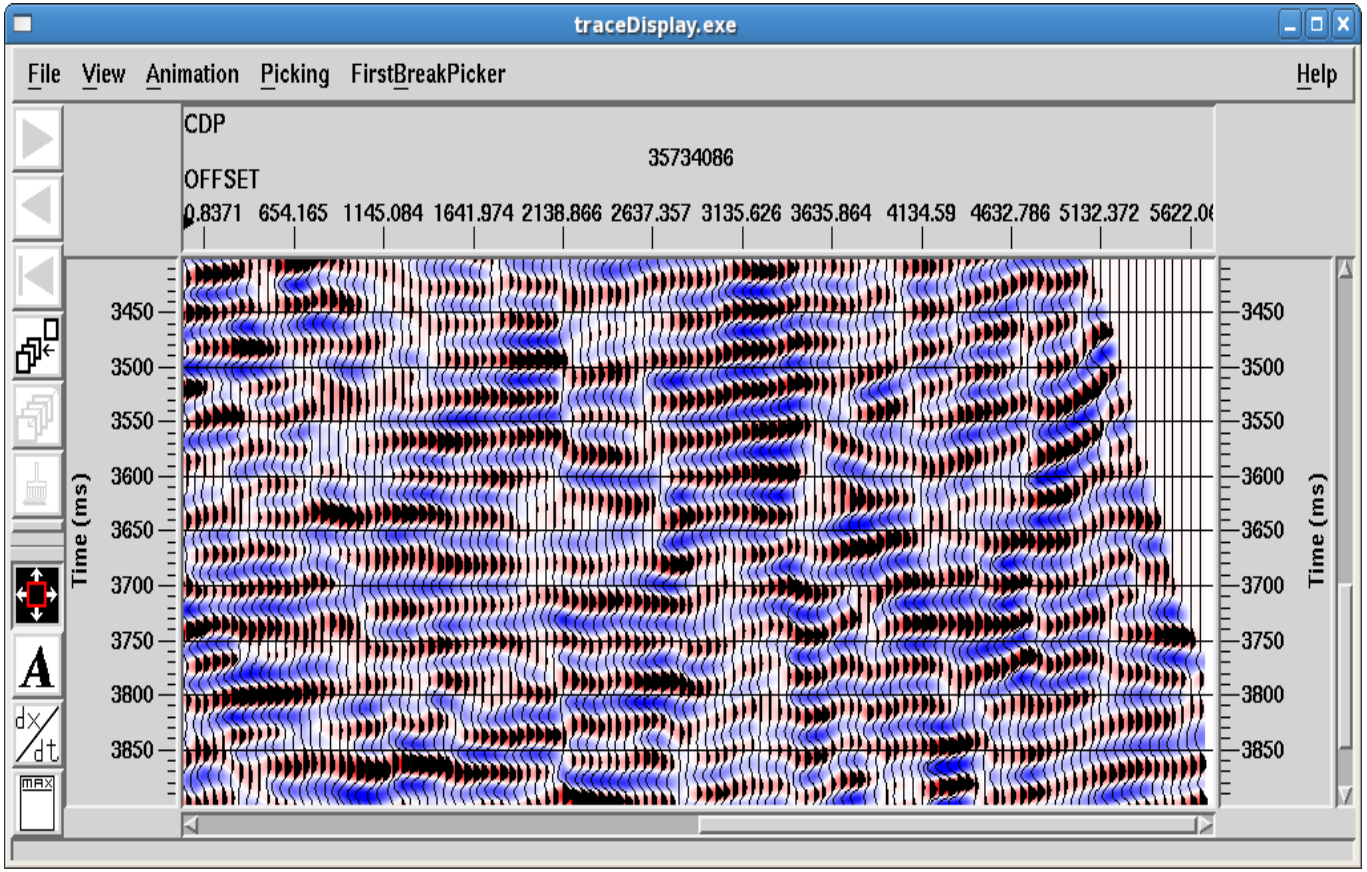

Figure IV-32: Enlarged part of the inline component at the reservoir zone (t=3400ms – 3900ms) after the NMO correction.

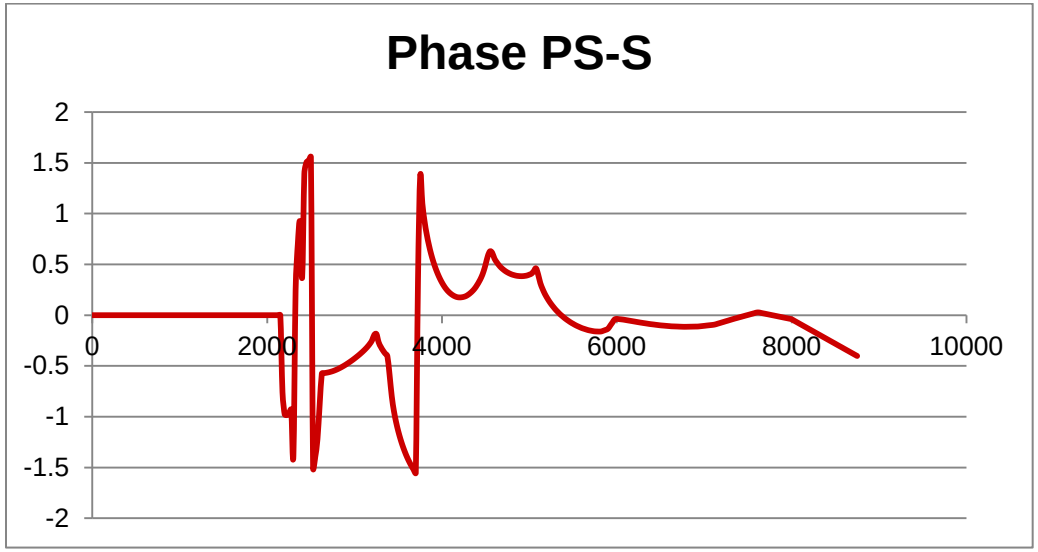

Figure IV-33: Zoeppritz modelling of PSS waves on phase changes with offset (Berteussen, 2014).

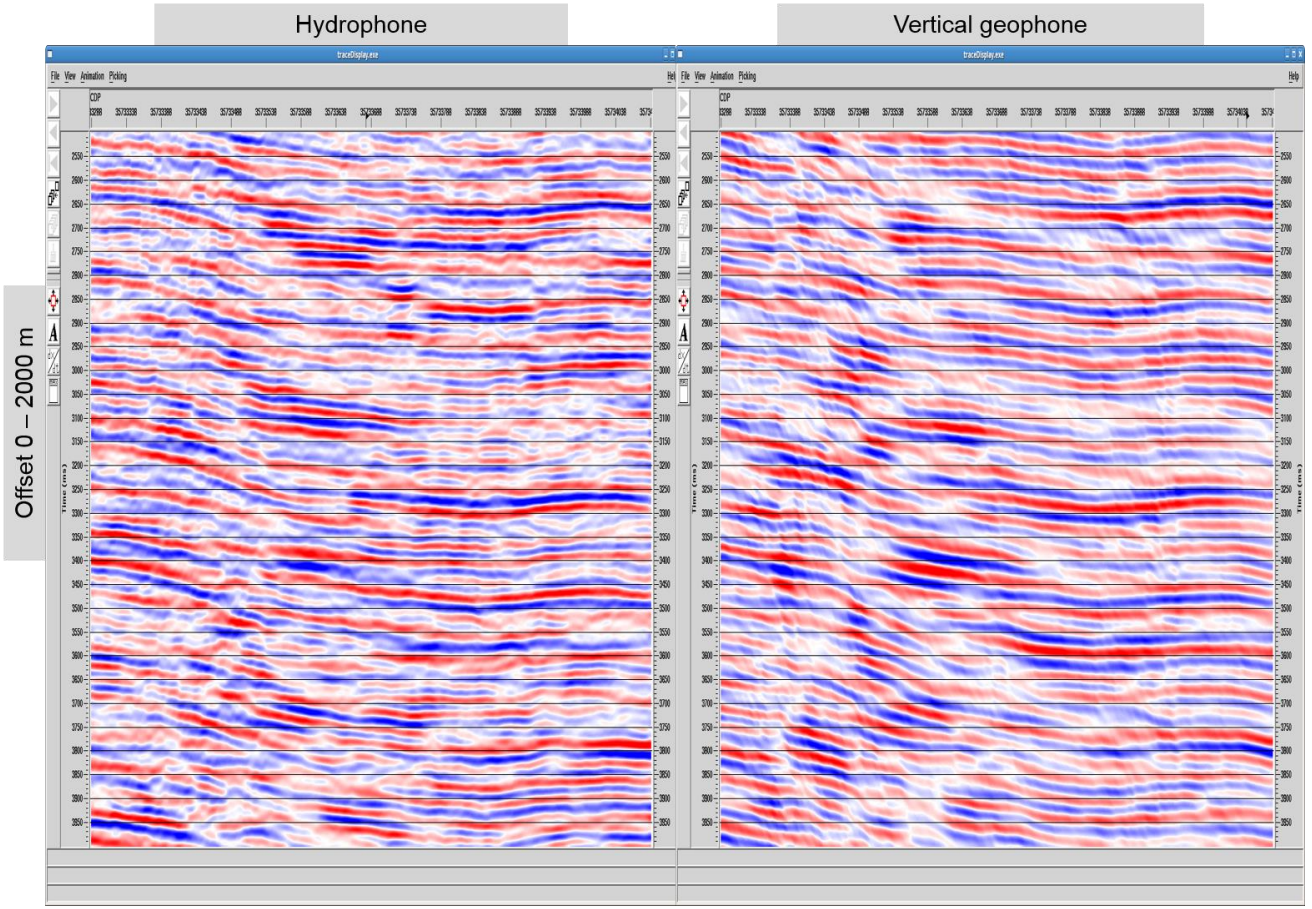

Figure IV-34: Portion of S stacked sections using near offset gather (0-2000m) with stacking velocity based on shear wave log in time zone t =2500ms-4000ms. a) Hydrophone. b) Vertical geophone.

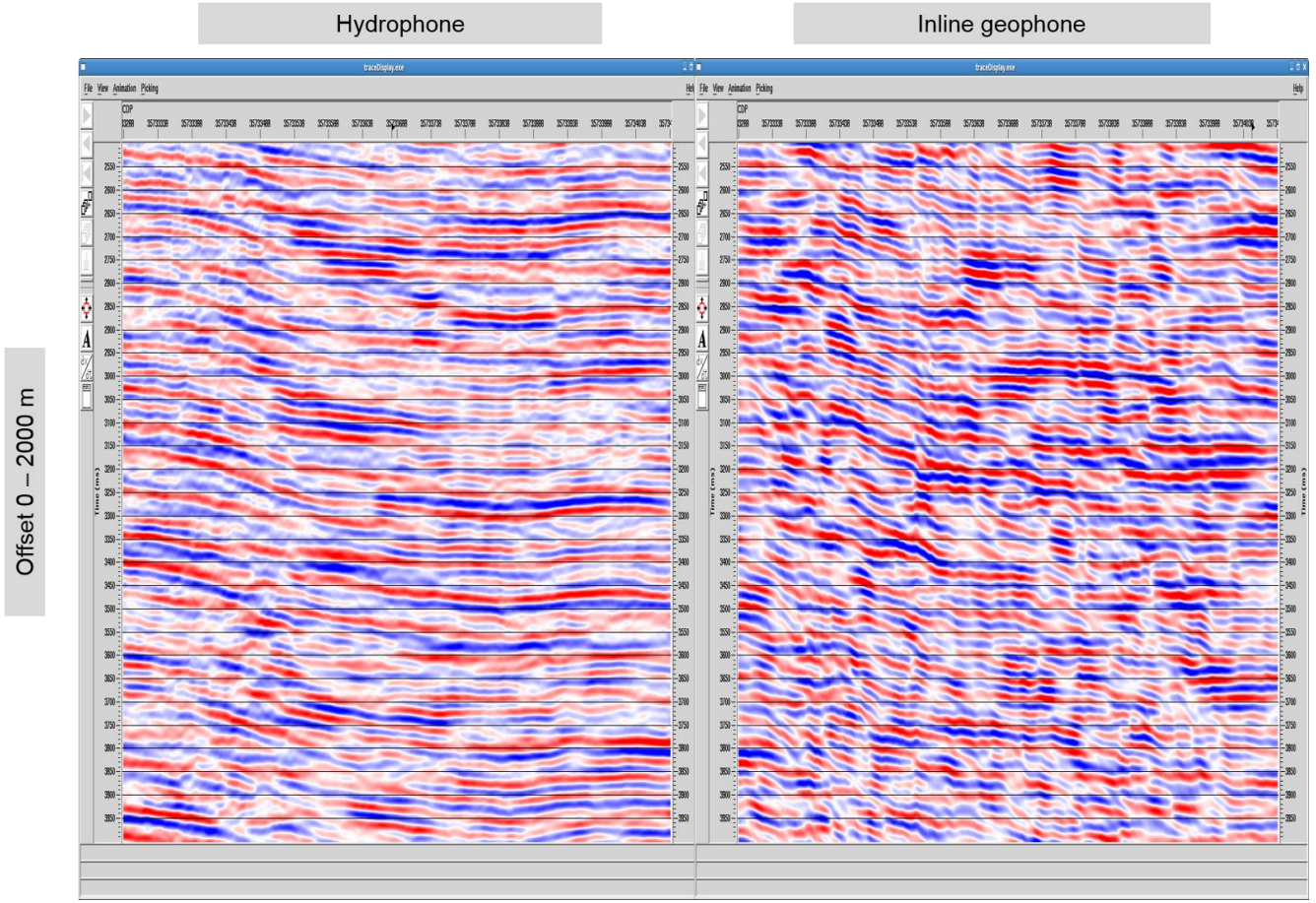

Figure IV-35: Portion of S stacked sections using near offset gather (0-2000m) with stacking velocity based on shear wave log in time zone t =2500ms-4000ms. a) Hydrophone. b) Inline geophone (color).

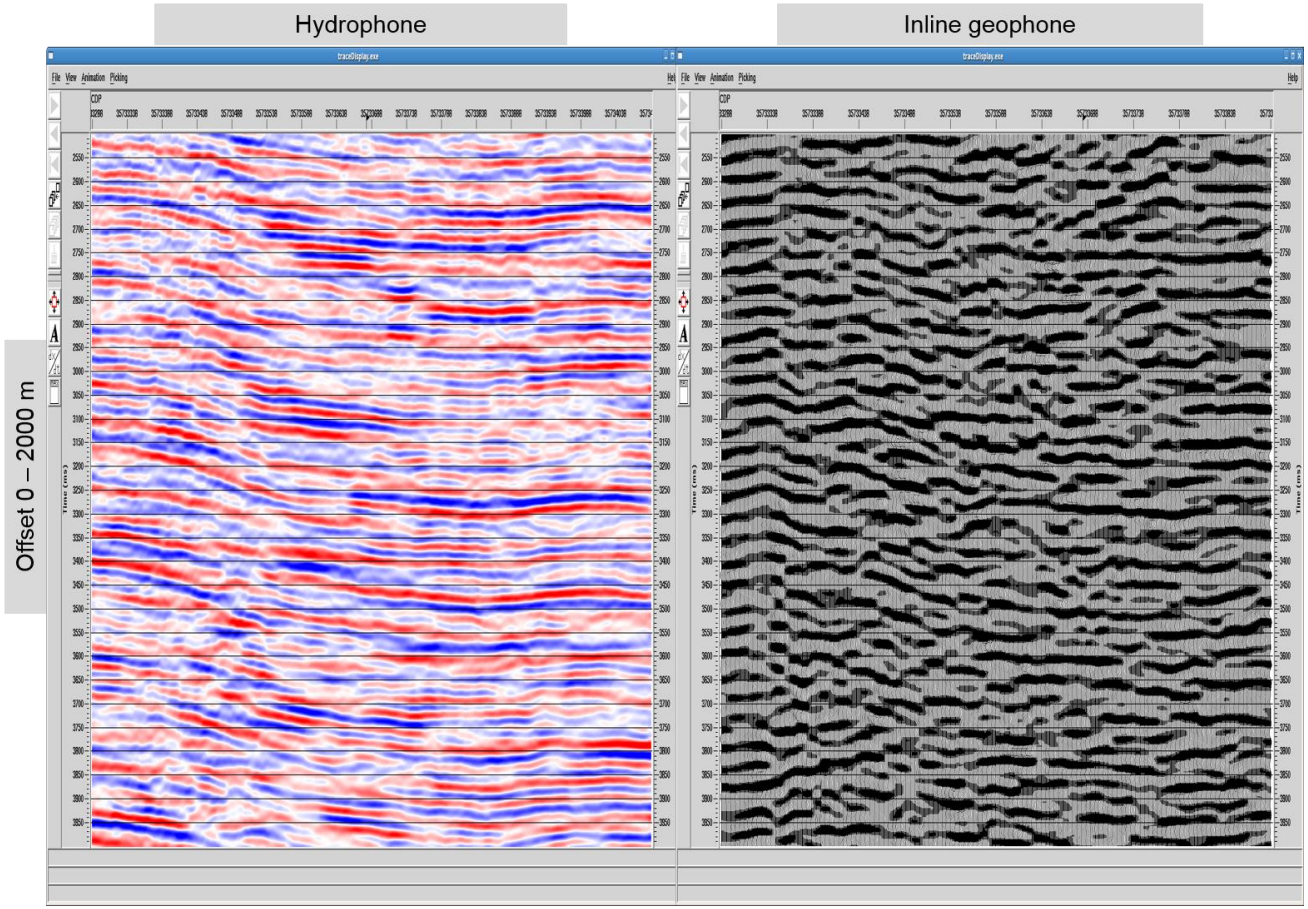

Figure IV-36: Portion of S stacked sections using near offset gather (0-2000m) with stacking velocity based on shear wave log in time zone t =2500ms-4000ms. a) Hydrophone. b) Inline geophone (black).

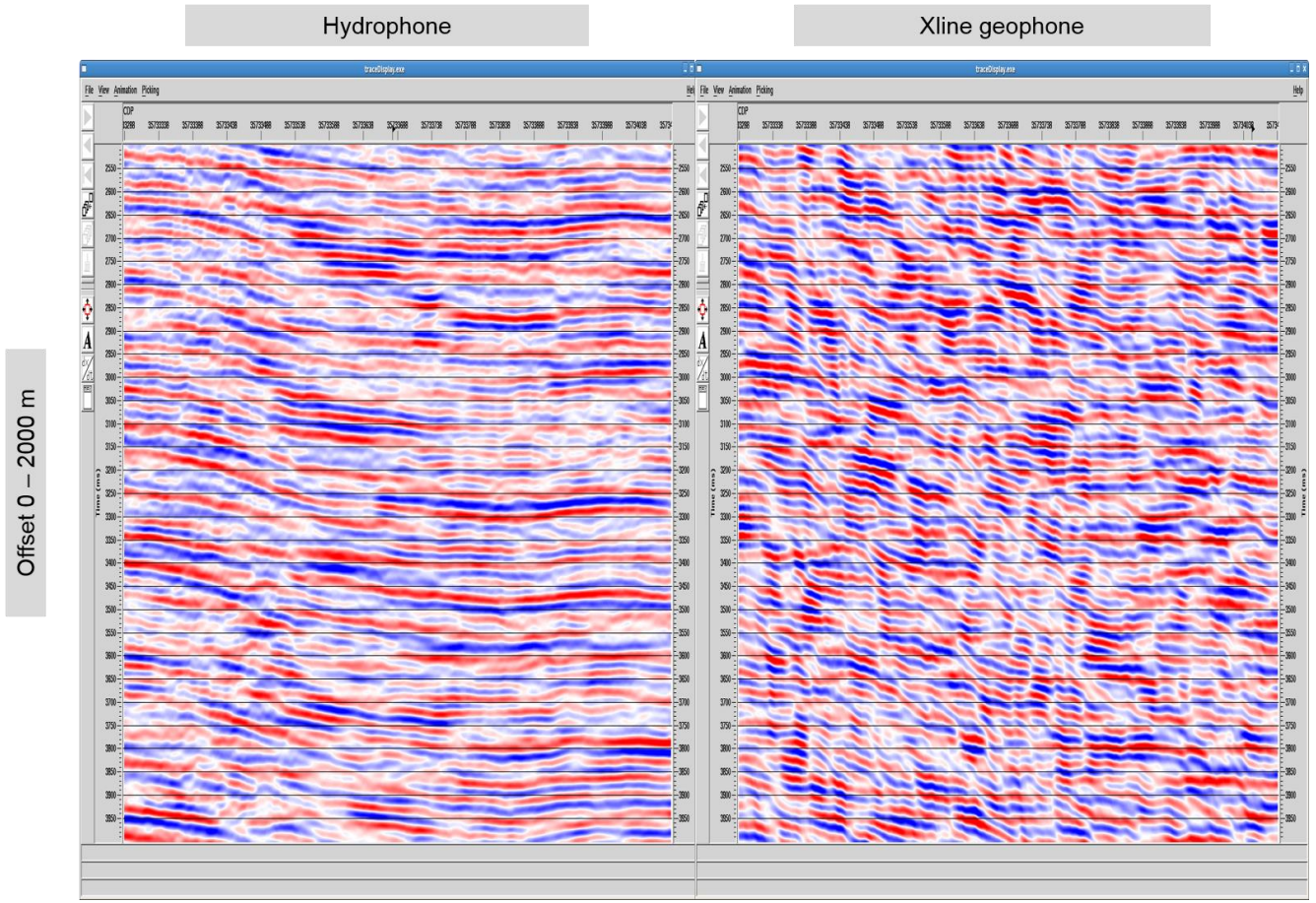

Figure IV-37: Portion of S stacked sections using near offset gather (0-2000m) with stacking velocity based on shear wave log in time zone t =2500ms-4000ms. a) Hydrophone. b) Xline geophone (color).

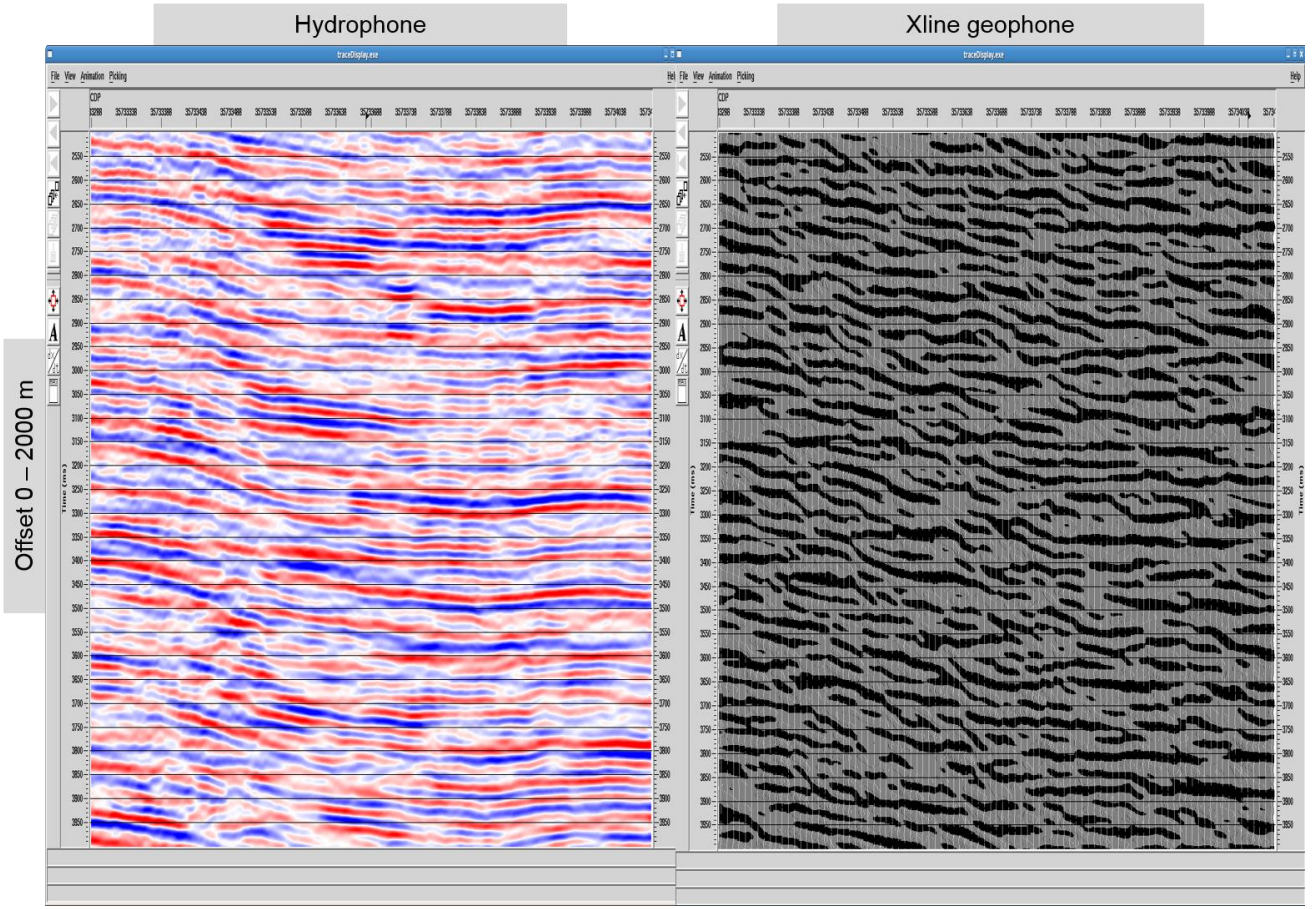

Figure IV-38: Portion of S stacked sections using near offset gather (0-2000m) with stacking velocity based on shear wave log in time zone t =2500ms-4000ms. a) Hydrophone. b) Xline geophone (black).

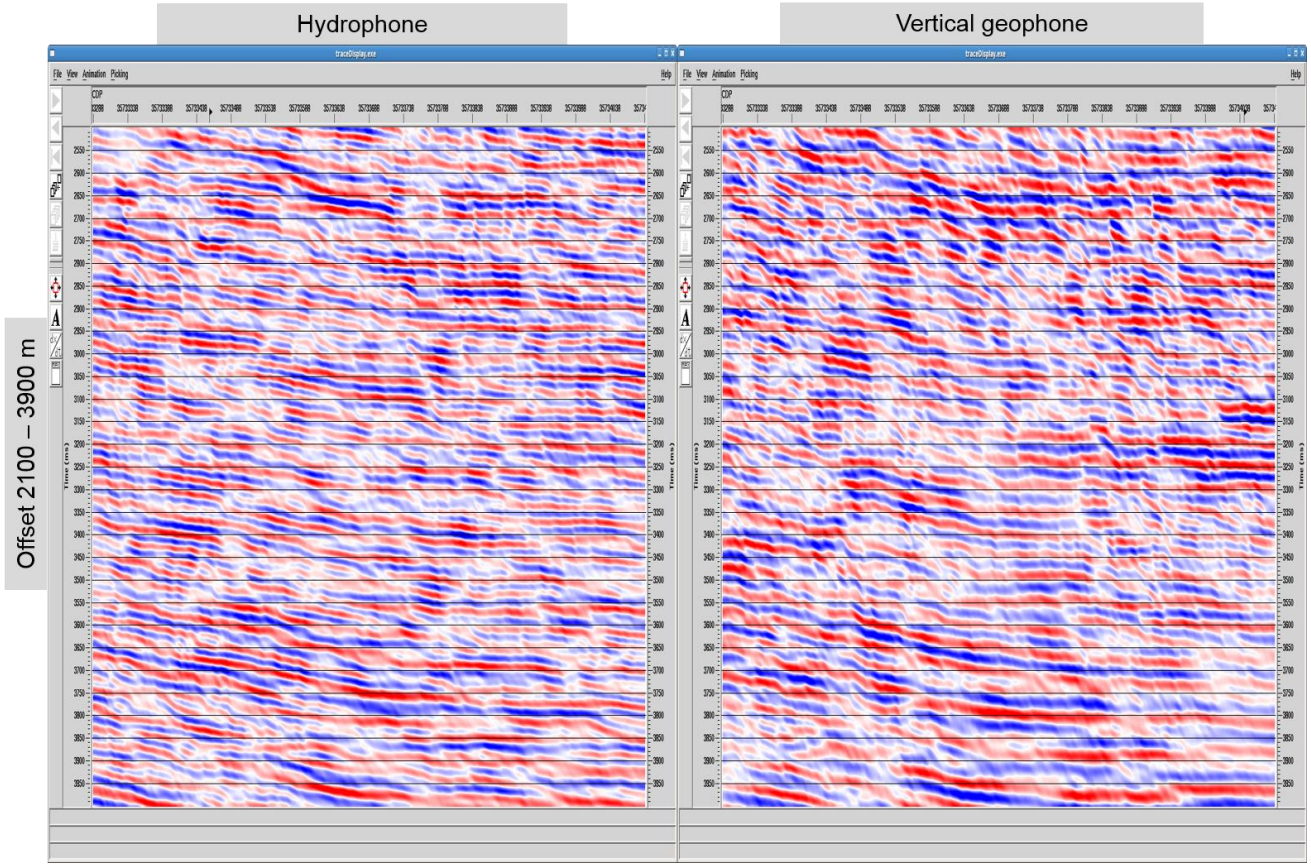

Figure IV-39: Portion of S stacked sections using middle offset gather (2100-3900m) with stacking velocity based on shear wave log in time zone t =2500ms-4000ms. a) Hydrophone. b) Vertical geophone.

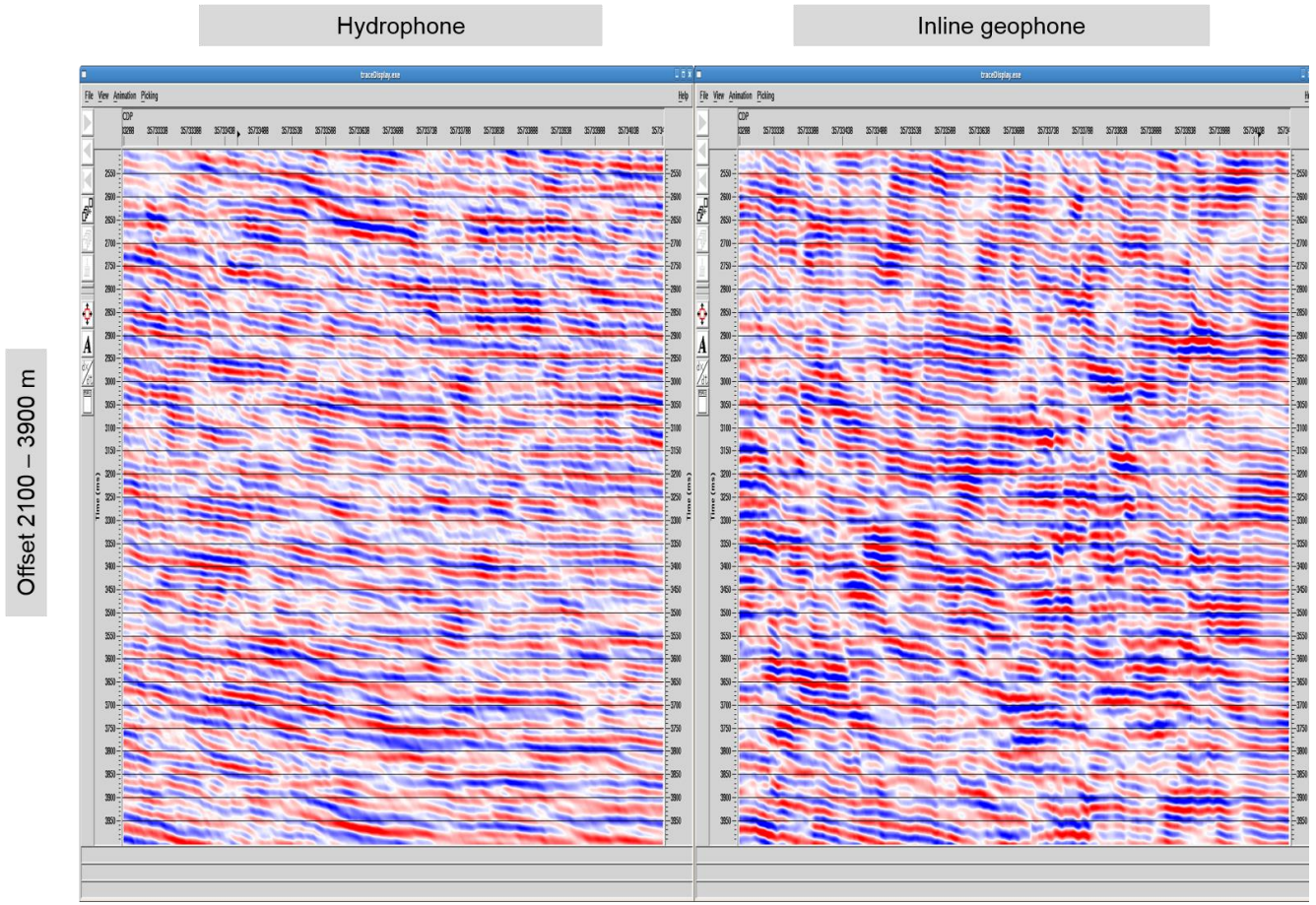

Figure IV-40: Portion of S stacked sections using middle offset gather (2100-3900m) with stacking velocity based on shear wave log in time zone t =2500ms-4000ms. a) Hydrophone. b) Inline geophone (color).

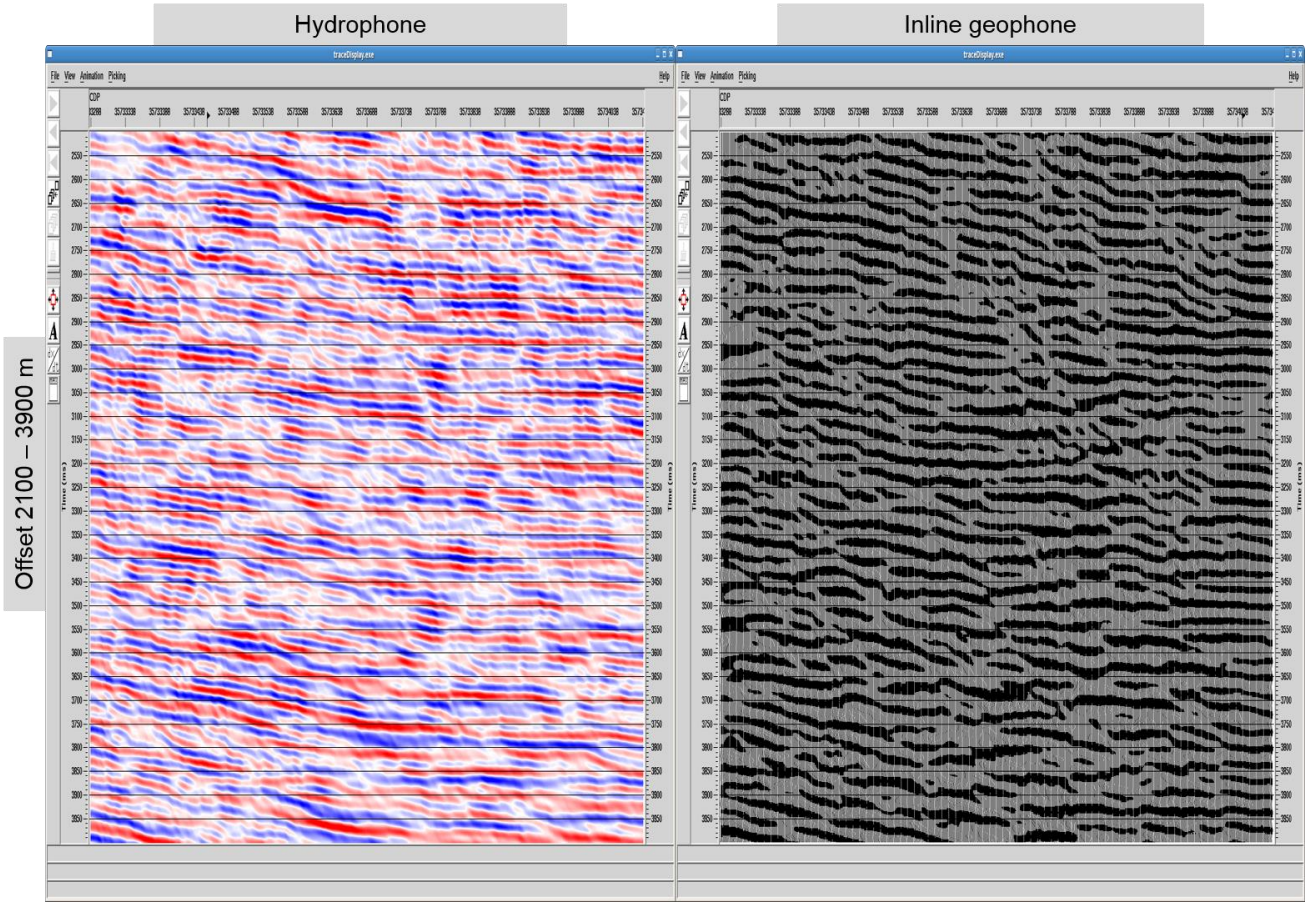

Figure IV-41: Portion of S stacked sections using middle offset gather (2100-3900m) with stacking velocity based on shear wave log in time zone t =2500ms-4000ms. a) Hydrophone. b) Inline geophone (black).

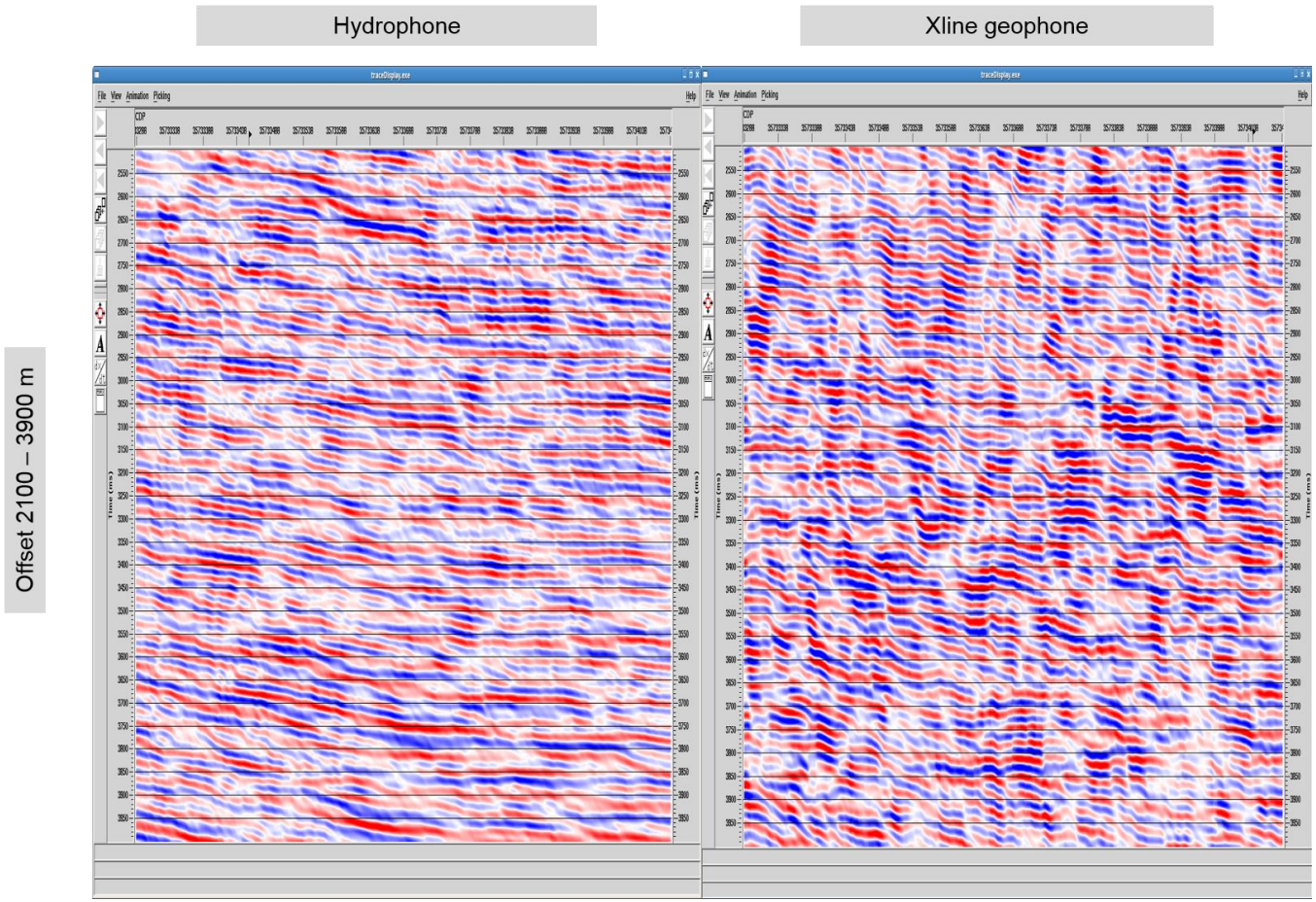

Figure IV-42: Portion of S stacked sections using middle offset gather (2100-3900m) with stacking velocity based on shear wave log in time zone t =2500ms-4000ms. a) Hydrophone. b) Xline geophone (color).

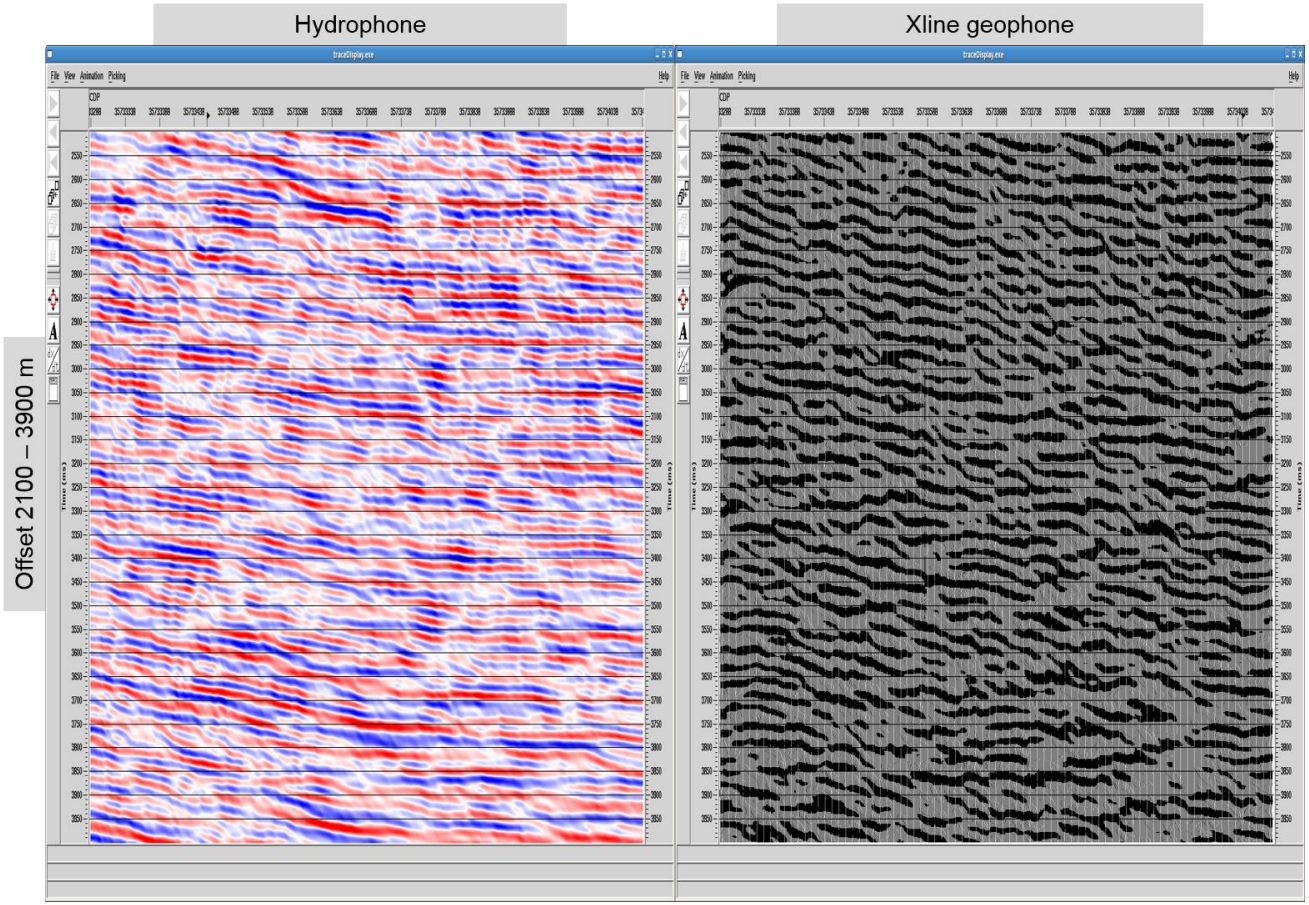

Figure IV-43: Portion of S stacked sections using middle offset gather (2100-3900m) with stacking velocity based on shear wave log in time zone t =2500ms-4000ms. a) Hydrophone. b) Xline geophone (black).

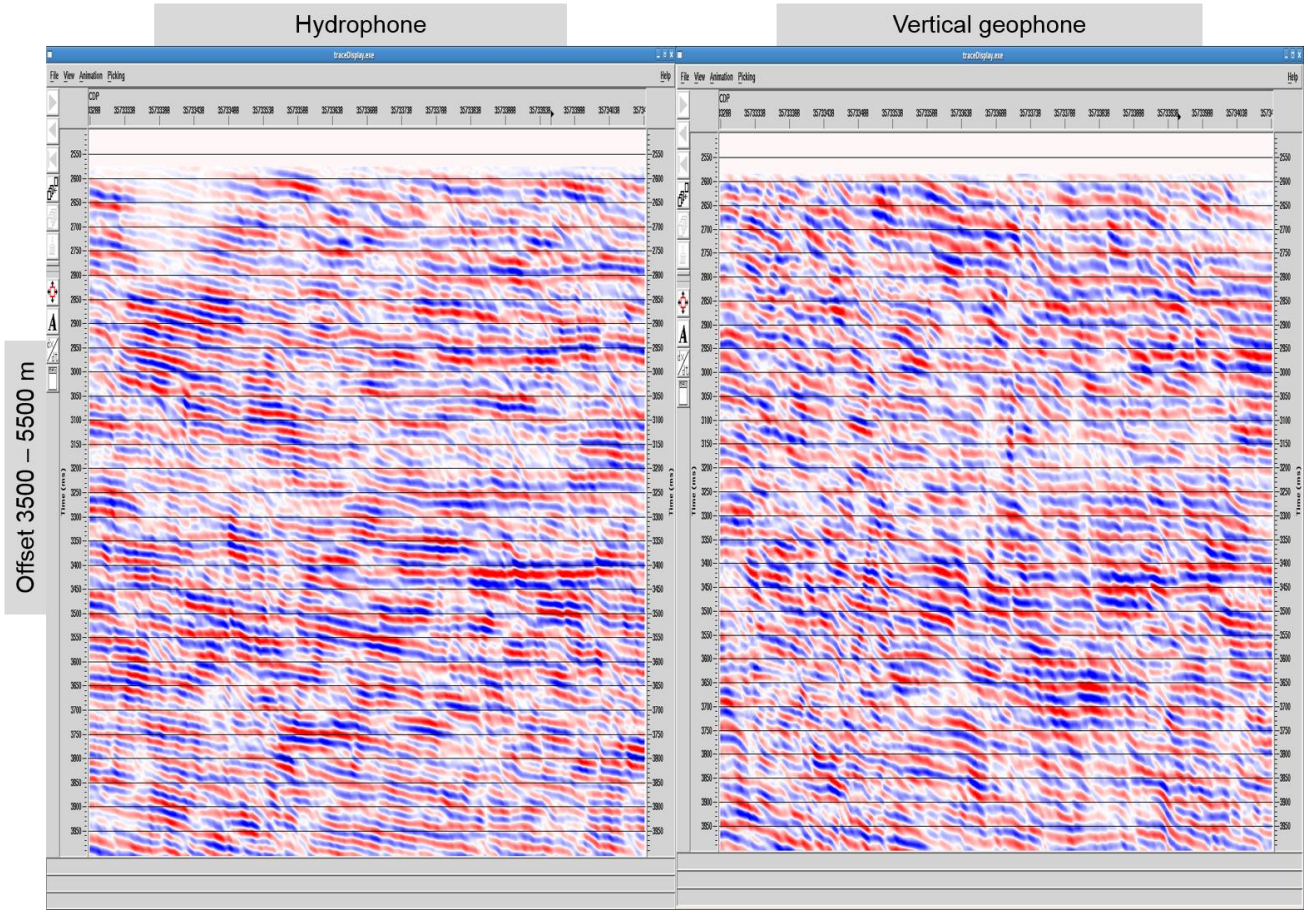

Figure IV-44: Portion of S stacked sections using far offset gather (3500-5500m) with stacking velocity based on shear wave log in time zone t =2500ms-4000ms. a) Hydrophone. b) Vertical geophone.

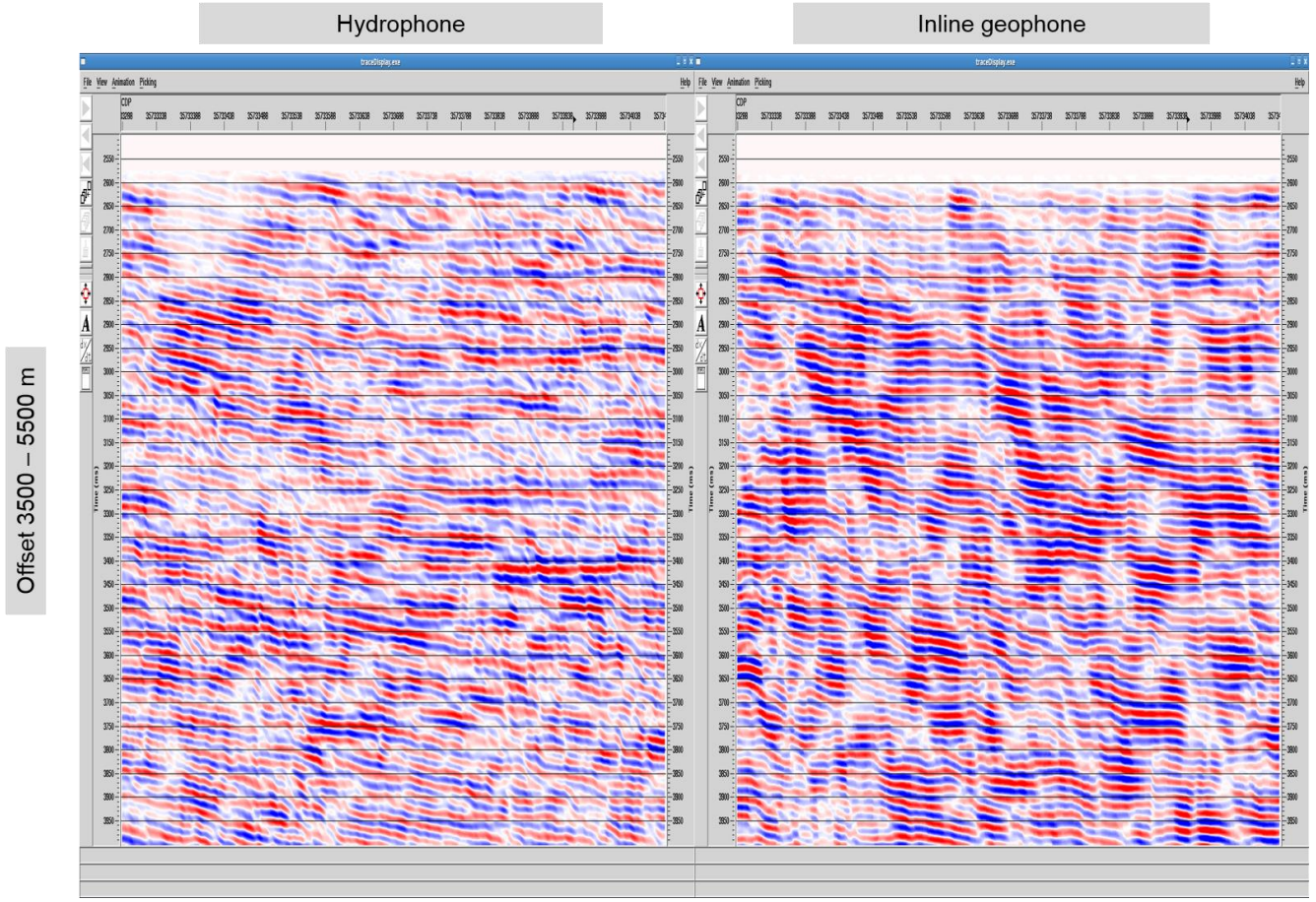

Figure IV-45: Portion of S stacked sections using far offset gather (3500-5500m) with stacking velocity based on shear wave log in time zone t =2500ms-4000ms. a) Hydrophone. b) Inline geophone (color).

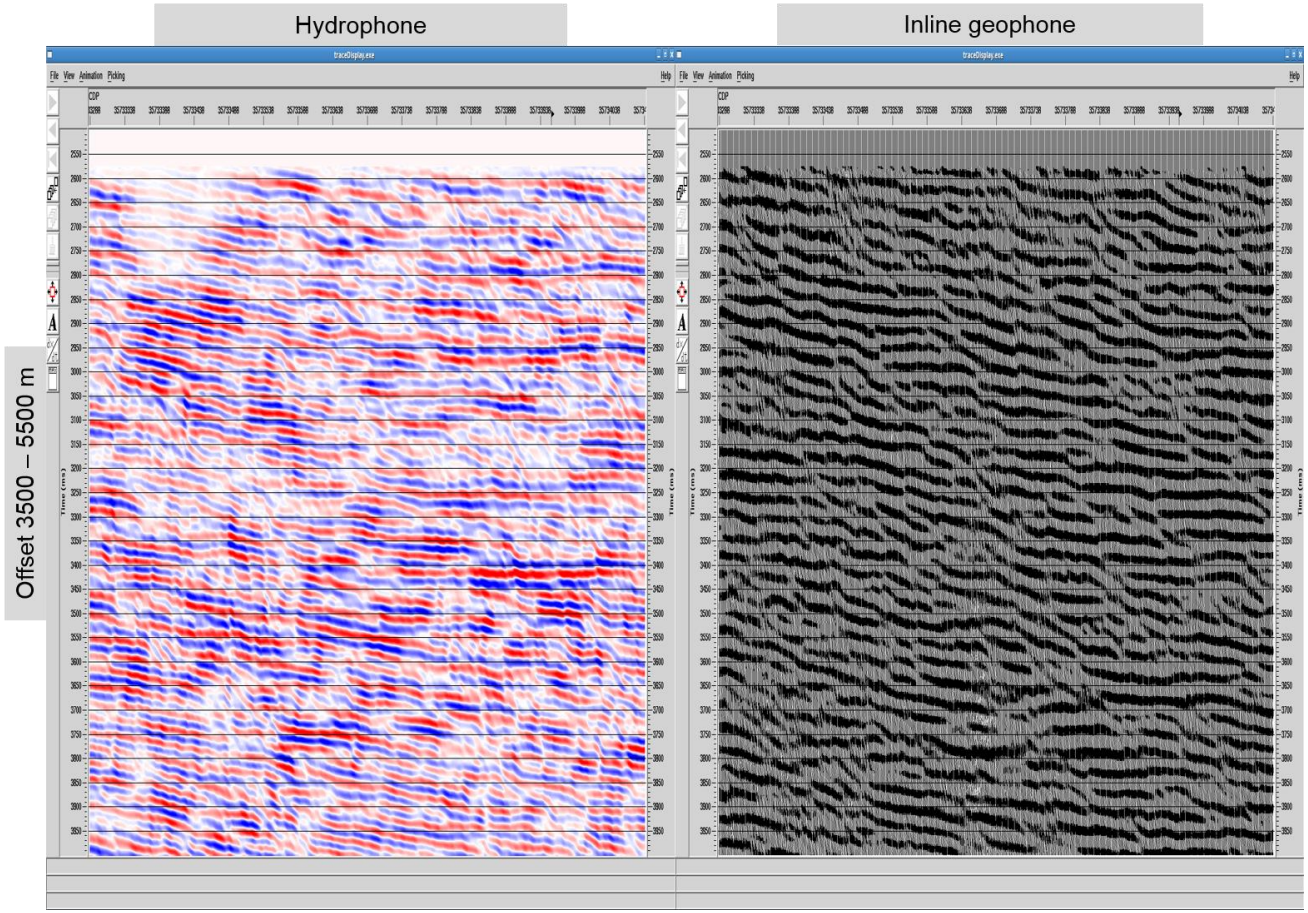

Figure IV-46: Portion of S stacked sections using far offset gather (3500-5500m) with stacking velocity based on shear wave log in time zone t =2500ms-4000ms. a) Hydrophone. b) Inline geophone (black).

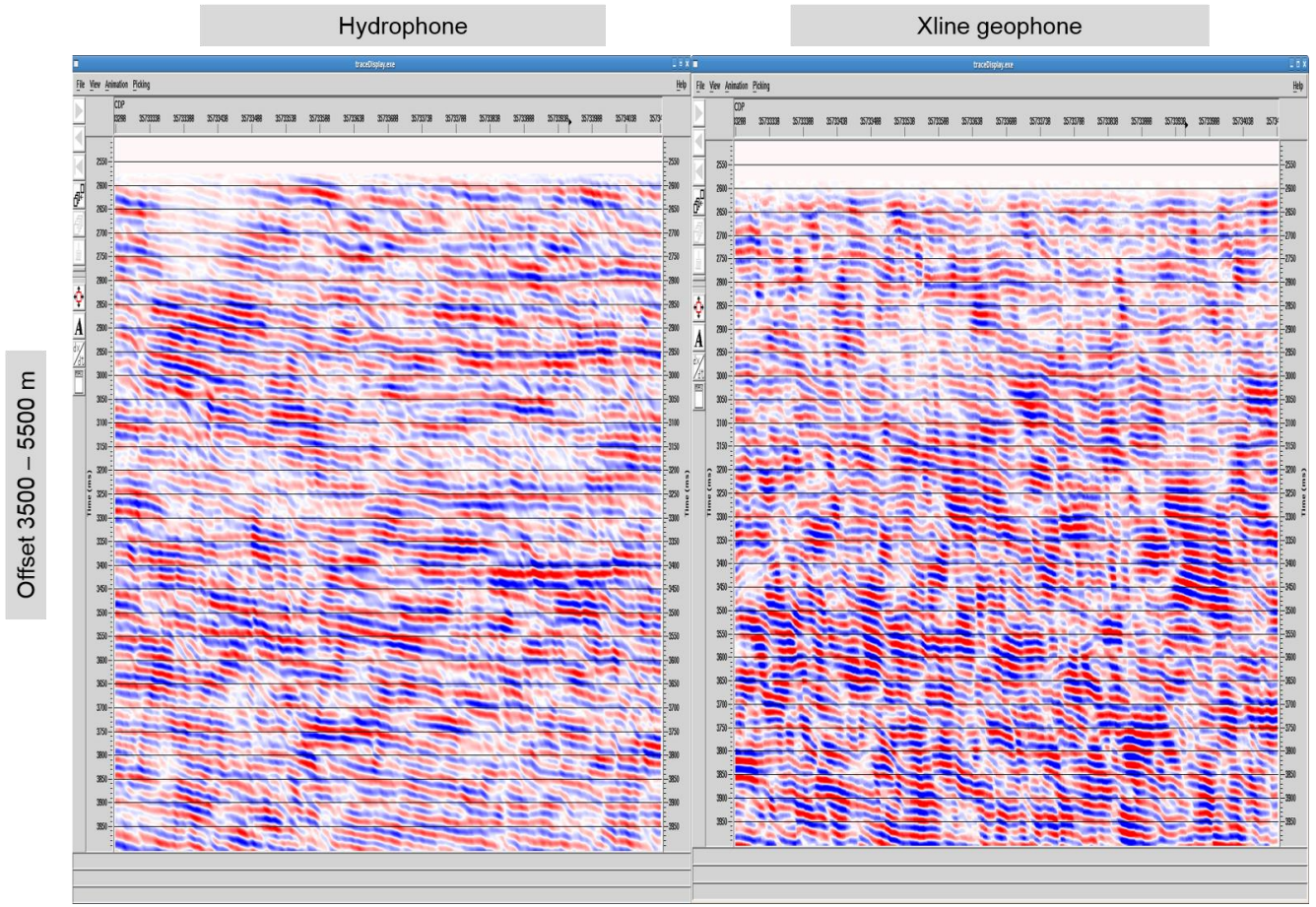

Figure IV-47: Portion of S stacked sections using far offset gather (3500-5500m) with stacking velocity based on shear wave log in time zone t =2500ms-4000ms. a) Hydrophone. b) Xline geophone (color).

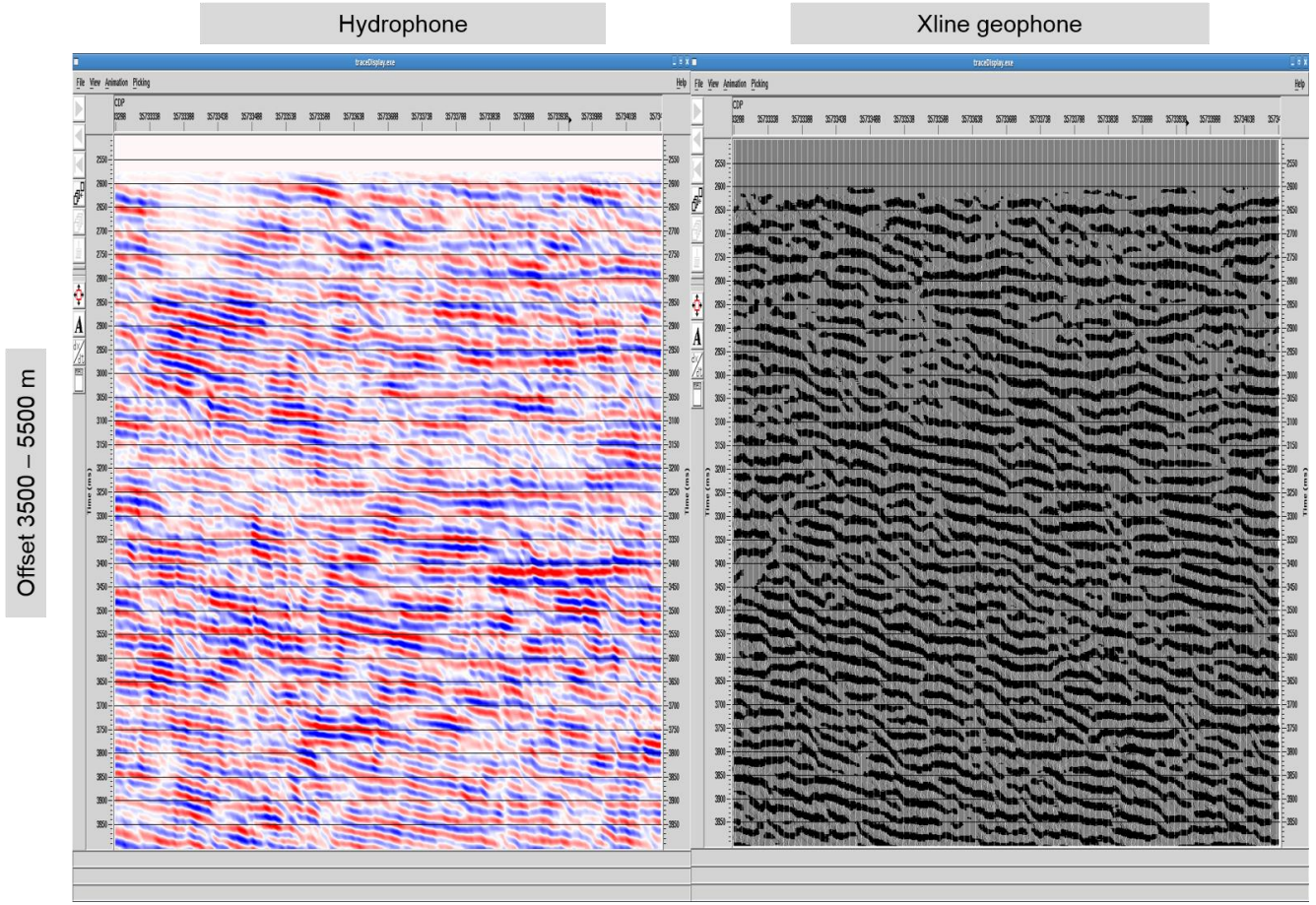

Figure IV-48: Portion of S stacked sections using far offset gather (3500-5500m) with stacking velocity based on shear wave log in time zone t =2500ms-4000ms. a) Hydrophone. b) Xline geophone (black).

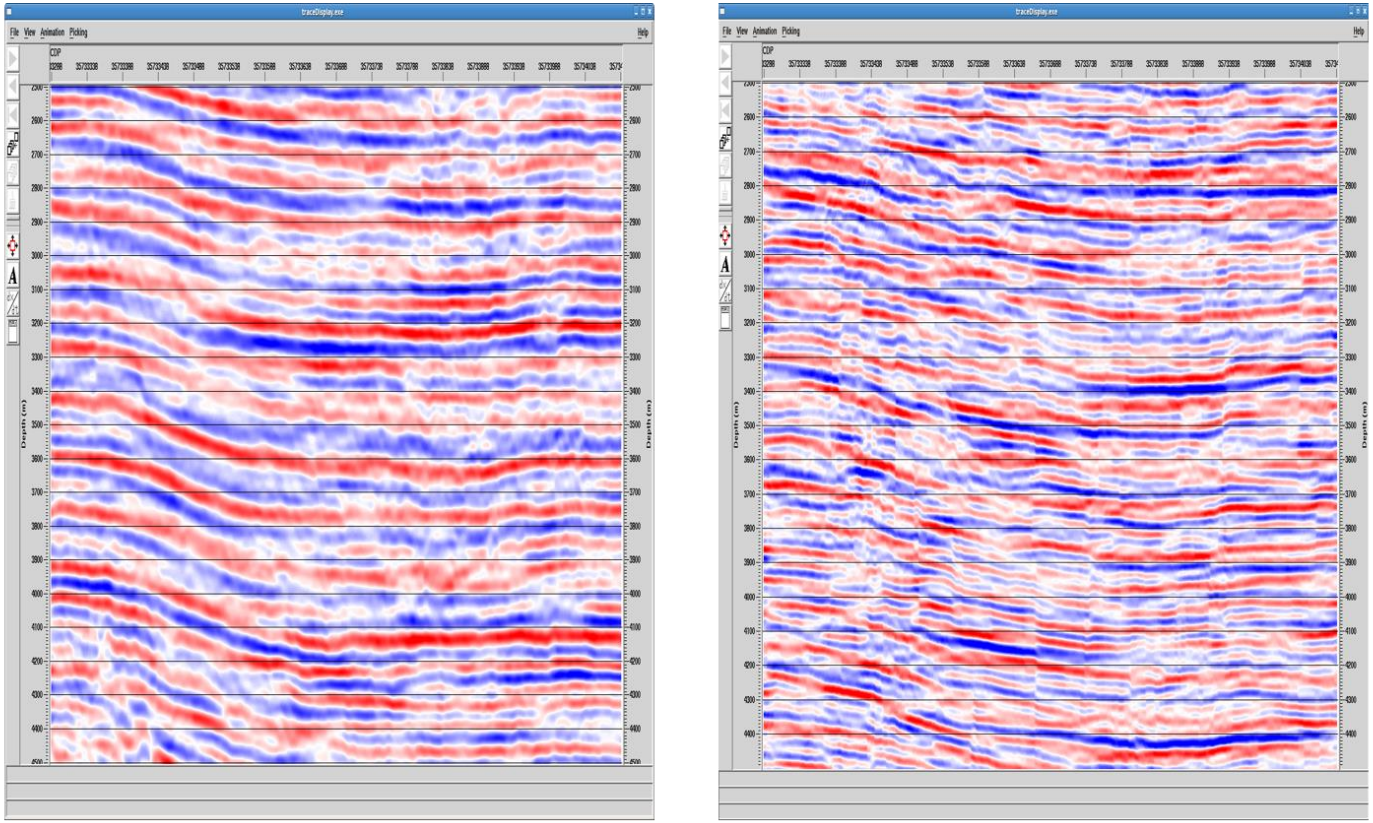

Figure IV-49: a) The P velocity stacked section in depth of the pressure component. 2) The S velocity stacked section in depth of the pressure component.

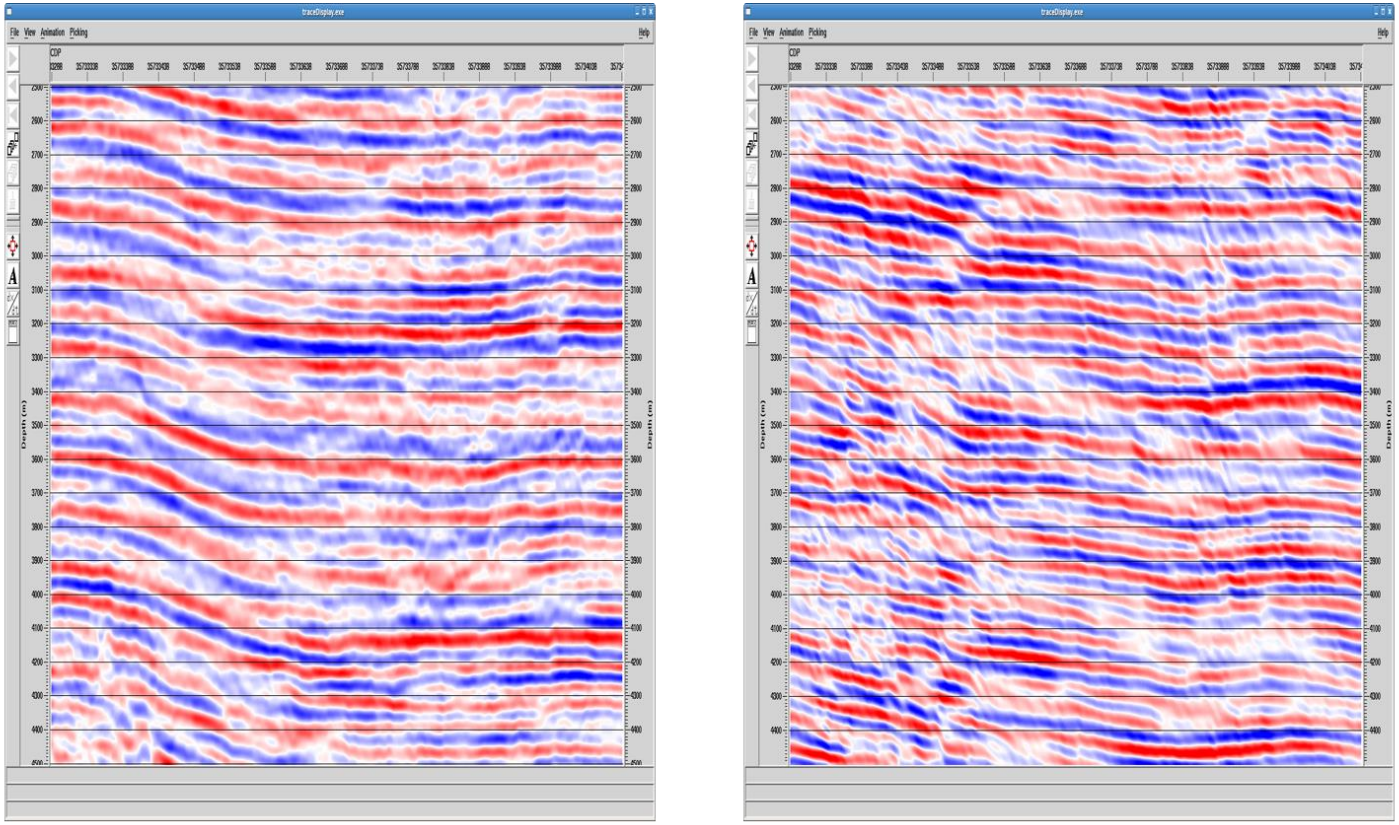

Figure IV-50: a) The P velocity stacked section in depth of the pressure component. 2) The S velocity stacked section in depth of the vertical component.

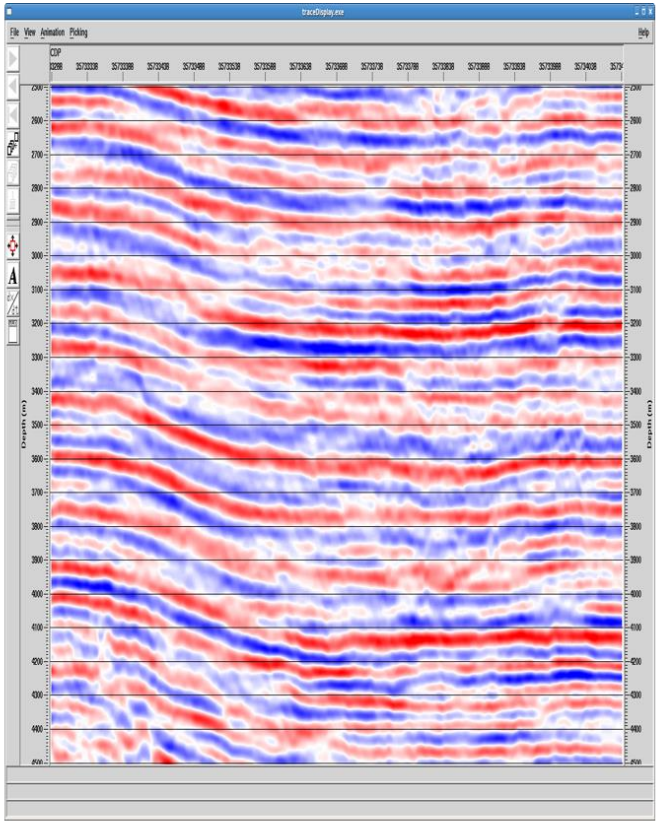

P velocity stacking in pressure component

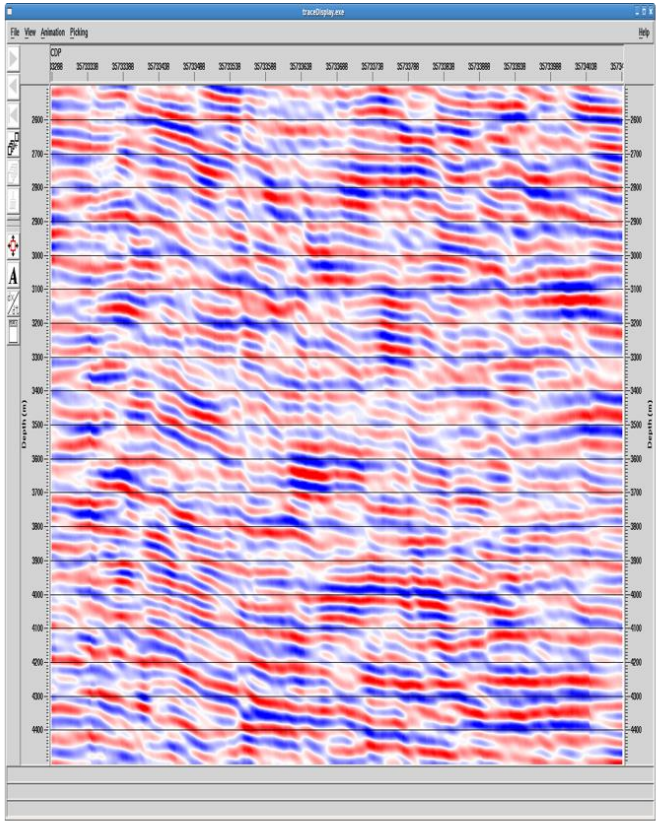

S velocity stacking in inline component

Figure IV-51: a) The P velocity stacked section in depth of the pressure component. 2) The S velocity stacked section in depth of the inline component (color).

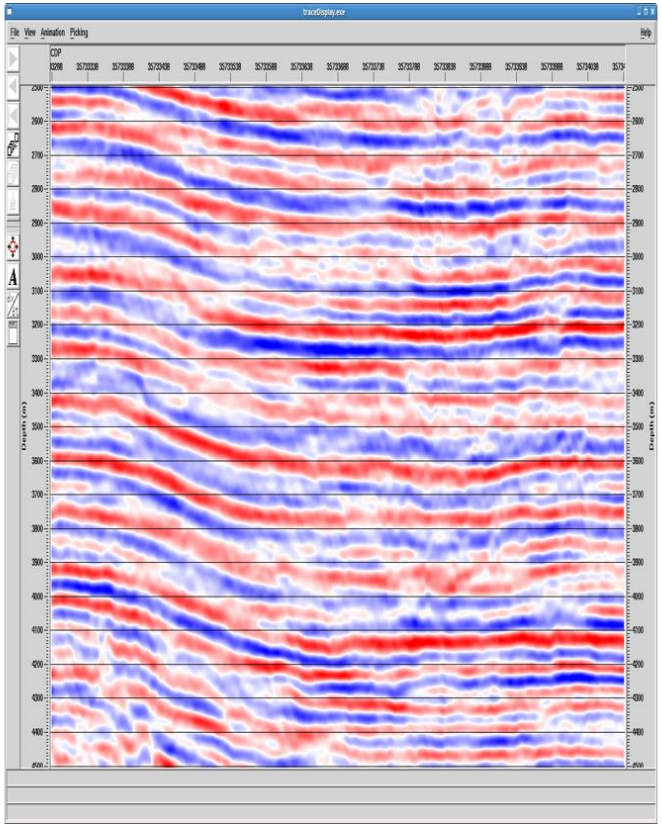

P velocity stacking in pressure component

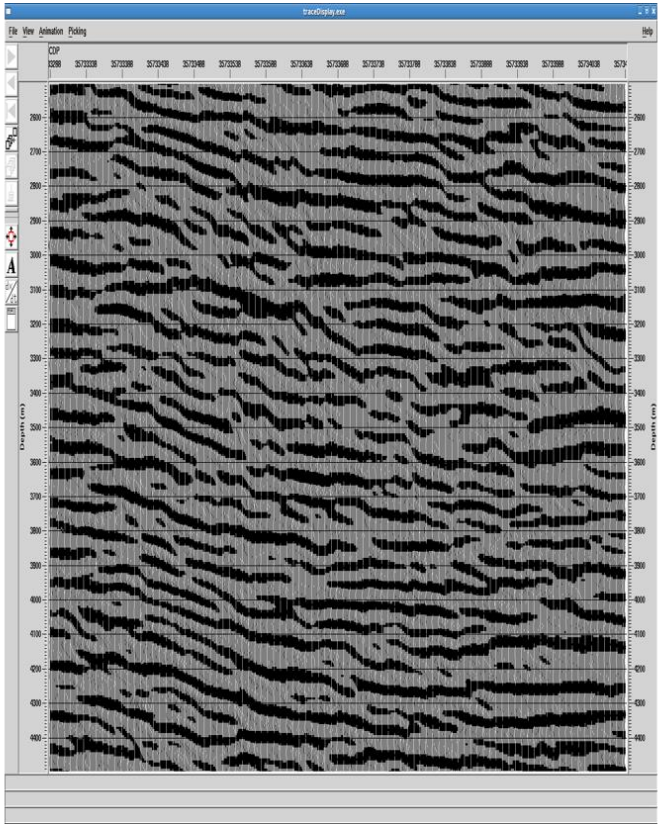

S velocity stacking in inline component

Figure IV-52: a) The P velocity stacked section in depth of the pressure component. 2) The S velocity stacked section in depth of the inline component (black).

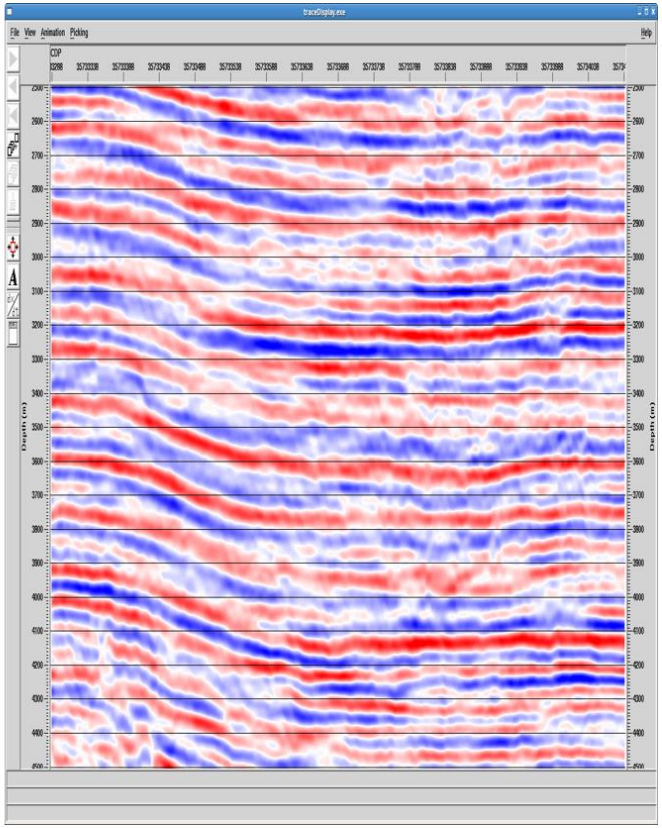

P velocity stacking in pressure component

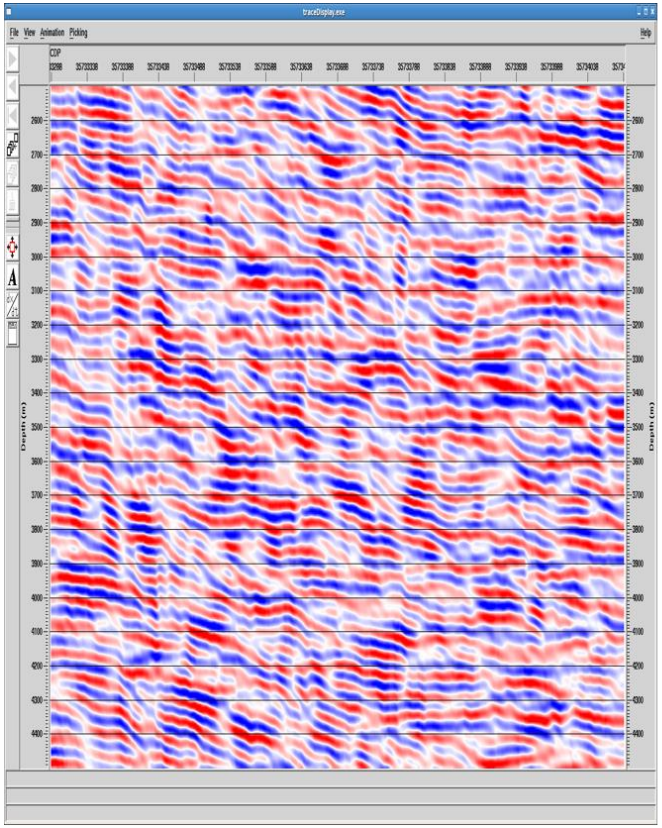

S velocity stacking in xline component

Figure IV-53: a) The P velocity stacked section in depth of the pressure component. 2) The S velocity stacked section in depth of the crossline component (color).

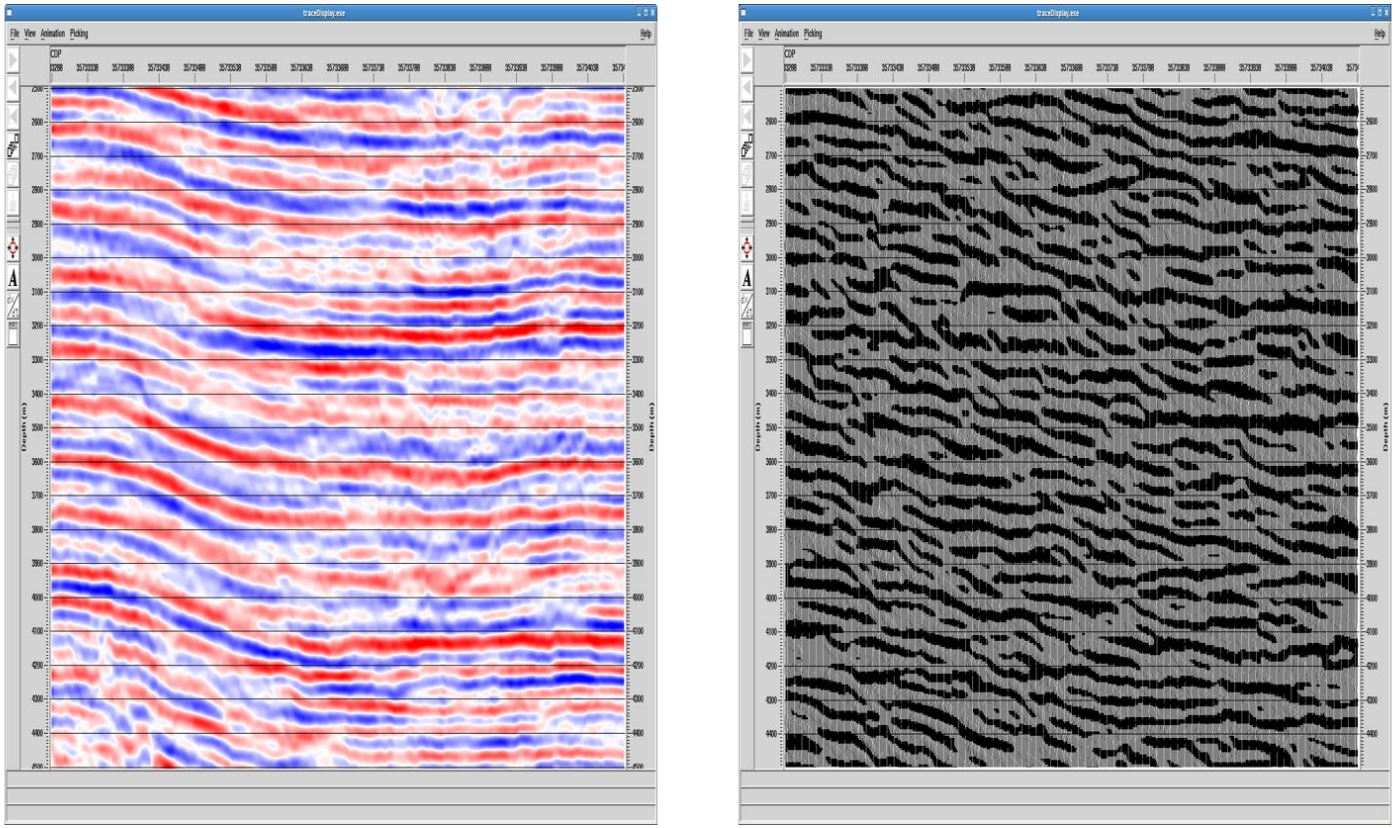

Figure IV-54: a) The P velocity stacked section in depth of the pressure component. 2) The S velocity stacked section in depth of the crossline component (black).

4.6. Conclusion

The harsh acquisition environment of the shallow marine Arabian Gulf results in heavily dispersive surface waves, which challenges the current processing methodology and limits the potential benefit of 4C OBC data, but also leads to new opportunity for shear wave exploration. This chapter discussed the preconditioning of the data before and after the stacking to enhance the S/N by eliminating the various noises in different domains and discovered the improvement it brought in delineating the subsurface structure and estimating rock properties using both P and S waves.

Modeling results indicated the existence of strong PSS waves when vertical velocities change rapidly. It also verified that the shear waves undergo phase changes in the post-critical angle zone. Conventional processing procedure cannot utilize these unique propagation properties of the PSS wave in the shallow water environment with a hard sea bottom. One 4C OBC 2D seismic line from offshore U.A.E. was studied for the 4C processing workflow design with the purpose to obtain the subsurface structure section.

Using velocity information from a nearby well and the modeling result, the proposed 4C processing procedure implemented various filtering algorithms, the special converted velocity analysis and the model based partial stacking. P wave velocity structure was generated using both P and Z components. Horizontal components are used for S wave detection. The extracted PSS events are relatively clear on the inline components. Though mixed with residual noises, the processed crossline component also

shows those events, which can be the SH waves. We illustrated one potential comprehensive structural interpretation on depth by using both P and S waves.

In summary, 4C seismic data hold a great promise for an increased seismic resolution, better detection of bypassed hydrocarbons and better mapping of permeability heterogeneity if shear wave information can be successfully extracted from the 4C seismic data. However, the shear source has been expensive and not easily applicable in the marine environment, and the conventional PS converted wave processing is complicated and unreliable. The innovative findings of PSS converted waves provide a way to fully utilize the OBC data. The processing methodology outlined here could be applied as a general workflow to enhance the data quality and obtain the P/S images from the 4C OBC data in the shallow marine Arabian Gulf.

CHAPTER V

CONCLUSION

The 4C OBC surveying has the advantage over towed streamer surveys since the two horizontal components provide the opportunity to extend shear waves studies to offshore fields, especially the technology on the shear wave mode. Currently, most marine 4C applications are implemented to acquire the P-SV converted waves, with a P-wave source. The shallow OBC acquisition provides the unique opportunity to study the fundamental S waves (SH-SH and SV-SV), since an illuminating SV wave-field is generated with the P waves due to the hard sea bottom at the source station.

Acquiring high quality 4C OBC data is considerably more difficult than the conventional seismic data, especially in shallow marine applications, because it requires that receivers are in good contact with the ground and line in consistent direction to accurately measure ground motion. Various signal enhancement algorithms have been performed on single sensor with success, in both time and frequency domain, but not applicable or ineffective on the 4C OBC data. We summarized the major challenges for OBC data processing in the Arabian Gulf: 1) Highly dispersive Scholte waves due to the shallow water depth and the hard sea bottom; 2) Poor vector fidelity of 3C geophone due to the coupling issues; 3) High velocity P related surface waves which mix with the reflected signals in the frequency spectrum. All of these make the wave-field complicated and challenge the conventional processing algorithm.

In order to address the above obstacles, we investigated the propagation properties of surface waves and designed the TFK transform using variable S transform to convert the signal from the time domain to the TFK domain. Considering surface waves' low frequency and low velocity properties, we implemented the TFK filtering to eliminate the surface waves in the FK domain at any specific time. Next, we recognized the value of polarization characteristics in the filtering design to correct the vector fidelity of 3C geophones. Three polarization properties were derived in the time-frequency-wavenumber domain. Combining the joined relationship of polarization, time, frequency and wavenumber, the TFK polarization filtering was implemented for eliminating the residual surface waves. After this two-step processing on one shot gather, TFK filtering and then TFK polarization analysis, reflected signals clearly showed up in the pressure and vertical components and the overall signal to noise ratio of horizontal components was improved. The displayed reflected layers in the horizontal components demonstrate the presence of the strong shear waves.

A generalize 4C OBC processing sequence was introduced for enhancing the signal quality and generating the P/S velocity section. To attenuate highly dispersive surface waves, various filtering methods are implemented in multi-domain based on surface waves propagation properties. With high quality processed data, we obtain the P velocity images through the pressure and vertical components. Modeling results indicate the PSS wave is generated from the direct "shear source" converted from P waves at the hard sea bottom. Exploring the propagation properties of PSS waves, we observed that the energy of PSS wave is much stronger than the PP wave at middle and far offset, and

the PSS wave involves various phase changes. Both the energy and wave itself could cause potential serious problems even to structural interpretation if not properly being considered in data processing. Considering PSS waves, we designed a model based processing workflow with partial stacking to identify and split shear wave information from horizontal components. The structural interpretations based on P and S velocity sections are consistent. These results verify the reliability of extracted S waves and the applicability of the proposed processing workflow in the shallow marine acquisition.

In conclusion, advanced processing algorithm and procedure were proposed in this research to extract the full potential of 4C OBC data and obtain high quality image sections for the interpretation. With further successful application, the algorithm, workflow and method could potentially be applied to both marine and land multicomponent acquisition to aid in reservoir characterization and hydrocarbon prediction.

REFERENCES

Ali, M.Y., Watts, A.B., and Searle, M.P. 2013. Seismic stratigraphy and subsidence history of the United Arab Emirates (UAE) rifted margin and overlying foreland basins. In K.A. Hosani, F. Roure, R. Ellison and S. Lokier (Eds), *Lithosphere Dynamics and Sedimentary Basins: The Arabian Plate and Analogues Frontiers in Earth Sciences*: 127-143. Berlin: Springer.

Askari, R., and Siahkoohi, H. 2008. Ground roll attenuation using the S and x-f-k transforms. *Geophysical Prospecting* **56**(1): 105-114. DOI: 10.1111/j.1365-2478.2007.00659.x

Ball, V., and Corrigan, D. 1996. Dual-sensor summation of noisy ocean-bottom data. *Proc*., 66th SEG Annual International Meeting, Denver, Colorado, 10-15 October, 28-31.

Barr, F.J., and Sanders, J.I. 1989. Attenuation of water column reverberations using pressure and velocity detectors in a water-bottom cable. *Proc*., 59th SEG Annual International Meeting, Dallas, Texas, 29 October-2 November, 653-655.

Basu, S., Mohapartra, S., and Viswanathan, S. 2012. Pre-conditioning of data before PZ summation in OBC survey – a case study. *Proc*., 9th Biennial International Conference and Exposition on Petroleum Geophysics, Hyderabad, 16-18 February, 357-362.

Berg, E., Svenning, B., and Martin, J. 1995. Sumic, a new strategic tool for exploration and reservoir mapping. *Journal of Applied Geophysics* **34**(2): 139-140.

Berteussen, K. and Sun, Y.F. 2010. A critical look at the acquisition parameters for sea bottom seismic in the Arabic Gulf. *Proc*., 80th SEG Annual International Meeting, Denver, Colorado, 17-22 October, 56-60.

Berteussen, K., Sun, Y.F., Ali, M., and Zhang, Z. 2014. Hunting S-waves using 4C seismic data in the carbonates, offshore UAE. *Proc.*, 84th SEG Annual International Meeting, Denver, Colorado, 26-31 October, 347-352. http://dx.doi.org/10.1190/segam2014-0347.1

Blouin, M., Gloaguen, E., Bellefleur, G., and Pugin, A. 2013. Characterizing seismic anisotropy in unconsolidated marine clay using 9C VSP data. *Proc*., 83th SEG Annual International Meeting, Las Vegas, Nevada, 347-351.

Christoffersson, A., Husebye, E.S. and Ingate, S.F. 1985. A new technique for 3-component seismogram analysis. Semiannual Technical Summery, Oct. 1984-Mar. 1985, NORSAR Scientific Report, Kjeller, Norway.

Cohen, L. 1995. *Time-frequency Analysis*. Upper Saddle River, New Jersey: Prentice Hall, Inc.

Crompton, R., Dodge, K., Whitfield, P., Bouska, J., and Johnston, R. 2005. Depth imaging of 3D, 4C OBS surveys in the Caspian sea. *Proc*. 75th SEG Annual International Meeting, Houston Texas, 5-6 November, 425-428.

Cultreri, J., Gilmer, A., and Hardage, B. 2005. Using 9C shear wave data to delineate sand in Morrow channels. *Proc*. 75th SEG Annual International Meeting, Houston Texas, 5-6 November, 440-443.

Dash, P.K., Panigrahi, B.K., and Panda, G. 2003. Power quality analysis using S-transform. *IEEE Transactions on Power Delivery* **18**(2): 406-411. DOI: 10.1109/TPWRD.2003. 809616.

Deighan, A.J., and Watts, D.R. 1997. Ground roll suppression using the wavelet transform. *Geophysics* **62**(6): 1896-1903. DOI: 10.1190/1.1444290.

Deng, J., Han, D., Liu, J., and Yao, Q. 2007. Application of spectral decomposition to detect deepwater gas reservoir. *Proc.*, 77th SEG Annual International Meeting, San Antonio, Texas, 23-26 September, 1427-1431. http://dx.doi.org/10.1190/1.2792766

Diallo, M., Kulesh, M., Holschneider, M., Scherbaum, F., and Adler, F. 2006. Characterization of polarization attributes of seismic waves using continuous wavelet transforms. *Geophysics* **71**(3): 67-77. http://dx.doi.org/10.1190/1.2194511

Donno, D., Nehorai, A., and Spagnolini, U. 2008. Seismic velocity and polarization estimation for wavefield separation. *IEEE Transactions on Signal Processing* **56**(10): 4794-4809. DOI: 10.1109/TSP.2008.927459

Dragoset, B., and Barr, F.J. 1994. Ocean-bottom cable dual-sensor scaling. *Proc*., 64th SEG Annual International Meeting, 857-860.

Duennebier, F. K., and Sutton, G. H. 1995. Fidelity of ocean bottom seismic observations. *Marine Geophysical Researches* **17**(6): 535–555.

El-Awawdeh, R., Khouri, N., Neyadi, A., Shevchek, Z., Shebl, H., Edwards, H., Gombos,A., and Johns, M. 2008. 3D seismic evidence of tertiary - Cretaceous

karsts and collapse disturbance from offshore oilfield in Abu Dhabi and outcrop analogs from Jebel Hafit, United Arab. *Proc*., Abu Dhabi International Petroleum Exhibition and Conference, Abu Dhabi, UAE, 3-6 November,1-13. http://dx.doi.org/10.2118/118006-MS.

Esmersoy, C. 1984. Polarization analysis rotation and velocity estimation in three-component VSP. In *Vertical Seismic Profiling Part B: Advanced Concepts*.236-255. Geophysical Press. Houston, Texas.

Flinn, E.A. 1965. Singal analysis using rectilinearity and direction of particle motion: Proc., *IEEE* **53**(12): 1874-1876.

Fjellanger, J.P., Boen, F., and Ronning, K.J. 2006. Successful use of converted wave data for interpretation and well optimization on Grane. *Proc.*, SEG Annual International Meeting, New Orleans, Louisiana, 1-6 October, 1138-1142.

Gaiser, J., Barr, F., and Paffenholz, J. 2002. Vertical component coupling of OBC data. *Proc.* 64th EAGE Conference & Exhibition, Florence, Italy, 27-20 May,1-4.

Gaiser, J.2007. Detector coupling corrections for vector infidelity of multicomponent OBC data. *Geophysics* **72(**3): 67-77.

Galiana-Merino, J. J., Parolai, S., and Rosa-Herranz, J. 2011. Seismic wave characterization using complex trace analysis in the stationary wavelet packet domain. *Soil Dynamics and Earthquake Engineering*. **31**(11): 1565–1578.

George, N.V., Sahu, S.S., Mansinha, L., Tiampo, K.F., and Panda, G. 2009. Time localised band filtering using modified S-transform. *Proc*. 2009 International

Conference on Signal Processing Systems, Singapore, 15-17 May, 1-5. DOI: 10.1109/ICSPS.2009.63

Goodyear, B.G., Zhu, H., Brown, R.A., and Mitchell, J.R. 2004. Removal of phase artifacts from fMRI data using a stockwell transform filter improves brain activity detection. *Magnetic Resonance Medvance* **51**(1):16-21.

Hardage, B.A., DeAngelo, M.V., Murray, P.E., and Sava, D. 2001. *Multicomponent Seismic Technology*. Tulsa: Society of Exploration Geophysicists.

Ikelle, L., and Lasse, A. 2005. *Introduction to Petroleum Seismology*. Tulsa: Society of Exploration Geophysicists.

Ishiyama, T., Painter, D.J., Belaid, K., Gazet, S., Suwaidi, A.S.A., Karwatowski, J., Mahgoub, M.,Furuya, K., El-Dakhakhny, A. and Sinno, R. 2008. 3D OBC seismic data processing for two overlapping carbonate fields offshore Abu Dhabi, United Arab Emirates. *Proc.*, Abu Dhabi International Petroleum Exhibition and Conference, Abu Dhabi, UAE, 3-6 November, 1-6.

Jackson, G.M., Mason, I.M. and Greenhalgh, S.A. 1991. Principal component transforms of triaxial recordings by singular value decomposition. *Geophysics* **56**: 528-533. http://dx.doi.org/10.1190/1.1443068

Johns, T.D., Vito, C., Clark, R., and Sarmiento, R. 2006. Multicomponent OBC (4C) prestack time imaging: offshore Trinidad, Pamberi, LRL Block. *Proc.*, SEG Annual International Meeting, New Orleans, Louisiana, 1-6 October, 1193-1197.

Johns, T. 2007. Applications of non-rigid matching to 3D converted-wave (PS) imaging. *Proc*., ASEG 19th Geophysical Conference, 1-5.

Jurkevics, A. 1988. Polarization analysis of three-component array data. *Bulletin of the Seismological Society of America* **75**(5): 1725-1743.

Konyuhov, A.I., and Maleki, B. 2006. The Persian Gulf Basin: geological history, sedimentary formations, and petroleum potential. *Lithology and Mineral Resources* **41**(4): 344-361.

Loewenthal, D., Lee,S.S., and Gardner, G.H.F. 1985. Deterministic estimation of a wavelet using impedance type technique. *Geophysical Prospecting* **33**(7):956-969. DOI: 10.1111/j.1365-2478.1985.tb00791.x

Magotra, N., Ahmed, N., and Chael, E. 1987. Seismic event detection and source location using single-station (three-component) data. *Bulletin of the Seismological Society of America* **77**: 958-971.

Martins, L.M.R., and Davis, T.L. 2014. From ocean-bottom cable seismic to porosity volume: A prestack PP and PS analysis of a turbidite reservoir, deepwater Campos Basin, Brazil. *Interpretation* **2**(2):91-103.

Montalbetti, J.F., and Kanasewich, E.R. 1970. Enhancement of teleseismic body phases with a polarization filter. *Geophysics Journal of the Royal Astronomical Society* **21**:119-129.

Morozov, I. B., and Smithson, S. B. 1996. Instantaneous polarization attributes and directional filtering. *Geophysics* **61**(2): 872–881.

Nahm, J.W., and Duhon, M.P. 2003. Interpretation and practical application of 4C-3D seismic data, East Cameron gas fields. *Gulf of Mexico* **22**(4): 300-309.

Nawab, S.H., and Quatieri, T.F. 1988. Short-time Fourier transform. In J.S. Lim and A.V. Oppenheim (Eds), *Advanced Topics in Signal Processing*, 289-337. Upper Saddle River, New Jersey: Prentice-Hall, Inc.

Nguyen, D.T., Brown, R.D., and Lawton, D.C. 1989. Polarization filter for multi-component seismic data. *CREWES Research Report* **7**: 93-101.

Parolai, S. 2009. De-noising of seismograms using the S transform. *Bulletin of the Seismology Society of America* **99**(1): 226-234.

Perelberg, A.I. and Hornbostel, S.C. 1994. Applications of Seismic Polarization Analysis. *Geophysics* **59**(1):119-130. DOI: 10.1190/1.1443522

Pethick, A. 2015. Marine Controlled Source Electromagnetic Visualisation. Retrieved from https://www.behance.net/gallery/956334/Marine-Controlled-Source-Electromagnetic-Visualisation.

Pinnegar, C.R. 2006. Time-frequency polarization analysis and filtering. *Recorder* **31**(7). Retrieved from http://csegrecorder.com/articles/view/time-frequency-polarization-analysis-and-filtering.

Pinnegar, C.R., and Eaton, E.E. 2003. Application of the S-transform to prestack noise attenuation filtering. *Journal of Geophysics Research* **108**(B9): 2422-2431. DOI: 10.1029/2002JB002258.

Pinnegar, C.R., and Mansinha, L. 2003a. The bi-Gaussian S transform. *SIAM Journal of Scientific Computing* **24**(5): 1678-1692. DOI:10.1137/S1064827500369803.

Pinnegar, C.R., and Mansinha, L. 2003b. The S-transform with windows of arbitrary and varying shape. *Geophysics* **68**(1): 381-385. http://dx.doi.org/10.1190/1.1543223.

Rajput, S. 2010. Converted wave velocity model using 4C ocean bottom seismometer data. *Proc.*, ASEG 21st Geophysical conference. Retrieved from http://www.publish.csiro.au/?act=view_file&file_id=ASEG2010ab212.pdf

Rosales, D.A., and Guitton, A. 2004. Ocean-bottom hydrophone and geophone coupling. Stanford Exploration Project Report 115:57-70.

Rusmanugroho, H. and McMechan, G.A. 2012. 3D, 9C seismic modeling and inversion of Weyburn field data. *Geophysics* **77**(4):161-173.

Rutty, M., and Greenhalgh, S.A. 1999. *Covariance Analysis in Seismic Signal Processing*. Tulsa: Society of Exploration Geophysicists.

Sahu, S.S., Panda, G., and George, N.V. 2009. An improved S-transform for time-frequency analysis. *Proc.*, IEEE International Advance Computing Conference, Patiala, India, 6-7 March, 315-319. DOI: 10.1109/IADCC.2009.4809028.

Sato, Y. 1955. Analysis of dispersed surface waves by means of Fourier Transform. *Bulletin of the Earthquake Research Institute* **33**: 33-47.

Samson, J.C., and Olson, J.V. 1980. Some comments on the descriptions of the polarization states of waves. *Geophysics Journal of the Royal Astronomical Society* **61**(1): 115-129. DOI: 10.1111/j.1365-246X.1980.tb04308.x.

Samson, J.C., and Olson, J.V. 1981. Data-adaptive polarization filters for multichannel geophysical data. *Geophysics* **46**(10): 1423-1431. http://dx.doi.org/10.1190/1.1441149.

Schalkwijk, K.M., Wapenaar, C.P.A., and Verschuur, D.J. 1999.Application of two-step decomposition to multicomponent ocean-bottom data: Theory and case study. *Journal of Seismic Exploration* **8**:261-278.

Schimmel, M., and Gallart, J. 2005. The inverse S Transform in filters with time-frequency localization. *IEEE Transactions on Signal Processing* **53**(11): 4417-4422. DOI: 10.1109/TSP.2005.857065

Schimmel, M., and Gallart, J. 2007. Authors' Reply to Comments on "The inverse S transform in filters with time-frequency localization", *IEEE Transactions on Signal Processing* **55**(10): 5120-5121.

Sejdic, E., Djurovic, I., and Jiang, J. 2007. S transform with frequency dependent Kaiser window. *Proc.*, Acoustics, Speech and Signal Processing, Honolulu, Hawaii, 15-20 April, 1165-1168. DOI:10.1109/ICASSP.2007.367049.

Sinha, S., Routh, P.S., and Anno, P. 2009. Instantaneous spectral attributes using scales in continuous-wavelet transform. *Geophysics* **74**(2):137-142. DOI: 10.1190/1.3054145

Sinha, S., Routh, P.S., Anno, P., and Castagna, J.P. 2005. Spectral decomposition of seismic data with continuous-wavelet transform. *Geophysics* **70**(6): 19-25. DOI: 10.1190/1.2127113

Sirat, M., and Sun, Y. 2006. Oil and gas in the UAE: present and future production. *Proc.*, Energy 2030 International Conference, Abu Dhabi, UAE, 1-2 November, 62-63.

Shieh, C.F., and Herrmann, R.B. 1990. Ground roll: rejection using polarization filters. *Geophysics* **55**(9): 1216-1222. DOI: 10.1190/1.1442937

Stockwell, R.G., Mansinha, L., and Lowe, R.P. 1996. Localization of the complex spectrum, the S transform. *IEEE Transactions on Signal Processing* **44**(4): 998-1001. DOI: 10.1109/78.492555

Stockwell, R.G. 2007. A basis for efficient representation of the S-transform. *Digital Signal Process* **17**: 371-393. DOI: 10.1016/j.dsp.2006.04.006

Stratton, J.A. 1941. *Electromagnectic Theory*. New York City: McGraw-Hill.

Sun, Y.F. and Berteussen, K. 2009a. New opportunities of 4C ocean bottom seismic in shallow-water environment of the Arabian Gulf: A case study. *Proc.*,79th SEG Annual International Meeting, Houston, Texas, 25-30 October, 46-50.

Sun, Y.F., and Berteussen, K. 2009b. Challenge and opportunity of 4C ocean bottom seismics in shallow water environment. *Proc.*,71st EAGE Conference, Amsterdam, Netherlands, 8-11 June, 1-5.

Sun, Y.F., and Berteussen, K. 2010. Multicomponent seismic acquisition in the Arabic Gulf- Should we take a new look at the acquisition parameters. *Proc.*,72nd EAGE Conference, Barcelona, Spain, 14-18 June, 124-128.

Tan, Y.Y., He, C., Wang, Y.D., and Zhong, Z. 2013. Ground roll attenuation using a time-frequency dependent polarization filter based on the S transform. *Applied Geophysics* **10**(3): 279-294.

Tatham, R.H., and Goolsbee, D.V. 1984. Separation of P- and S-wave reflections offshore western Florida. *Geophysics*, **49**: 493-508.

Tatham, R.H., and McCormack, M.D. 1991. Multicomponent Seismology in Petroleum Exploration. Tulsa: Society of Exploration Geophysicists. http://dx.doi.org/10.1190/1.9781560802556

Todorov, T., and Margrave, F.G. 2010. Variable-factor S-transform for time-frequency decomposition, deconvolution, and noise attenuation. *Proc.*, GeoCanada, Calgary, Alberta, 10-14 May, 1-4.

Waggoner, J. and Kristiansen, P. 2003. Using multicomponent seismic data to better understand reservoir characteristics. *Proc.*, SPE Annual Technical Conference and Exhibition, Denver, Colorado, 5-8 October, 1-8. DOI:http://dx.doi.org/10.2118/84569-MS

Vetri, L., Loinger, E., Gaiser, J., Grandi, A., and Lynn, H. 2003. 3D/4C Emilio: Azimuth processing and anisotropy analysis in a fractured carbonate reservoir. *The Leading Edge* **22**(7): 675-679.

Vidale, T. 1986. Complex polarization analysis of particle motion. *Bulletin of the Seismological Society of America* **76**(5): 1393-1405.

Yilmaz, O. 2001. *Seismic Data Processing.* Tulsa: Society of Exploration Geophysicists.

Zhang, Z., Sun, Y.F., and Berteussen, K. 2010. Analysis of surface waves in shallow water environment of the Persian Gulf using S and t-f-k transform. *Proc.*, 80th SEG Annual International Meeting, Denver, Colorado, 17-22 October, 3723-3728. http://dx.doi.org/10.1190/1.3513624.

Zhang, Z., Sun, Y.F., and Berteussen, K. 2012. Improving OBC data quality of the geophone components in shallow-water Persian Gulf through advanced time-

frequency analysis. *Proc*., 82nd SEG Annual International Meeting, Las Vegas, Nevada, 4-9 November, 1131-1135. http://dx.doi.org/10.1190/segam2012-1133.1

Zhang, Z., Sun, Y.F., and Berteussen, K., and Ali, M. 2013. Effect of Scholte wave on rotation of multi-component OBC seismic data in shallow water environment of the Arabian Gulf. *Proc.*, 83rd SEG Annual International Meeting, 22-27 September, Houston, Texas, 1233-1238. http://dx.doi.org/10.1190/segam2013-1233.1.

Zhang, Z., Sun, Y.F., and Berteussen, K., and Ali, M. 2014. A new method of surface wave analysis and OBC signal enhancement in shallow environment of the Arabian Gulf using time-frequency-wavenumber polarizaiton analysis. *Proc.*, ADIPEC Conference, Abu Dhabi, UAE, 10-13 November, 1-10. http://dx.doi.org/10.2118/172078-MS

Zhang Z., Sun, Y.F. and Berteussen K., 2015, "Time Frequency Wavenumber Analysis of Surface Waves and Signal Enhancement using S-Transform", Journal of Computational Acoustic. (Accepted)

Zheng, Y., and Stewart, R. 1992. Polarization filter: design and testing. *CREWES Research Report* **4**(8): 1-19.

Zhu, H., Goodyear, B.G., Lauzon, M.L., Brown, R.A., Mayer, G., Law, A.G., Mansinha, L., and Mitchell, J.T. 2003. A new local multistate Fourier analysis for medical imaging. *Medical Physics* **30**(6): 1134-1141.